Aqueous Dielectric Effects

am Fachbereich Physik der Freien Universität Berlin
eingereichte Dissertation

zur Erlangung des akademischen Grades
eines Doktors der Naturwissenschaften (Dr. rer. nat.)

vorgelegt von

Klaus F. Rinne

Berlin, Januar 2015

Erster Gutachter:	Prof. Dr. Roland R. Netz
	Freie Universität Berlin
Zweite Gutachterin:	Prof. Dr. Petra Imhof
	Freie Universität Berlin
Tag der Disputation:	6. März 2015

Contents

Chapter 1

Introduction

"Nothing in the world is softer and weaker than water, yet nothing is better at overcoming the hard and strong. This is because nothing can alter it."

Lǎozǐ, Dàodéjīng chapter 78

1.1 Water and Aqueous Solutions in Bulk and at Interfaces

Already before the ancient Greeks the importance of water for our planet and for life was highlighted. As examples I would like to mention the creation story in the Old Testament and Wǔ Xíng, the Five Elements in the Chinese philosophy, consisting of water, wood, fire, earth and metal.

In fact, the shape of the earth is dominated by the water of the oceans and large glaciers of ice and snow at the poles and high mountain areas. All together, liquid water and ice cover more than 70 % of our planet's surface.

Water vapour is present in the atmosphere and is highly relevant for the climate cycle. The natural presence of all three phases is uniquely found for water[1]. Other molecules of the size of water as for instance carbondioxide or methane have a much lower boiling temperature. The reason for the high boiling temperature and specific heat capacity of water is its strong polarity due to the large electronegativity of the oxygen, which allows the forming of hydrogen bonds (H-bonds) with neighbouring water molecules. While in the ice phase the maximum of four H-bonds per molecule with 25 kJ per mol is reached[2], the average number of bonds decreases with increasing temperature due to entropic effects. The H-bond network is a key factor for the temperature density anomaly of water reaching the maximal density at 4°C[3, 4]. Isobaric cooling below this temperature leads to an expansion. Life in deep oceans is only possible because the density anomaly keeps the temperature at 4°C and water in the liquid phase there. Water is essential for life of plants and living beings from single-cell organisms up to large mammals. A large amount of the volume of our body is water. Biological cells can not work without it. The relevant chemical reactions inside our body keeping us alife are only possible because the reaction components are dissolved in water.

In the following I list a few salient features of the solvation properties of water, which are recently studied: The solubility of hydrophobic particles in water typically displays a temperature anomaly[5]. In general, the solvent affects the structure of macro-molecules[6, 7, 8]. It is supposed that a conformational change of proteins leading to insolubility is a key factor of neurodegenerative diseases such as Parkinson's or Huntington's disease[9, 10]. The hydrophobic effect is suggested to play a key role in the stabilization of proteins[11]. There is an ongoing discussion whether the hydration water dominates the dynamics of proteins[12, 13]. It is well established that the water structure and dynamics inside hydration shells around solutes are modified. But the mechanisms behind are not fully understood yet. Aqueous solutions of mono-atomic and monovalent ions as for instance sodium chloride are a simple model system to study solution-solvent interactions with dielectric spectroscopy and simulations[14, 15, 16].

The tendency to form H-bonds also controls the properties of interfacial water, which are often departing from the bulk attributes. The surface tension of water at an air-water interface is very large due to the missing H-bond partners at the interface. Most unpolar surfaces are unfavourable for water. The Lotus effect can occur at superhydrophobic surfaces[17, 18, 19], while polar surfaces are wetted in contact with water. Hydrophobic surfaces can have a very low water friction coefficient and a large slip length[20, 21, 22, 23, 24]. These characteristics are crucial for the flow speed in thin ducts. Carbon nanotubes are an excellent example of hydrophobic pipes and a model system for biological channels. To generate flow in these systems, various pump designs based on temperature gradients[25], Coulomb dragging[26] or surface waves[27] were proposed. Electro-kinetic pumping mechanisms are a possible alternative, as we show in this thesis.

1.2   Dielectric Susceptibility

The Coulomb force is one of the fundamental interactions and central for the properties of the dipolar solvent water. The dielectric response to electric fields provides information about structure, time-scales and free energies. Furthermore, the impact of electromagnetic radiation from mobile phones and high-voltage overhead lines on the human body is a topic of political and scientific discussions[28, 29].

An internal (local) electric field $\vec{E}$ generates a polarization $\vec{P}$ inside a probe. As a result only the dielectric displacement field $\vec{D}$ fulfills the continuous equation (equation 1.2), even if the external charge density ρ is zero. Polarization density $\vec{P}/V$ and internal electric field are related by the susceptibility $\chi = \epsilon - 1$, which is independent of $\vec{E}$ for weak electric fields (equation 1.4). For interfacial water it has been shown that quadrupole moments and higher moments can be relevant for dielectric effects[30]. The tensorial character of the frequency dependent response function

$$\vec{\nabla} \times \vec{E} = 0 \qquad (1.1)$$
$$\vec{\nabla} \cdot \vec{D} = \rho \qquad (1.2)$$
$$\vec{P}/V = \vec{D} - \epsilon_0 \vec{E} \qquad (1.3)$$
$$= \epsilon_0 \chi \vec{E} \qquad (1.4)$$
$$= \epsilon_0 (\epsilon - 1) \vec{E} \qquad (1.5)$$

Maxwell equations

tion $\chi(f) = \chi'(f) - i\chi''(f)$ is relevant for non-isotropic dielectric materials[31, 32, 33] or at interfaces[34, 35]. For inhomogeneous fields or at interfaces χ becomes a function of position. Recent molecular dynamics simulations show that the dielectric response of water at an interface

is different if the electric field is applied perpendicular to the interface than parallel to it. The perpendicular component of the permittivity is even found to be negative in some regions[30, 34, 36]. The simulation results are supported by experimentally measured overscreening of an interfacial surface charge within the double-layer[37, 38]. These interfacial dielectric features also affect hydrodynamics close to the interface[39, 40].

For water in the bulk phase and homogeneous fields the response function $\chi(f)$ is scalar. The dielectric properties of water in the immediate vicinity of ions and surface groups of proteins and other biomolecules are important for a number of technological and biological processes[41, 42] such as protein folding, coagulation and flocculation and nanofiltering.

The static dielectric constant of non-conducting materials can be measured using capacitance bridges[43, 44]. A powerful tool to determine isotropic dielectric spectra up to frequencies f of about 100 GHz is dielectric resonance spectroscopy, even in the presences of free charges. These experiments measure the reflection or transmission of a probe relative to air[45, 46]. The obtained frequency dependent dielectric loss has to be corrected by the contribution due to the static conductivity. This correction term increases with inverse frequency and sets a lower frequency limit of the method at about 0.1 GHz. Lumped circuit techniques can be used, if much lower frequencies are targeted[47]. On the high frequency side terahertz time-domain spectroscopy is available in the lower THz-range, while for even higher frequencies Fourier transform spectroscopy is favored[48, 49, 50, 51].

The dielectric spectrum of pure water at room temperature obtained from dielectric resonance spectroscopy is almost perfectly described by a single Debye process (equation 1.6 with $\alpha = 0$) with a relaxation time $\tau_{CC} \approx 8.3$ ps and a static dielectric constant $\epsilon_{CC} \approx 80$. Increasing temperature leads to a decrease of the relaxation time

$$\chi(f) + 1 = \frac{\epsilon_{CC}}{1 + (i\,2\pi f \tau_{CC})^{1-\alpha}} \qquad (1.6)$$

Cole-Cole fit function for dielectric spectra. α is zero for a Debye process.

and the dielectric constant[52]. Addition of sodium chloride to water leads to a blue shift, a decrease of the dielectric constant and a broadening of the signal, which is quantified by an increasing Cole-Cole exponent α[53]. Other aqueous sodium-halide solutions show a similar concentration dependence[54, 55]. The loss of dielectric susceptibility is too strong to be just a trivial water dilution effect. So, the spectral changes can not be explained without including a modified dielectric response of water in the vicinity of the ions. For solutions of multi-atomic ions such as sodium succinate[56], sodium sulfate[57], magnesium sulfate[58], scandium sulfate[59, 60] or aluminium sulfate[59] additional slow processes attributed to slow solvation shell water or ion pairing are reported. Robust simulations are helpful to uncover the origin of these effects. Dielectric spectra of aqueous peptide solutions can have a dielectric constant higher than pure water, due to the high polarization of some peptides[61, 62]. Rotations and tumbling of these large molecules cause spectral resonances in the sub-GHz range.

Apart from the mentioned spectroscopy techniques which track the total (collective) polarization of a probe, nuclear magnetic resonance (NMR) studies[63, 64], two-dimensional infrared vibrational echo spectroscopy[65, 66], femto-second polarization-resolved infrared pump-probe experiments[15, 67] and polarization resolved THz time-domain Raman spectroscopy[68] couple to the orientation of single water molecules. These experiments have greatly enhanced the understanding of the

hydrogen bond dynamics in the water solvation shell around charged and uncharged solutes. Two-dimensional infrared vibrational echo spectroscopy experiments of aqueous solutions of sodium bromide found retarded single water dynamics[69], while the corresponding dielectric relaxation spectroscopy experiments observe an acceleration of the collective water dynamics[55].

Computer simulations are helpful to resolve this experimental puzzle by the simultaneous analysis of single-water and collective-water dynamics in the ion solvation shells. The frequency-dependent dielectric spectrum $\chi(f)$ can be obtained from equilibrium molecular dynamics simulations by the time evolution of the polarization $\vec{P}(t)$ via the fluctuation dissipation theorem:

$$\chi(f) = -\frac{1}{3V k_B T \epsilon_0} \int_0^\infty e^{-2\pi i f t} \langle \vec{P}(0) \cdot \dot{\vec{P}}(t) \rangle \mathrm{d}t, \tag{1.7}$$

where V is the system volume, $k_B T$ the thermal energy, ϵ_0 the vacuum permittivity and $\dot{\vec{P}}(t) = \mathrm{d}\vec{P}(t)/\mathrm{d}t$ is the time derivative of the polarization $\vec{P}$. A derivation of the fluctuation dissipation theorem is presented in Appendix A. Simulation trajectories allow a split up of the total polarization into different terms and therefore an assignment of spectral resonances to the interactions between different solution components is possible[70].

1.3 Modeling: Molecular Dynamics Simulations

In molecular dynamics (MD) simulation packages like GROMACS[71] or LAMMPS[72] the equations of motion are integrated numerically for each atom to follow the time evolution of a system. An MD simulation is deterministic and the particle trajectories depend on the initial positions and velocities of the atoms in the system. If the time evolution of a system is simulated long enough, all regions of the $6\,N$-dimensional phase space are covered during a simulation, no matter which initial condition has been chosen. In this case, an ensemble and time average of variables can be calculated from the particle trajectories.

The attractive Van der Waals interaction and the short ranged, strong Pauli repulsion between atoms are considered in the simulation via the 6-12 Lennard-Jones-potential (LJ) with the potential strength ϵ_{ij}, the range σ_{ij} and the particle distance $r_{ij} = |\vec{r}_i - \vec{r}_j|$. If we add the Coulomb interaction for charges q_i, the non-bonded energy of an N-particle system is the following:

$$E_{\text{non-bonded}} = \frac{1}{2} \sum_{i=1}^{N} \sum_{j\neq i}^{N} \left[4\epsilon_{ij} \left(\left(\frac{\sigma_{ij}}{r_{ij}} \right)^{12} - \left(\frac{\sigma_{ij}}{r_{ij}} \right)^{6} \right) + \frac{q_i q_j}{4\pi\epsilon_0 r_{ij}} \right], \tag{1.8}$$

where the LJ parameters for interaction between particles of different atom types A and B are usually obtained from the Lorentz-Berthelot mixing rules,

$$\epsilon_{\text{AB}} = \lambda_\epsilon \sqrt{\epsilon_{\text{A}} \epsilon_{\text{B}}} \tag{1.9}$$

$$\sigma_{\text{AB}} = \lambda_\sigma (\sigma_{\text{A}} + \sigma_{\text{B}})/2, \tag{1.10}$$

where λ_ϵ and λ_σ are very often set to unity. In order to form molecules from several atoms and to keep their intra molecular structure, bonded forces between atoms of the same molecule are

added to the non-bonded forces. Commonly harmonic potentials of strength k_r and k_θ around the equilibrium bond lengths b_0 and the equilibrium angles θ_0 are applied:

$$E_{\text{bonded}} = \sum_{\text{bonds}} \frac{k_r}{2}(b - b_0)^2 + \sum_{\text{angles}} \frac{k_\theta}{2}(\theta - \theta_0)^2 \qquad (1.11)$$

Alternatively bond lengths and angles can be fixed via constrained algorithms[73, 74] to save computational cost. The total energy of the simulation system is the sum of bonded and non-bonded energies.

A set of parameters for the bonded interactions, the partial charges q_i and the LJ parameters σ_i and ϵ_i is known as a force field. For water various 3-particle models with LJ interaction on the oxygen and partial charges on all atoms have been developed as TIPS[75], SPC[76], TIP3P[77] and SPC/E[78] and optimized with respect to different observables. Additionally, more complicated water force fields with one or more dummy atoms as for example TIP4P[77] or TIP5P[79] exist, but are computationally more expensive. In our work we will use the SPC/E model, since it reproduces the dielectric constant in the best way compared to the other established 3-point models[80, 81]. In case of ionic solutions the LJ interaction parameters between ions and water as well as between ions and ions follow from an optimization with respect to solution properties. A recent force field optimization for mono-valent ions using $\lambda_\sigma \neq 1$ successfully reproduces solvation free energies and activity coefficient derivative with respect to salt concentration[82]. A force field optimization for peptides is very challenging because of the large amount of non-bonded degrees of freedom and different functional groups and we therefore use the established Amber03 force field[83].

Since every degree of freedom contributes $k_B T/2$ to the kinetic energy E_{kin} with the Boltzmann constant k_B and temperature T, the temperature of the system can be directly calculated from the particle velocities and the number of degrees of freedom N_{f}:

$$T = \frac{2E_{\text{kin}}}{k_B N_{\text{f}}} = \sum_{i=1}^{N} \frac{m_i v_i^2}{k_B N_{\text{f}}} \qquad (1.12)$$

Most systems are in contact with a heat bath, which keeps the system at temperature T. As a consequence, in simulations the particle velocities have to be rescaled by a thermostat as for instance Berendsen thermostat[84] or Nosé Hoover thermostat[85, 86]. If one velocity component is expected to have a non zero average velocity like in the case of a continuous flow, only the other velocity components should be used to determine the temperature. If periodic boundary conditions are used, the system size is quasi infinite and the long range Coulomb interaction can be calculated in Fourier space similarly to the Ewald summation for ionic crystals[87]. For MD simulations computationally more efficient algorithms like Particle-mesh Ewald (PME)[88] or Particle-Particle Particle-Mesh (PPPM)[89] are available. Short ranged Lennard-Jones (LJ) interactions are neglected for larger distances to increase computational speed. Various cutoff methods have to be used carefully to avoid artifacts[v][90, 91].

1.4   Outline of this Work

The first part of this thesis aims to understand the interactions between water and solutes by dielectric spectra obtained from equilibrium molecular dynamics simulations. In the following chapter we obtain dielectric spectra of aqueous solutions of NaF, NaCl, NaBr and NaI and decompose the spectra into contributions of different solvation shells, ionic current and water polarization cross-correlation and a pure ionic term to cover the dynamics on the molecular scale. In chapter three we decompose the water contribution of the sodium-halide spectra in self correlation effects of single water dipoles and the collective relaxation with other water molecules to resolve the experimental puzzle of reverse dynamical trends between the two components. Both experimental findings are reproduced and explained using the Madden-Kivelson theory[92], which relates the static dielectric constant and the relaxation time.

In chapter four we study the dielectric spectra of an eight residue alanine solvated in water. Projection of equilibrium simulations into folded and unfolded peptide configurations allows to understand how ordering of an otherwise identical amino acid sequence changes the dielectric response. Furthermore, we show that the presence of the peptide significantly affects the collective water relaxations in comparison with pure bulk water. The dynamics of single water dipoles is only weakly slowed down. We explain the slow cross-correlation between hydration shell water and outer shell water observed in earlier studies in terms of the absence of fast self-relaxation contributions.

Chapter five of this work demonstrates the pumping of pure water through a carbon nanotube via AC electric fields. The minimal pump setup of two electrodes aligned along a carbon nanotube filled with water driven with phase shifted AC voltage is presented. Due to the high dielectric susceptibility, the water dipoles orient in the external electric field and follow its motion. The pumping mechanism is explained by a polarization-dragging theory. The parameter dependence is extensively studied and successfully compared to the predictions from the polarization-dragging theory, developed in this thesis.

Chapter 2

Dissecting Ion-Specific Dielectric Spectra of Sodium-Halide Solutions into Solvation Water and Ionic Contributions

2.1   Introduction

Water interacts with solutes differently than with other water molecules, which influences the electromagnetic response properties of aqueous solutions and therefore leads to distinct signatures of solvation water and bulk water in absorption spectra. This makes spectroscopy a preferred method for the study of the mechanism of how water solvates polar as well as nonpolar solutes. Dielectric relaxation spectroscopy is a powerful experimental tool to measure the dielectric susceptibility of aqueous solutions in the GHz range and allows to resolve very slow solvation processes[93]. This frequency range is accessible to equilibrium molecular dynamics (MD) simulations which therefore allows in principle for a detailed comparison of simulated and experimental spectra. Robust experimental dielectric spectra are available for solutions of the salts NaF, NaCl, NaBr, and NaI from the Buchner group[53, 54, 55], which by comparison allow to infer ion-specific effects on the static as well as dynamic dielectric properties in an insightful manner. A number of simulation studies calculated dielectric spectra of salt solutions and in particular analyzed the various water, ions and ion-water cross-contributions to the total spectrum[61, 94, 95, 96, 97, 98, 99, 100, 101]. Surprisingly, no explicit comparison between simulated and experimental dielectric spectra was undertaken, and also the influence of ion-specific effects on dielectric spectra was not addressed in previous simulation work. Only for aqueous saccharide solutions concentration dependent spectra from experiments and simulation were quantitavely compared[102].

This is curious since the decomposition of experimentally measured dielectric spectra into individual contributions stemming from water and ions is challenging and can only be accomplished by fitting the spectra to heuristic sum formulas, assuming that one knows the functional form of the individual spectral contributions and that simple superposition is valid. In contrast, the full polarization auto-correlation function, which is related to the dielectric spectrum via Fourier transformation, can be straightforwardly decomposed into different molecular contributions in MD simulations. Consequently, if the statistics are robust and the force fields are validated, MD simulations can help to answer central questions related to the range over which ions are able to perturb the water structure and dynamics[103, 104, 105]. Other pertinent open questions are whether ion-water polarization cross-correlations enhance or suppress dielectric absorption and to what degree ion-polarization auto-correlations contribute to the static dielectric constant.

In this chapter we report on extensive MD simulations for NaF, NaCl, NaBr and NaI salt solutions. The dielectric spectra show a significant blue shift and a simultaneous decrease of the static dielectric constant with increasing salt concentration and increasing anion size, in almost quantitative agreement with experimental data[53, 54, 55]. This serves as a validation of the non-polarizable force fields employed and of the technique we use in order to extract the spectral information from the simulation trajectories. The purely ionic contribution to the dielectric response is negligible, the ion-water cross-correlation contribution however is negative and reduces the total dielectric response by about 5-10% for 1 M solutions. By a separate analysis of the dielectric contribution from consecutive water solvation shells around ions we demonstrate that the salt-induced effects on the dielectric spectra and in particular the salient blue shift primarily stem from the first solvation shell around ions. This is in agreement with the recent interpretation of THz experiments that probe the collective water motion around ions in a different frequency regime[48].

With rising salt concentration the simulated spectra show more pronounced deviations from a single-Debye form, as quantified by the exponent α of a Cole-Cole fit, this is in quantitative agreement with experimental spectra. Our spectral decomposition into ionic and different water solvation shell contributions does not render the individual contributions more Debye-like, this suggests that the non-Debye-like character of the total dielectric spectra of salt solutions is not due to the superposition of different elementary Debye-like relaxation processes with different relaxation times. Rather, we conclude that the non-Debye-like character of salt solution spectra is an inherent signature of the first water solvation shell around ions.

This chapter is structured in the following way: In section 2.2 we discuss our simulation methods. We validate our methods by comparison of the total dielectric spectra with experimental data in section 2.3, and in section 2.4 we discuss the spectral decomposition results.

2.2   Methods

2.2.1   Dielectric Response Functions

The complex frequency-dependent dielectric susceptibility $\chi(f) = \chi'(f) - i\chi''(f)$ relates the total system polarization $\vec{P}(f)$ to the electric field $\vec{E}(f)$ via the linear-response relation $\vec{P}(f) = \chi(f)\epsilon_0\vec{E}(f)$, where ϵ_0 is the vacuum permittivity. According to the fluctuation dissipation theorem $\chi(f)$ follows

from the auto-correlation of equilibrium polarization fluctuations via[106, 107]

$$\chi(f) = -\frac{1}{3Vk_BT\epsilon_0} \int_0^\infty e^{-2\pi ift} \langle \vec{P}(0) \cdot \dot{\vec{P}}(t) \rangle \mathrm{d}t, \tag{2.1}$$

where $\dot{\vec{P}}(t)$ denotes the time derivative of the time-dependent total polarization $\vec{P}(t)$, V is the system volume and k_BT is the thermal energy. Equation 2.1 thus allows to obtain the complete susceptibility spectrum from one simulation trajectory in equilibrium. Note that for a salt solution the total polarization consists of the water polarization $\vec{P}_\mathrm{W}$ and the ionic polarization $\vec{P}_\mathrm{I}$ according to $\vec{P} = \vec{P}_\mathrm{W} + \vec{P}_\mathrm{I}$. In a periodic simulation box it is convenient to express the ionic polarization in terms of the ionic current $\vec{J}_\mathrm{I}$ via $\vec{J}_\mathrm{I}(t) = \mathrm{d}\vec{P}_\mathrm{I}(t)/\mathrm{d}t$. The susceptibility has a low-frequency diverging imaginary part due to the ionic DC-conductivity, what is typically experimentally reported is the DC-conductivity corrected dielectric signal $\Delta\chi(f) = \chi(f) + i\sigma_0/(2\pi f)$ that displays regular behavior in the low-frequency limit, where $\sigma_0 = \sigma(f=0)$ is the static ionic conductivity.

The frequency-dependent ionic conductivity $\sigma(f) = \sigma'(f) - i\sigma''(f)$ by definition relates the electric current due to free ionic charges with the applied electric field according to $\vec{J}_\mathrm{I}(f) = \sigma(f)\epsilon_0\vec{E}(f)$ and can be calculated from the polarization-current cross-correlations via[70]

$$\sigma(f) = \frac{1}{3Vk_BT\epsilon_0} \int_0^\infty e^{-2\pi ift} \langle \vec{J}_\mathrm{I}(0) \cdot \dot{\vec{P}}(t) \rangle \mathrm{d}t. \tag{2.2}$$

By defining the auto and cross-correlation functions of the water polarization and ionic current as

$$\phi_\mathrm{W}(t) = \frac{\langle \vec{P}_\mathrm{W}(0) \cdot \vec{P}_\mathrm{W}(t) \rangle}{3Vk_BT\epsilon_0} \tag{2.3}$$

$$\phi_\mathrm{IW}(t) = \frac{1}{2} \frac{\langle \vec{P}_\mathrm{W}(0) \cdot \vec{J}_\mathrm{I}(t) - \vec{J}_\mathrm{I}(0) \cdot \vec{P}_\mathrm{W}(t) \rangle}{3Vk_BT\epsilon_0} \tag{2.4}$$

$$\phi_\mathrm{I}(t) = \frac{\langle \vec{J}_\mathrm{I}(0) \cdot \vec{J}_\mathrm{I}(t) \rangle}{3Vk_BT\epsilon_0}, \tag{2.5}$$

we can express the frequency-dependent ionic conductivity as a sum of a pure ionic term σ_I and an ion-water cross-correlation term σ_IW,

$$\sigma(f) = \sigma_\mathrm{IW}(f) + \sigma_\mathrm{I}(f) \tag{2.6}$$

$$\sigma_\mathrm{IW}(f) = -i2\pi f \int_0^\infty e^{-2\pi ift} \phi_\mathrm{IW}(t) \mathrm{d}t \tag{2.7}$$

$$\sigma_\mathrm{I}(f) = \int_0^\infty e^{-2\pi ift} \phi_\mathrm{I}(t) \mathrm{d}t. \tag{2.8}$$

It follows that the static conductivity is determined by the pure ionic term and can be written as $\sigma(f=0) = \sigma_\mathrm{I}(f=0) = \int_0^\infty \phi_\mathrm{I}(t)\mathrm{d}t$. The regularized susceptibility $\Delta\chi(f)$ can be decomposed into

three separate terms according to

$$\Delta\chi(f) = \chi_W(f) + \chi_{IW}(f) + \Delta\chi_I(f) \tag{2.9}$$

$$\chi_W(f) = \phi_W(0) - i2\pi f \int_0^\infty e^{-2\pi i f t}\phi_W(t)\mathrm{d}t \tag{2.10}$$

$$\chi_{IW}(f) = -2 \int_0^\infty e^{-2\pi i f t}\phi_{IW}(t)\mathrm{d}t \tag{2.11}$$

$$\Delta\chi_I(f) = -\frac{i}{2\pi f} \int_0^\infty (e^{-2\pi i f t} - 1)\phi_I(t)\mathrm{d}t, \tag{2.12}$$

as first shown by Caillol et al.[70] in 1986. The full derivation is given in the following section.

2.2.2   Water Hydration Shells and Ion-Pair States

The radial distribution function $g_{Na,O}(r)$ between sodium and water oxygen in Figure 2.1 A and $g_{-,O}(r)$ between anions and water oxygen in Figure 2.1 B exhibit well-defined maxima and minima, which allows to partition solvation water into distinct solvation shells. The positions of the local minima in the radial distributions, indicated by orange vertical dashed lines for F as an anion and by black dashed lines for Cl as an anion (Br and I give positions very similar to Cl and are therefore not shown), allow to distinguish first solvation-shell water, W1, and second solvation-shell water, W2, from third solvation-shell water, W3, as indicated in the figures. Note that the shell denoted by W3 contains all water molecules that are not part of the first and second solvation shells.

Likewise, the oscillations in the sodium-anion radial distribution functions $g_{Na,-}(r)$ in Figure 2.1 C point to distinct ion pair configurations[108, 109]. We indicate the first three minima of $g_{Na,-}(r)$ by vertical dashed lines, orange for NaF and black for NaCl, the positions of the minima for NaBr and NaI are again very close to the ones for NaCl and not shown. This gives rise to four different ion-pair populations, namely contact ion pairs (CIP), single solvent-separated ion pairs (SIP), doubly solvent-separated ion pairs (DSIP), and free ions (FI), as indicated in Figure 2.1 C. A schematic illustration of different ion-pair configurations is shown in Figure 2.1 D. The CIP lifetime is estimated as 12.3 ps for 1 M NaCl in Appendix B.2.

In contrast to the radial distribution functions in Figure 2.1 C, the number fraction n_I^k of different ion-pair configurations in Figure 2.1 E is dominated by single solvent-separated ion pairs (SIP) for all studied salts (here the index k numbers the four different ion-pair states CIP, SIP, DSIP, and FI). This reflects that although for the salts NaCl, NaBr, NaI the sodium-anion radial distribution in Figure 2.1 C is maximal for contact ion pairs (CIP), the solvent-separated ion pair population wins by numbers because of the larger shell radius. Note that in determining the number fractions n_I^k the ion-pair state k of an ion is defined by the closest counterion. Also, the sum of n_I^k is normalized to unity, $\sum_k n_I^k = 1$. The most pronounced variation among different salts at 1 M is seen for the contact ion pairs (CIP), which are maximal for NaCl and almost non existent for NaF, which reflects the strongly bound water solvation shell for NaF. When comparing the fractions n_I^k for the different concentrations of NaCl, we see that with increasing concentration the number of free ions (FI) goes down while the CIP fraction goes up.
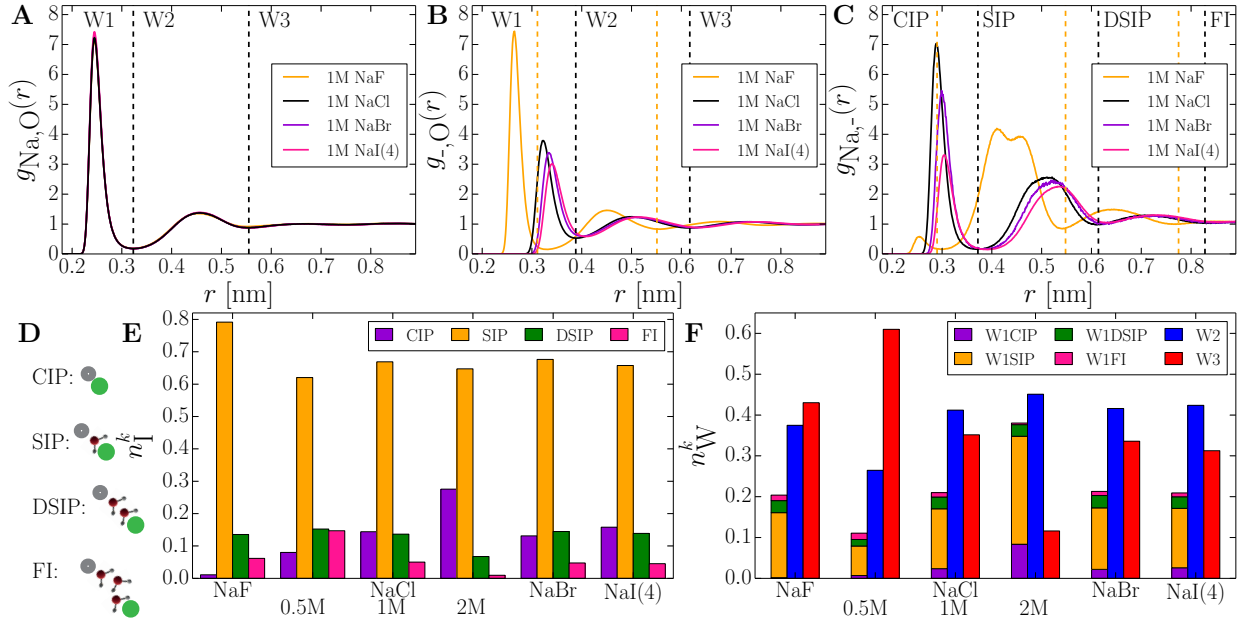
FIGURE 2.1: Water solvation layers and ion-pair states: (A) The radial distribution functions $g_{Na,O}(r)$ between sodium and water oxygen for the four different 1 M salt solutions NaF, NaCl, NaBr and NaI are almost indistinguishable. The vertical dashed lines at the minima separate the 1st, 2nd and 3rd water solvation shells. For iodide the force field I(4) is used. (B) The first maximum of the radial distribution functions $g_{-,O}(r)$ between the anions and water oxygen progressively moves to smaller distances as the bare anion size decreases. The orange/black vertical dashed lines denote the minima for F and Cl, respectively, the minima for Br and I are similar to Cl and not shown. (C) The anion-cation radial distribution functions $g_{Na,-}(r)$ show the typical crossover from contact-ion-pairing for Cl, Br, I to solvent-separated ion pairing for F. The positions of the first three minima (denoted by vertical dashed lines) define the different ion-pair configurations as schematically indicated in (D): contact ion pairs (CIP), single solvent-separated ion pairs (SIP), doubly solvent-separated ion pairs (DSIP) and free ions (FI). The orange lines denote the minima for NaF, the black ones for NaCl, the minima for NaBr and NaI are similar to NaCl and not shown. (E) The ion-pair number fractions n_I^k, which are normalized according to $\sum_k n_I^k = 1$, are dominated by solvent-separated ion pairs (SIP) for all studied solutions. (F) Number fractions of the different solvation water components n_W^k. Note that the n_W^k components are normalized with respect to pure water and therefore $\sum_k n_W^k \neq 1$, see text. First solvation-shell water is labeled by W1 and further decomposed into the different ion-pair configurations, second and third-shell solvation water is denoted by W2 and W3, respectively.

The number fraction of water in different solvation layers, denoted by n_W^k, is normalized with respect to the equivalent number of water molecules in pure water, $\sum_k n_W^k = N_W/N_{bulk}$. Here N_W is the actual number of water molecules in the simulation of a salt solution while $N_{bulk} = V \rho_{bulk}$ is the equivalent number of water molecules in pure water in the same volume V and with bulk number density $\rho_{bulk} = 33.4\,\mathrm{nm}^{-3}$. Due to the finite volume of the ions in solution and due to non-ideal mixing effects, the sum $\sum_k n_W^k$ is not equal to unity, so by dividing the spectral water contributions by n_W^k we eliminate trivial water dilution effects and can therefore extract a meaningful spectral contribution per water molecule. The running index k distinguishes first, second and third (and beyond) solvation shells, in part of our analysis the first shell is further decomposed depending on the ion-pair state. Figure 2.1 F shows that for 1 M solutions about 20% of the water is first solvation-shell water, and that the largest contribution to the first solvation shell comes not surprisingly from the single solvent-separated ion pairs, reflecting that these ions dominate the ion-pair fractions n_I^k shown in Figure 2.1 E. Note that in determining the number fractions n_W^k the state k of a water molecule is defined by the closest ion.

2.2.3 Decomposition of Dielectric Spectra

To analyze the different dielectric contributions of water hydration shells and ion-pair states we decompose the polarization and current correlation functions according to

$$\phi_{\mathrm{W}}^{k}(t) = \frac{\langle \vec{P}_{\mathrm{W}}(0) \cdot \vec{P}_{\mathrm{W}}^{k}(t) \rangle}{3V k_B T \epsilon_0} \tag{2.13}$$

$$\phi_{\mathrm{IW}}^{k}(t) = \frac{1}{2} \frac{\langle \vec{P}_{\mathrm{W}}^{k}(0) \cdot \vec{J}_{\mathrm{I}}(t) - \vec{J}_{\mathrm{I}}(0) \cdot \vec{P}_{\mathrm{W}}^{k}(t) \rangle}{3V k_B T \epsilon_0} \tag{2.14}$$

$$\phi_{\mathrm{I}}^{k}(t) = \frac{\langle \vec{J}_{\mathrm{I}}(0) \cdot \vec{J}_{\mathrm{I}}^{k}(t) \rangle}{3V k_B T \epsilon_0}, \tag{2.15}$$

where the index k in $\phi_{\mathrm{W}}^{k}(t)$ and $\phi_{\mathrm{IW}}^{k}(t)$ stands for the previously defined different water solvation shells and in $\phi_{\mathrm{I}}^{k}(t)$ for the different ion-pair states. Note that this decomposition is not unique, but allows to extract systematic trends and mechanistic insight in a straightforward fashion. By construction, the sums over the index k return the total correlation functions defined previously in equations 2.3-2.5, $\phi_{\mathrm{W}}(t) = \sum_k \phi_{\mathrm{W}}^{k}(t)$, $\phi_{\mathrm{IW}}(t) = \sum_k \phi_{\mathrm{IW}}^{k}(t)$, $\phi_{\mathrm{I}}(t) = \sum_k \phi_{\mathrm{I}}^{k}(t)$.

The decomposed dielectric spectral contributions follow in analogy to equations 2.10-2.12 as

$$\chi_{\mathrm{W}}^{k}(f) = \phi_{\mathrm{W}}^{k}(0) - i2\pi f \int_0^\infty e^{-2\pi i f t} \phi_{\mathrm{W}}^{k}(t) \mathrm{d}t \tag{2.16}$$

$$\chi_{\mathrm{IW}}^{k}(f) = -2 \int_0^\infty e^{-2\pi i f t} \phi_{\mathrm{IW}}^{k}(t) \mathrm{d}t \tag{2.17}$$

$$\Delta\chi_{\mathrm{I}}^{k}(f) = -\frac{i}{2\pi f} \int_0^\infty (e^{-2\pi i f t} - 1) \phi_{\mathrm{I}}^{k}(t) \mathrm{d}t \tag{2.18}$$

and the decomposed pure ionic contributions to the conductivity are in analogy to equation 2.8 given by

$$\sigma_{\mathrm{I}}^{k}(f) = \int_0^\infty e^{-2\pi i f t} \phi_{\mathrm{I}}^{k}(t) \mathrm{d}t. \tag{2.19}$$

Explicitly, the water dielectric contribution $\chi_{\mathrm{W}}(f)$ is thus split into a total of six different terms, first into the three water solvation shells, $\chi_{\mathrm{W}}(f) = \chi_{\mathrm{W1}}(f) + \chi_{\mathrm{W2}}(f) + \chi_{\mathrm{W3}}(f)$, and the first-solvation-shell contribution further into the four different ion-pair contributions according to

$$\chi_{\mathrm{W1}}(f) = \chi_{\mathrm{W1CIP}}(f) + \chi_{\mathrm{W1SIP}}(f) + \chi_{\mathrm{W1DSIP}}(f) + \chi_{\mathrm{W1FI}}(f). \tag{2.20}$$

2.2.4 Full Derivation of the Relation between Dielectric Functions and Polarization Correlation Functions

The derivation closely follows Caillol et al.[70]. Starting point is the defining relation for the electric susceptibility $\chi(f)$ relating the polarization $\vec{P}(f) = \chi(f)\epsilon_0 \vec{E}(f)$ with the electric field $\vec{E}$ (vector

arrows are skipped for clarity in the following derivation),

$$\chi(f) = \frac{1}{3Vk_BT\epsilon_0}\int_0^\infty e^{-2\pi ift}\langle P(0)\dot{P}(-t)\rangle \mathrm{d}t = -\frac{1}{3Vk_BT\epsilon_0}\int_0^\infty e^{-2\pi ift}\langle P(0)\dot{P}(t)\rangle \mathrm{d}t, \quad (2.21)$$

where we have used $P(0)\dot{P}(-t) = -P(0)\dot{P}(t)$, since $\dot{P}(t)$ is antisymmetric and $P(t)$ is symmetric under time-reversal. In a salt solution the total polarization $P(t) = P_\mathrm{W}(t) + P_\mathrm{I}(t)$ has two parts: The first part $P_\mathrm{W}(t)$ is the total polarization of the water molecules, which poses no problems in a simulation employing periodic boundary conditions. The total polarization of the ion distribution however depends on the position of the bounding box and gives rise to spurious effects when ions traverse the simulation box boundaries. Therefore we use the ionic current $J_\mathrm{I}(t) = \dot{P}_\mathrm{I}(t)$ instead,

$$\chi(f) = -\frac{1}{3Vk_BT\epsilon_0}\int_0^\infty e^{-i2\pi ift}\langle (P_\mathrm{W}(0) + P_\mathrm{I}(0))(\dot{P}_\mathrm{W}(t) + J_\mathrm{I}(t))\rangle \mathrm{d}t, \quad (2.22)$$

which can be split into three contributions according to $\chi(f) = \chi_\mathrm{W}(f) + \chi_\mathrm{IW}(f) + \chi_\mathrm{I}(f)$. We obtain

$$\chi_\mathrm{W}(f) = -\frac{1}{3Vk_BT\epsilon_0}\int_0^\infty e^{-2\pi ift}\langle P_\mathrm{W}(0)\dot{P}_\mathrm{W}(t)\rangle \mathrm{d}t \quad (2.23)$$

$$= \frac{1}{3Vk_BT\epsilon_0}\left[\langle P_\mathrm{W}^2(0)\rangle - i2\pi f\int_0^\infty e^{-2\pi ift}\langle P_\mathrm{W}(0)P_\mathrm{W}(t)\rangle \mathrm{d}t\right] \quad (2.24)$$

$$= \phi_\mathrm{W}(0) - i2\pi f\int_0^\infty e^{-2\pi ift}\phi_\mathrm{W}(t)\mathrm{d}t \quad (2.25)$$

$$\chi_\mathrm{IW}(f) = -\frac{1}{3Vk_BT\epsilon_0}\int_0^\infty e^{-2\pi ift}\langle P_\mathrm{W}(0)\dot{P}_\mathrm{I}(t) + P_\mathrm{I}(0)\dot{P}_\mathrm{W}(t)\rangle \mathrm{d}t \quad (2.26)$$

$$= \frac{1}{3Vk_BT\epsilon_0}\left[2\langle P_\mathrm{W}(0)P_\mathrm{I}(0)\rangle + \int_0^\infty \langle P_\mathrm{W}(0)P_\mathrm{I}(t) + P_\mathrm{I}(0)P_\mathrm{W}(t)\rangle\frac{\mathrm{d}}{\mathrm{d}t}\left(e^{-2\pi ift}\right)\mathrm{d}t\right]$$

$$= \frac{1}{3Vk_BT\epsilon_0}\left[2\langle P_\mathrm{W}(0)P_\mathrm{I}(0)\rangle + 2\int_0^\infty \langle P_\mathrm{W}(0)P_\mathrm{I}(t)\rangle\frac{\mathrm{d}}{\mathrm{d}t}\left(e^{-2\pi ift}\right)\mathrm{d}t\right] \quad (2.27)$$

$$= -\frac{2}{3Vk_BT\epsilon_0}\int_0^\infty e^{-2\pi ift}\langle P_\mathrm{W}(0)J_\mathrm{I}(t)\rangle \mathrm{d}t \quad (2.28)$$

$$= -2\int_0^\infty e^{-2\pi ift}\phi_\mathrm{IW}(t)\mathrm{d}t, \quad (2.29)$$

where we used that $P_W(0)P_I(t)$ is even under time-reversal in equation 2.27.

$$\chi_I(f) = -\frac{1}{3Vk_BT\epsilon_0}\int_0^\infty e^{-2\pi ift}\langle P_I(0)J_I(t)\rangle\mathrm{d}t \tag{2.30}$$

$$= \frac{1}{3Vk_BT\epsilon_0}\int_0^\infty e^{-2\pi ift}\langle J_I(0)P_I(t)\rangle\mathrm{d}t \tag{2.31}$$

$$= \frac{i}{3Vk_BT\epsilon_0 2\pi f}\int_0^\infty \langle J_I(0)P_I(t)\rangle\frac{\mathrm{d}}{\mathrm{d}t}\left(e^{-2\pi ift}\right)\mathrm{d}t \tag{2.32}$$

$$= \frac{i}{3Vk_BT\epsilon_0 2\pi f}\left[-\langle P_I(0)J_I(0)\rangle - \int_0^\infty e^{-2\pi ift}\langle J_I(0)J_I(t)\rangle\mathrm{d}t\right]$$

$$= -\frac{i}{3Vk_BT\epsilon_0 2\pi f}\int_0^\infty e^{-2\pi ift}\langle J_I(0)J_I(t)\rangle\mathrm{d}t \tag{2.33}$$

$$= -\frac{i}{2\pi f}\int_0^\infty e^{-2\pi ift}\phi_I(t)\mathrm{d}t, \tag{2.34}$$

where we used that $P_I(0)J_I(t)$ is odd under a time-reversal and thus $P_I(0)J_I(0) = 0$ in equation 2.33. The imaginary part of $\chi_I(f)$ diverges in the low-frequency limit because of a finite ionic DC conductivity. The ionic conductivity $\sigma(f)$ is by convention the electric current response of free charges to an electric field,

$$\sigma(f) = \frac{1}{3Vk_BT\epsilon_0}\int_0^\infty e^{-2\pi ift}\langle J_I(t)\dot{P}(0)\rangle\mathrm{d}t = \frac{1}{3Vk_BT\epsilon_0}\int_0^\infty e^{-2\pi ift}\langle J_I(0)\dot{P}(t)\rangle\mathrm{d}t \tag{2.35}$$

$$= \frac{1}{3Vk_BT\epsilon_0}\int_0^\infty e^{-2\pi ift}\langle J_I(0)\left(\dot{P}_W(t) + \dot{P}_I(t)\right)\rangle\mathrm{d}t \tag{2.36}$$

$$= \frac{1}{3Vk_BT\epsilon_0}\left[\langle J_I(0)P_W(0)\rangle - i2\pi f\int_0^\infty e^{-2\pi ift}\langle P_W(0)J_I(t)\rangle\mathrm{d}t + \int_0^\infty e^{-2\pi ift}\langle J_I(0)J_I(t)\rangle\mathrm{d}t\right]$$

$$= \frac{1}{3Vk_BT\epsilon_0}\left[-i2\pi f\int_0^\infty e^{-2\pi ift}\langle P_W(0)J_I(t)\rangle\mathrm{d}t + \int_0^\infty e^{-2\pi ift}\langle J_I(0)J_I(t)\rangle\mathrm{d}t\right] \tag{2.37}$$

$$= -i2\pi f\int_0^\infty e^{-2\pi ift}\phi_{IW}(t)\mathrm{d}t + \int_0^\infty e^{-2\pi ift}\phi_I(t)\mathrm{d}t. \tag{2.38}$$

By comparison with equations 2.29 and 2.34 it is seen that $\sigma(f) = i2\pi f\left[\chi_I(f) + 0.5\chi_{IW}(f)\right]$. The static conductivity $\sigma_0 = \sigma(f = 0)$ depends only on the ion-current auto-correlation,

$$\sigma_0 = \frac{1}{3Vk_BT\epsilon_0}\int_0^\infty \langle J_I(0)J_I(t)\rangle\mathrm{d}t = \int_0^\infty \phi_I(t)\mathrm{d}t. \tag{2.39}$$

By adding the term $i\sigma_0/(2\pi f)$ to $\chi_I(f)$ the divergence is lifted and we obtain

$$\Delta\chi_I(f) \quad = \quad \chi_I(f) + i\sigma_0/(2\pi f) \tag{2.40}$$

$$= \quad -\frac{i}{3Vk_BT\epsilon_0 2\pi f}\int\limits_0^\infty (e^{-2\pi ift} - 1)\langle J_I(0)J_I(t)\rangle\mathrm{d}t. \tag{2.41}$$

The dielectric spectrum that is typically reported in experiments is the non-diverging expression $\Delta\chi(f) = \chi(f) + i\sigma_0/(2\pi f) = \chi_W(f) + \chi_{IW}(f) + \Delta\chi_I(f)$.

2.2.5   Simulation Methods

We use GROMACS 4.5.4[71] to simulate three separate trajectories of duration $100\,\mathrm{ns}$ each for the salt types NaCl, NaBr and NaI, for bulk water only one and for NaF five trajectories are simulated. The simulation box contains about 7000 water molecules and 130 ion pairs (for the $1\,\mathrm{M}$ solutions) in the NPT ensemble at $300\,\mathrm{K}$, employing the Nose-Hoover thermostat implemented in GROMACS and a $2\,\mathrm{fs}$ integration time step. The neighbor list is updated every $20\,\mathrm{fs}$ and trajectories are saved every $10\,\mathrm{fs}$. Electrostatics are computed by Particle-Mesh-Ewald methods and the Lennard-Jones interactions are subject to a switch cutoff between 1.1 and $1.2\,\mathrm{nm}$. We use the SPC/E water model[78] and our previously optimized ion force fields with non-standard mixing rules[82] for fluoride and iodide. Note that these ion force fields have been simultaneously optimized with respect to the single-ion solvation free energy and the activity coefficients of different ion pairs, for iodide two distinct force fields were reported that both satisfied the equilibrium optimization procedure equally well[82]. In the present work we compare both force fields for iodide with experimental dielectric spectra and therefore perform an additional optimization step based on dynamic and static dielectric properties, as will be discussed further below. Because of memory limitations all trajectories are split into series of $20\,\mathrm{ns}$ length during data analysis. The polarization components of each time series are Fourier transformed via Fast Fourier Transformation (FFT). Correlation functions are calculated by multiplication in Fourier space according to the convolution theorem. After back transformation into the time domain the correlations are averaged over different time series. We update the decomposition of water and ions into different solvation-shell and ion-pair states every $10\,\mathrm{fs}$, consequently, the ensemble of tagged molecules changes in time. Since the diffusion of ions and water molecules is slower than the polarization fluctuations, the fluctuating ensembles corresponding to different solvation shells and ion-pair states do not influence the resulting spectra and correlation functions on the frequency or time scales of interest. An upper time cutoff is imposed on the Laplace transform of the correlation functions during calculation of the spectra, as is discussed in detail in Appendix B.1.

2.3   Comparison with Experimental Dielectric Spectra

In Figure 2.2 we compare Buchner's experimental results[53] for the dielectric spectra of NaCl solutions at different concentrations with our simulation results. In Figure 2.2 on the left side we

	simulation			experiment[53, 54, 55]			
	ϵ_{CC}	τ_{CC} [ps]	α	ϵ_{CC}	τ_{CC} [ps]	α	ϵ_∞
water	69.9	10.72	0.014	78.4	8.27	0.000	5.87
1 M NaF	56.8	9.65	0.042	*67.8	*8.28	*0.036	*4.96
0.5 M NaCl	61.1	9.75	0.030	71.7	7.79	0.023	5.65
1 M NaCl	53.6	9.10	0.047	66.6	7.47	0.041	5.65
2 M NaCl	43.4	8.71	0.085	58.3	7.06	0.057	5.65
1 M NaBr	52.6	9.23	0.058	66.6	7.55	0.032	5.64
1 M NaI(4)	51.5	9.07	0.056	65.5	7.19	0.039	5.05

TABLE 2.1: Cole-Cole fit parameters to our simulation spectra and the experimental spectra measured by Buchner et al. *Experimental Cole-Cole fit parameters for 0.86 M NaF were received in a private communication by R. Buchner and linearly extrapolated to 1 M.
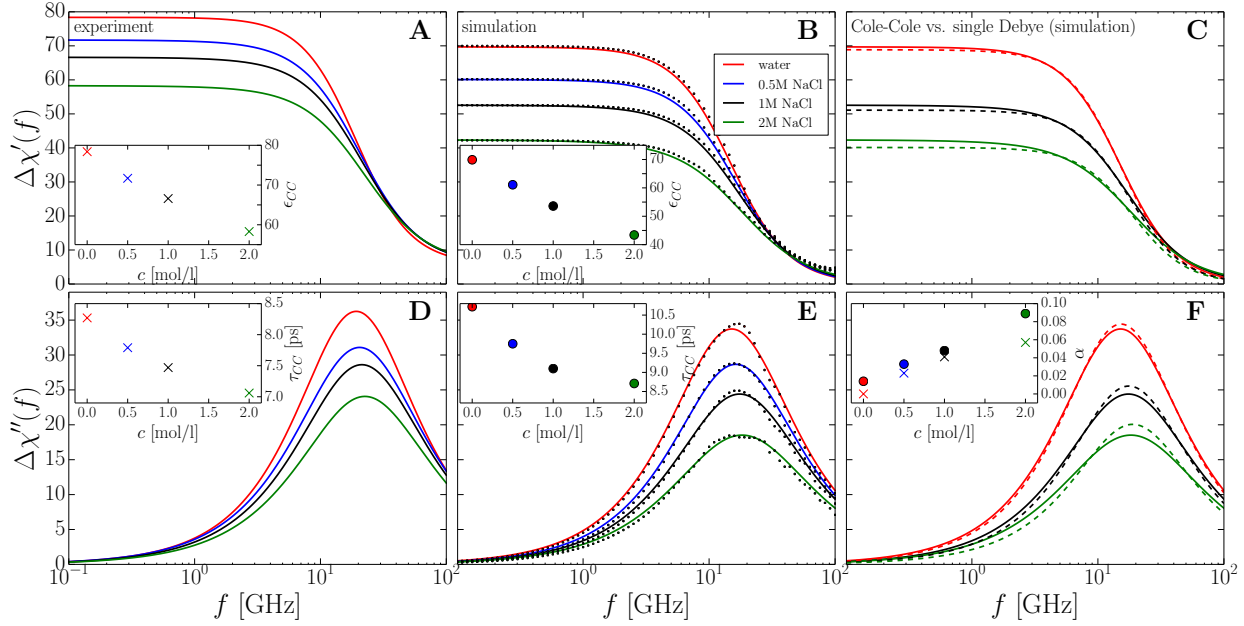

FIGURE 2.2: Comparison of experimental and simulated dielectric spectra of NaCl solutions at matching concentrations $c = 0, 0.5, 1,$ and 2 M. (A) and (D): Experimental Cole-Cole fits of the real and imaginary parts of the dielectric susceptibility $\Delta\chi'(f)$ and $\Delta\chi''(f)$, reproduced from Buchner et al.[53]. The red lines show the results for pure water ($c = 0$ M). The dielectric constant ϵ_{CC} in the inset in (A), as obtained from the amplitude of the Cole-Cole fits, decreases as a function of NaCl concentration. The corresponding experimental relaxation time τ_{CC} in the inset in (D) exhibits a characteristic blue-shift to shorter times with rising NaCl concentration. (B) and (E) show the simulated real and imaginary parts of the dielectric susceptibility, points correspond to simulation data and lines are the Cole-Cole fits for different NaCl concentrations, including pure water (red lines). The insets again show the dielectric constant ϵ_{CC} and the relaxation time τ_{CC} as a function of NaCl concentration, which reproduce the experimental trends. (C) and (F) compare Cole-Cole fits (solid lines) and single Debye fits (dashed lines) of the simulation data. The inset in (F) shows the Cole-Cole exponent α, which is a measure of the deviations from a simple Debye form, as a function of salt concentration extracted from the experimental fits[53] (crosses) and from the simulation data (filled symbols).

reproduce the experimentally determined Cole-Cole fits to experimental data[53] according to

$$\Delta\chi(f) + 1 \quad = \quad \frac{\epsilon_{CC} - \epsilon_\infty}{1 + (i\,2\pi f\tau_{CC})^{1-\alpha}} + \epsilon_\infty, \tag{2.42}$$

Figure 2.2 A shows the real part while Figure 2.2 D shows the imaginary part of the dielectric function, the latter part corresponding to the absorption spectrum. We also include the spectrum of pure water (shown in red) and plot the amplitude ϵ_{CC} and the characteristic relaxation time τ_{CC} as a function of concentration in the insets. Increasing salt concentration lowers the dielectric constant ϵ_{CC}, a trend that is well-known and rationalized in terms of the so called dielectric saturation effect[110, 111, 112, 113], we will come back to this interpretation further below. At the same time, increasing salt concentration decreases the relaxation time and leads to a significant blue-shift, we will further below argue this shift to be mostly due to strongly bound water in the first solvation shell. In the analysis of our simulation data we fit the real and imaginary parts of the dielectric spectrum simultaneously with the error functional $(\Delta\epsilon')^2 + (2\Delta\epsilon'')^2$ using a logarithmic distribution of sample frequencies in the range between 0.1 and 100 GHz. In order to roughly achieve the same relative errors for real and imaginary parts, we use a higher weight for the imaginary part, since it has a lower absolute value. For the simulation data we use $\epsilon_\infty = 1$ in the Cole-Cole fitting function (equation 2.42), reflecting that the used classical force field does not include atomic polarizabilities. In Figures 2.2 B and E we show the real and imaginary parts of the dielectric function, dots correspond to simulation data, solid lines are Cole-Cole fits (fit parameters are listed in Table 2.1). The fits are of very high quality, the same holds also for the decomposed spectra we present further below, so for clarity of presentation we in this chapter sometimes present only the Cole-Cole fits of our simulation data. The concentration dependence of the amplitude ϵ_{CC} and the characteristic relaxation time τ_{CC} in the insets in Figures 2.2 B and E show a very similar trend as the experimental data in Figures 2.2 A and D, namely a decrease of both the dielectric constant as well as the relaxation time with increasing salt concentration. While the decrement of the dielectric constant in simulations, $\epsilon_{CC} = 69.9$ for $c = 0\,\text{mol/l}$ to $\epsilon_{CC} = 43.4$ for $c = 2\,\text{mol/l}$ NaCl, is only slighter higher than in experiments, which gives $\epsilon_{CC} = 78.4$ for $c = 0\,\text{mol/l}$ and $\epsilon_{CC} = 58.3$ for $c = 2\,\text{mol/l}$ NaCl, the overall dielectric constant is lower in simulations compared to experiments. Similarly, the change of the relaxation time upon increase of salt concentration is similar in simulations compared to experiments, while the overall relaxation time in simulations is larger by about 2 ps compared to experiments. It transpires that the disagreement between experiments and simulations mainly reflects a deficiency of the SPC/E water model, which is well known and amply documented in literature for the static dielectric properties[81, 114, 115]. As a side remark we note that previous simulations of NaCl solutions in SPC/E water give a somewhat better agreement of the simulated spectra with experimental data[99], but it seems that this is spurious and caused by an incorrect treatment of the ion-water cross-polarization term, as we will discuss further below.

Overall, the ion-dependent changes of the simulated spectra match experimental data quite well, both the change in dielectric strength and in relaxation time are reproduced remarkably well. The simulation data (dots in Figures 2.2 B and E) are well described by Cole-Cole fits, which demonstrates that the Cole-Cole fitting parameters constitute a useful set to describe simulated dielectric spectra. The deviations of the simulated data from the simple Debye form (obtained by setting $\alpha = 0$ in equation 2.42) increase with salt concentration, this is demonstrated in Figures 2.2 C and F where we compare Debye fits (broken lines) with Cole-Cole fits (solid lines). The inset of
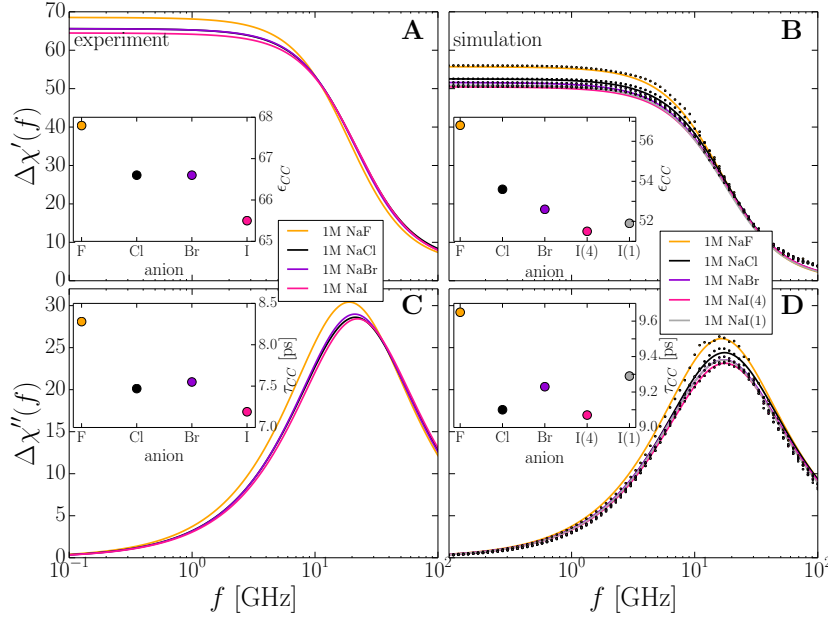
FIGURE 2.3: Comparison of experimental and simulated dielectric spectra of NaF, NaCl, NaBr and NaI solutions at concentration $c = 1\,\text{M}$. (A) and (C): Experimental Cole-Cole fits of the real and imaginary parts of the dielectric susceptibility $\Delta\chi'(f)$ and $\Delta\chi''(f)$ for the different salt types, reproduced from Buchner et al.[53, 54, 55]. The dielectric constant ϵ_{CC} in the inset in (A), as obtained from the amplitude of the Cole-Cole fits, decreases with increasing size of the anion, with the exception of Br. The corresponding experimental relaxation time τ_{CC} in the inset in (C) shows a similar trend: Larger anions are characterized by smaller relaxation times. (B) and (D) show the simulated real and imaginary parts of the dielectric susceptibility, points correspond to simulation data and lines are Cole-Cole fits for the different salt types. The insets again show the dielectric constant ϵ_{CC} and the relaxation time τ_{CC} for the different salt types. Note that results for two different force fields for iodide are shown, the force field combination NaI(4) reproduces the experimental trends much better.

Figure 2.2 F shows the Cole-Cole exponent α as a function of salt concentration, where circles denote simulation and crosses experimental results, α quantifies spectral deviations from the Debye form. We see that while pure water in simulation shows almost Debye-type dielectric relaxation, characterized by $\alpha = 0.014$, the higher concentrated NaCl solutions exhibit significantly larger α values and thus pronounced deviations from simple Debye relaxation. A naive interpretation would be that the deviations from simple Debye-type relaxation are caused by the superposition of water and ionic relaxation processes at different relaxation frequencies, our decomposition analysis demonstrates that this naive interpretation is not in agreement with a more detailed analysis of the data.

To study ion specific effects on the dielectric relaxation, we in addition simulated NaF, NaBr and NaI solutions at fixed concentration $c = 1\,\text{M}$. In Figure 2.3 (left side) we show the matching experimental Cole-Cole fits reproduced from Buchner et al.[53, 54, 55] for the real part (A) and the imaginary part (C) of the dielectric function. The experimental data show a clear ion-specific trend, NaF (orange lines) has the strongest and NaI (pink lines) the weakest dielectric signal, which is most clearly presented in the inset of Figure 2.3 A where we plot the dielectric constant ϵ_{CC} for the four different salt types. A similar ion-specific trend is observed for the relaxation time τ_{CC} which is plotted in the inset of Figure 2.3 C, the smallest anion F leads to the longest relaxation while the largest anion I gives rise to the fastest relaxation. The simulation data in Figures 2.3 B and D exhibit very similar behavior, except an offset the dielectric constant ϵ_{CC} in the inset of Figure 2.3 B

and the relaxation time τ_{CC} in the inset of Figure 2.3 D reproduce the experimental trends very well. The offsets are similar to the data for pure water shown in Figure 2.2, so similarly to our discussion of the salt-concentration dependent data above, we conclude that the disagreement between experimental and simulation data for the different ions is mostly caused by deficiencies of the water model. Note that the static dielectric constants we obtain in our simulations are sightly lower than obtained indirectly from ionic distribution functions in earlier work[108].

In our simulations we use two distinct force fields for iodide, the results are slightly different and denoted by NaI(4) and NaI(1) in Figures 2.3 B and D. These force fields were found to be of equal quality in our previous ion force-field optimization studies based on the simultaneous matching of experimental single-ion solvation free energies and activity coefficients[82], in other words, the two iodide force fields are degenerate with respect to the static properties employed in our optimization. A comparison of the simulated and experimental dielectric constants ϵ_{CC} and relaxation times τ_{CC} in the insets of Figure 2.3 show that force field I(4) performs significantly better compared to force field I(1). We conclude that based on the combined static and dynamic experimental data for dielectric relaxation times, dielectric constants, single-ion solvation free energies and activity coefficients force field I(4) is superior to force field I(1), including dielectric properties thus lifts the degeneracy of the two iodide force fields. Our force fields even reproduce the weak irregularity of bromide, which experimentally has a slightly larger relaxation time than both chloride and iodide, see Figures 2.3 C and D. This might be interpreted in favor of the force fields used by us in the present study, though we hasten to add that for the dielectric constant our simulation data for Br does not reproduce the similar irregularity in the experimental data, see Figures 2.3 A and B.

All in all we conclude that the simulation data reproduce the ion-specific trends of the dielectric relaxation spectra in a remarkably accurate fashion, which serves as a validation of both our force fields and the simulation technology, and therefore warrants our more detailed ion-specific analysis of the water and ion relaxation contributions.

2.4   Spectral Contribution of Water-Water Correlations

In Figures 2.4 A and B we show the spectral decomposition of the real and imaginary dielectric functions for 2 M NaCl into the contributions from the three solvation shells, W1, W2, and W3, the ion-water cross-term (IW) and the ion-ion term (I), note that the latter contribution is multiplied by a factor of five for better visibility. Solid lines show Cole-Cole fits and dashed lines show single Debye fits to our simulation data. The sum of all five contributions reproduces the full dielectric spectrum shown previously in Figures 2.2 B and E according to $\Delta\chi(f) = \chi_{W1}(f) + \chi_{W2}(f) + \chi_{W3}(f) + \chi_{IW}(f) + \Delta\chi_I(f)$. Most strikingly, the spectrum is dominated by the second solvation shell water contribution (W2, blue line), followed by first (W1, green line) and third shell (W3, red line) contributions. The ion-water cross-contribution (IW, yellow line) is negative and therefore significantly weakens the total dielectric response. This cross-term has been controversially discussed in literature and can be interpreted as an ionic screening effect on the water dielectric function (see Ref.[94] for a discussion and a detailed list of references). In fact, it seems that in earlier simulation work on NaCl solutions the ion-water cross-term had the incorrect sign, giving rise to a positive contribution to the total spectrum[94, 95, 99]. Although this would spuriously improve the agreement of the total spectrum with experiments, the correct sign
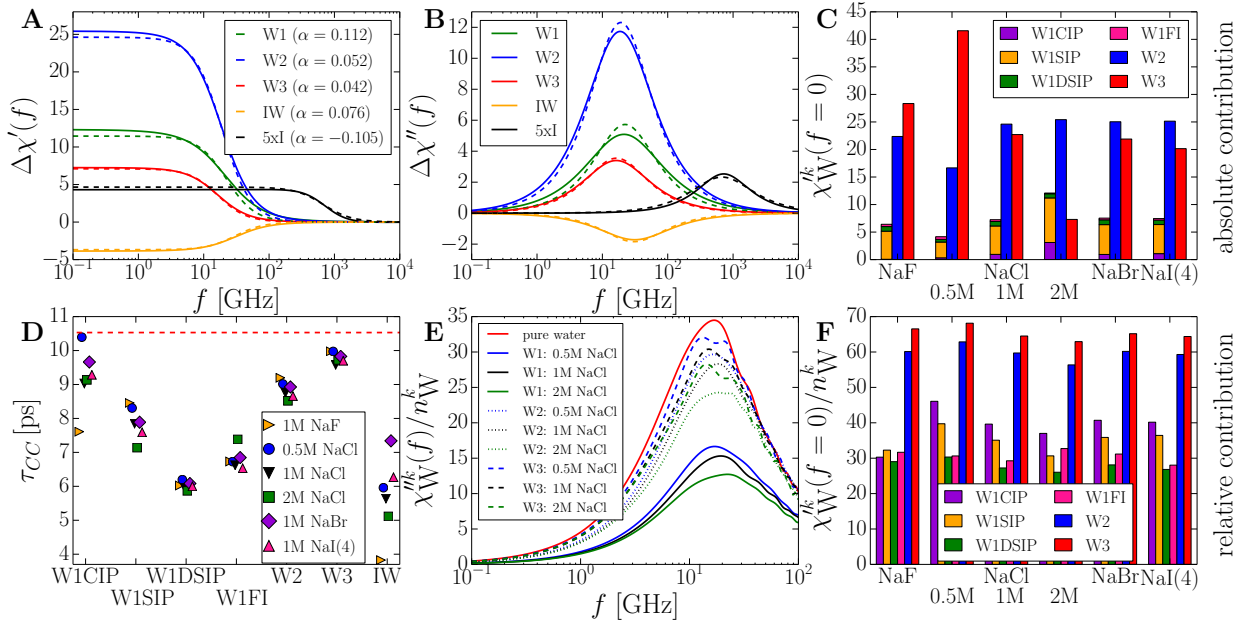
FIGURE 2.4: Simulation results for the decomposition of dielectric spectra. (A) & (B) Decomposition of the real and imaginary parts of $\Delta\chi(f)$ for $2\,\text{M}$ NaCl into contributions from the first water solvation shell W1 (green), second shell W2 (blue), third shell W3 (red), ion-water cross-contribution (IW, orange) and the ionic contribution (I, black, increased by a factor of five for better visibility). Dashed lines denote single Debye fits and solid lines are Cole-Cole fits. (C) Absolute contribution of the different water shells to the static dielectric constant for all different solutions. (D) Dielectric relaxation time τ_{CC} of the different water shells for all salt solutions, obtained from Cole-Cole fits. The horizontal red dashed line denotes the bulk water dielectric relaxation time. (E) Imaginary dielectric function per water molecule for different water solvation shells, $\chi_{\text{W}}''^k(f)/n_{\text{W}}^k$, for NaCl at different concentrations: The first solvation shell (W1, solid lines) has the weakest contribution of only about $50\,\%$ of pure water (red line). (F) Relative contribution of the different water shells to the static dielectric constant for all different salt solutions $\chi_{\text{W}}'^k(f=0)/n_{\text{W}}^k$.

used in previous[96, 101] and in the present work attenuates the dielectric response of water which is in line with an interpretation in terms of ions screening and thus weakening the water dielectric response (see section 2.2.4 for an explicit derivation of the various dielectric contributions).

The Cole-Cole exponent for the five contributions in the legend in Figure 2.4 (A) has for the given first-solvation shell water contribution W1 the value $\alpha = 0.112$, which is larger than the value for the total spectrum for $2\,\text{M}$ NaCl $\alpha = 0.085$ shown in Figure 2.2 F. Indeed, while the Cole-Cole and single-Debye fits (solid and broken lines in Figures 2.4 A and B) for the third-solvation shell water (W3, red lines) agree quite well, in line with a rather small exponent $\alpha = 0.042$, the two fitting forms show increasing deviations as one goes to the inner solvation shells. Therefore an interpretation of the non-Debye like character of the dielectric response of salt solutions as being caused by the addition of two distinct processes caused by ion and water relaxation that are each Debye-like but occur at different relaxation times is not in line with our results: Rather, our decomposition into ion, ion-water and different water-solvation shell contributions reveals that deviations from a single Debye form are caused by the intrinsic non-Debye-like character of the strongly bound solvation water in the first solvation shell around ions. This conclusion is supported by the fact that the relaxation times of the dominant dielectric contributions in Figure 2.4 B are quite similar. A further decomposition of the spectral contribution of the first solvation shell $\chi_{\text{W1}}(f)$ depending
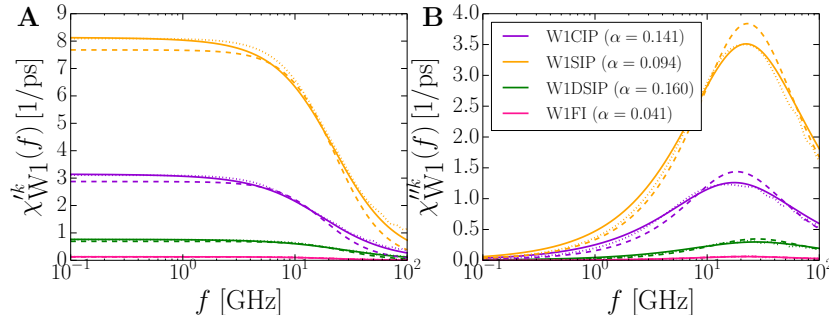
FIGURE 2.5: Decomposition of the first solvation shell water contribution to the dielectric spectrum, $\chi_{W1}(f)$, for $2\,M$ NaCl into separate contributions from solvation water of contact ion pairs (CIP, purple), solvent-separated ion pairs (SIP, orange), doubly-solvent separated ion pairs (DSIP, green) and free ions (FI, pink). Simulation data are shown by dots, single Debye fits by dashed lines and Cole-Cole fits by solid lines.

on the pair configuration of the closest ion according to

$$\chi_{W1}(f) = \chi_{W1CIP}(f) + \chi_{W1SIP}(f) + \chi_{W1DSIP}(f) + \chi_{W1FI}(f)$$

is shown for $2\,M$ NaCl in Figure 2.5. Here the simulation data are shown by dots, single-Debye fits by broken lines and Cole-Cole fits by solid lines. It is seen that the Debye fits perform rather poorly, in fact, some of the exponents for the individual contributions are even larger than the Cole-Cole exponent for the entire first-solvation shell ensemble. This means that the large deviations of the dielectric contribution due to first solvation shell water from single-Debye behavior is not a signature of different ionic environments which each are characterized by different relaxation times.

The increase of the Cole-Cole exponent α in Figure 2.2 F from $\alpha = 0.014$ for $c = 0\,M$ to $\alpha = 0.085$ for $c = 2\,M$ can therefore partly be traced back to the increase of the fraction of inner shell water n_{W1} with concentration (see Figure 2.1 F), which is characterized by a significantly higher $\alpha = 0.112$ value compared to the other solvation layers.

The absolute contribution of the different solvation-water shells $\chi_W'^k(f = 0)$ to the total static dielectric constant for all studied solutions is shown in Figure 2.4 C. This plot mostly reflects the different numbers of water molecules in the different solvation layers. More meaningful is the relative contribution $\chi_W'^k(f = 0)/n_W^k$ in Figure 2.4 F, where we rescale $\chi_W'^k(f = 0)$ by the water number fraction n_W^k. Here it is seen that the relative contribution for third shell water $\chi_{W3}'(f = 0)/n_{W3}$ is close to the bulk water value of about 70, while for second-shell water $\chi_{W2}'(f = 0)/n_{W2}$ is reduced by about 15% and for first-shell water $\chi_{W1}'(f = 0)/n_{W1}$ the relative contribution is only about half of the bulk value (note that for first-shell water we further decompose into the different ion-pair states). Since by construction the various dielectric contributions are additive, we conclude that the dielectric saturation effect in salt solutions is (apart from a trivial dilution effect because of the finite ionic volume) mainly caused be the reduction of the dielectric amplitude in the first water solvation shell around ions.

There are two distinct explanations for the dielectric decrement in salt solutions, keeping in mind that the dielectric spectrum is dominated by the water contributions and therefore also the decrement must be related to how water reacts to the presence of ions in the solution: The first explanation rationalizes the decrease of the water polarizability by water orientation in the ionic

electric fields, a mechanism usually called dielectric saturation. This explanation neglects correlations between water molecules and rather invokes a single-dipole picture: Clearly, in an orienting electric field, the polarizability of a single dipole decreases. The second explanation is less intuitive but explicitly considers the effect of correlations between water molecules on the dielectric response. According to the Madden-Kivelson-theory[92] the Kirkwood factor g_K, which is the dielectric enhancement factor due to correlations between water molecules[116], is linearly related to the relaxation time. For water g_K is known to be high and of the order of $g_K \simeq 2.3$[117], so a decrease of the dielectric contribution of the first solvation shell can alternatively be interpreted as being caused by a loss of correlations between water molecules. This interpretation is reasonable in light of the perturbing influence of an ion on the local water structure. To obtain further evidence for this decorrelation effect, we in Figure 2.4 D show the relaxation times τ_{CC} of all individual water solvation shells for all studied salt solutions. Different salts and different concentrations for NaCl show quite similar behavior and a clear trend: Third solvation shell water W_3 has a relaxation time similar to bulk water (shown as a broken horizontal line), the second shell water W_2 has a substantially reduced relaxation time, and the relaxation time of water in the first solvation shell (except around contact-ion-pair ions W1CIP) is even further reduced. This decomposition therefore demonstrates that the blue shift of the dielectric spectra of salt solutions mainly comes from a blue shift of first-solvation water shell. Note that the relaxation time of first-solvation shell water progressively increases for ions that are bound to each other more closely, i.e., as one goes from doubly-solvent separated ion pairs (W1DSIP) over solvent-separated ion pairs (W1SIP) to contact ion pairs (W1CIP). This trend correlates very nicely with the results for the dielectric constant per water molecule for the different water solvation types in Figure 2.4 F. Our data thus show a good correlation between relaxation times and dielectric constants for the different water solvation layers in qualitative agreement with the Madden-Kivelson-theory originally derived for homogeneous liquids, we thus conclude that the dielectric decrement observed in salt solutions is in line with a decorrelation mechanism of water in the first and also in the second solvation shell around ions. We note that this does not rule out that also dielectric saturation plays a role in our systems, because the relaxation time of a single dipole in a strong external electric field is also expected to go down. But since correlation effects are dominant for liquid water, as witnessed by the large Kirkwood factor of $g_K \simeq 2.3$ in bulk water, we argue that a single dipole picture is not applicable in order to understand the dielectric decrement in salt solutions.

In Figure 2.4 E we plot the imaginary dielectric function per water molecule $\chi_W'^k(f = 0)/n_W^k$ for the three water solvation shells W1, W2 and W3 for NaCl at the three different concentrations $c = 0.5, 1, 2\,\mathrm{M}$ and compare with the corresponding result for pure water (red solid line). We see that the spectral contribution of the third solvation shell W3 is almost bulk-like, while distinct deviations are discerned for W2. The spectrum of the first solvation shell W1 (solid lines) is reduced to about half the bulk value and the blue shift, which is more clearly seen in Figure 2.4 D, can already be discerned. Interestingly, the outer shell spectra W2 and W3 converge to the bulk curve for high frequencies, meaning that deviations between bulk and solvation water mostly concerns slow, low-frequency processes.

A decomposition of experimental spectra into three single Debye processes often leads to a slow ionic, a dominant bulk water-like and fast water process with relaxations times separated by more than one order of magnitude[55]. In our simulations the differences are smaller, since the fastest
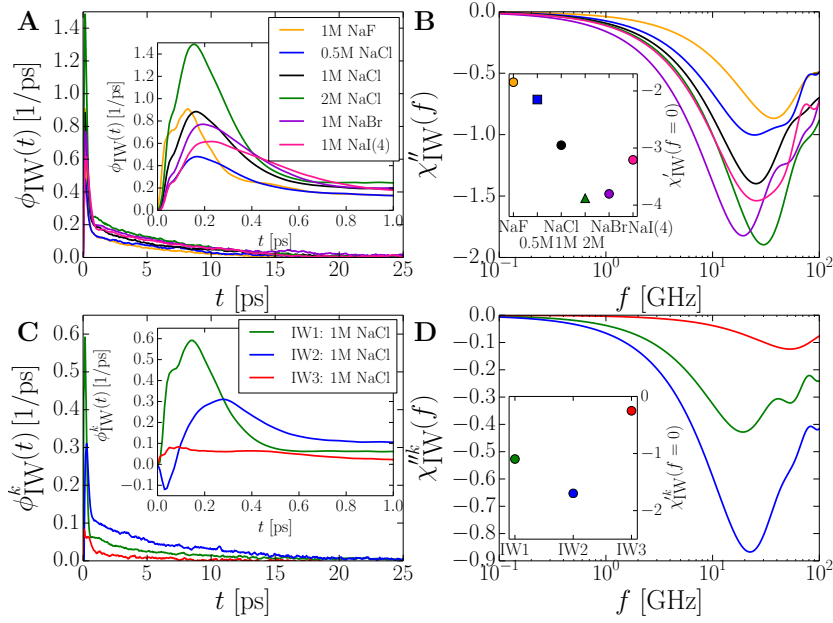
FIGURE 2.6: Detailed analysis of ion-water cross-correlations: (A) The ion-water cross-correlation function $\phi_{\text{IW}}(t)$ exhibits a fast drop over less than a picosecond followed by a much slower decrease. The inset shows the short-time behavior and demonstrates that $\phi_{\text{IW}}(t)$ is antisymmetric for all studied salt solutions. (B) Imaginary part of the ion-water dielectric contribution $\chi''_{\text{IW}}(f)$ for all studied salts. The inset shows the static real dielectric contribution $\chi'_{\text{IW}}(f=0)$. Real as well as imaginary parts are negative and thus decrease the total dielectric response function. (C) Ion-current cross-correlation functions $\phi^k_{\text{IW}}(t)$ for different water shells for 1 M NaCl. The inset shows the short-time behavior and demonstrates that the first shell (green line) reaches its maximum at a shorter time compared to the second shell (blue line), while the third shell (red line) shows only negligible correlations. (D) Imaginary dielectric spectra $\chi''^k_{\text{IW}}(f)$ for different water shells for 1 M NaCl. The inset shows the static real dielectric contribution $\chi'^k_{\text{IW}}(f=0)$. The second-shell contribution IW2 dominates the frequency-dependent response function.

inner shell water (W1DSIP) is only about a factor of two faster than bulk water, as seen in Figure 2.4 D.

2.5 Detailed Analysis of Ion-Water Cross-Correlations and their Contribution

The ion-water dielectric cross-correlation function $\phi_{\text{IW}}(t)$ in Figure 2.6 A shows a steep initial decay over roughly one ps followed by a much slower relaxation. $\phi_{\text{IW}}(t)$ is odd in time, as seen more clearly in the inset, and positive for all studied solutions, reflecting that $P_{\text{W}}(0)J_{\text{I}}(t)$ is larger than $J_{\text{I}}(0)P_{\text{W}}(t)$, see equation 2.4. This is in accord with previous simulation results for various ionic liquids[97, 98] except 1-ethyl-3-methyl-imidazolium triflat ($\text{EMIM}^+\text{CF}_3\text{SO}_3^-$), where an opposite time-correlation has been reported[100]. We have reliable data for $\phi_{\text{IW}}(t)$ up to about 10 ps; this allows to calculate the spectral contribution $\chi_{\text{IW}}(f)$ in Figure 2.6 B, which is characterized by a relaxation time around $\tau_{\text{IW}} \simeq 5$ ps about a factor two faster than bulk water. We see pronounced ion specific trends in the short time behavior of $\phi_{\text{IW}}(t)$ (inset of Figure 2.6 A), for the smallest anion fluoride $\phi_{\text{IW}}(t)$ displays a maximum at the shortest time and - comparing only the 1 M solutions - has the highest amplitude and the fastest decrease. With increasing anion size the maximum
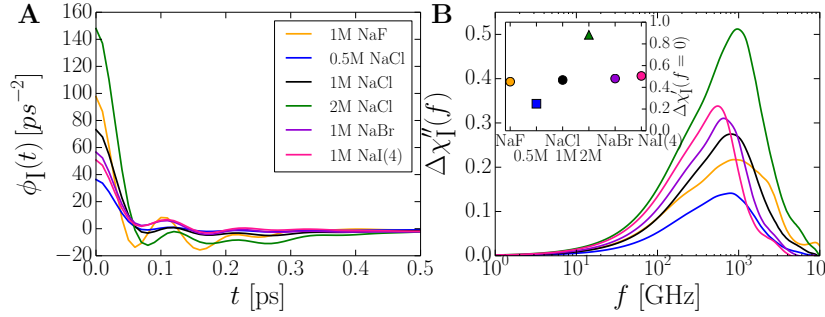
FIGURE 2.7: Detailed analysis of ion-ion correlations: (A) Ion auto-correlation functions $\phi_I(t)$ for all studied salt solutions. $\phi_I(t)$ exhibits pronounced oscillations and decreases quickly within a few hundred fs. (B) Imaginary DC-conductivity corrected dielectric ion contribution $\Delta\chi_I''(f)$ for all different salt types. The inset shows the static real contribution $\Delta\chi_I'(f = 0)$. For the 1 M solutions the ion part $\Delta\chi_I(f)$ contributes only about 1% to the total dielectric signal and can thus be neglected for all practical purposes.

is shifted to longer times. This translates into the ionic specific series of the real zero-frequency contribution $\chi_{IW}'(f = 0)$ shown in the inset of Figure 2.6 B.

By splitting up the ion-water cross-term $\phi_{IW}(t)$ into the different water shells for 1 M NaCl in Figure 2.6 C we see that the correlation between ions and first-solvation shell water IW1 dominates at the shortest time scales (as comes out from the inset), while correlations with second-solvation shell water IW2 dominate at longer times scales. Consequently, the amplitude of the spectral contribution of the ion cross-correlations with the second shell $\chi_{IW2}(f)$ exceeds $\chi_{IW1}(f)$, as shown in Figure 2.6 D for the imaginary part of the spectrum as well as for the static limit in the inset. The correlation between ions and third solvation shell water is weak and largely irrelevant. The spectral contribution of the water-ion cross-term is commonly denoted as kinetic dielectric decrement. A recent non-equilibrium study of aqueous NaCl solutions shows that the absolute value of the static decrement of the ion-water contribution does not increase monotonically with increasing salt concentration. Instead the maximum value occurs at a salt concentration of about 2M[118]. In our simulations the second solvation shell water contributes stronger to the static decrement than the first shell. Clearly, at very high concentrations most of the water will be in the first shell and only a minor part will be in the strongly contributing second shell. Therefore, the loss of second shell water might explains the smaller absolute value of the decrement at very high concentrations.

2.6   Analysis of Ion-Ion Correlations and Frequency-Dependent Conductivity

The auto-correlation function of the ion-current, $\phi_I(t)$, shown in Figure 2.7 A for all different salt types and salt concentrations, exhibits high-frequency oscillations and decreases quickly within a few hundred fs for all different salt solutions. Figures 2.4 A and B demonstrate that the ion contribution $\chi_I(f)$ is the weakest of the three main contributions to the dielectric susceptibility $\chi_W(f)$, $\chi_{IW}(f)$, and $\chi_I(f)$, and accordingly has not been included in earlier simulation studies of aqueous NaCl solutions[95, 96, 99]. We recall that the DC-conductivity correction only effects the imaginary part of $\Delta\chi_I(f)$, leading to a vanishing $\Delta\chi_I''(f)$ in the low frequency limit. As shown in Figure 2.7 B, $\Delta\chi_I''(f)$ is peaked around 1 THz, the maximum shifts to lower frequencies with increasing anion size (this is most clearly seen when comparing the different salt solution data at
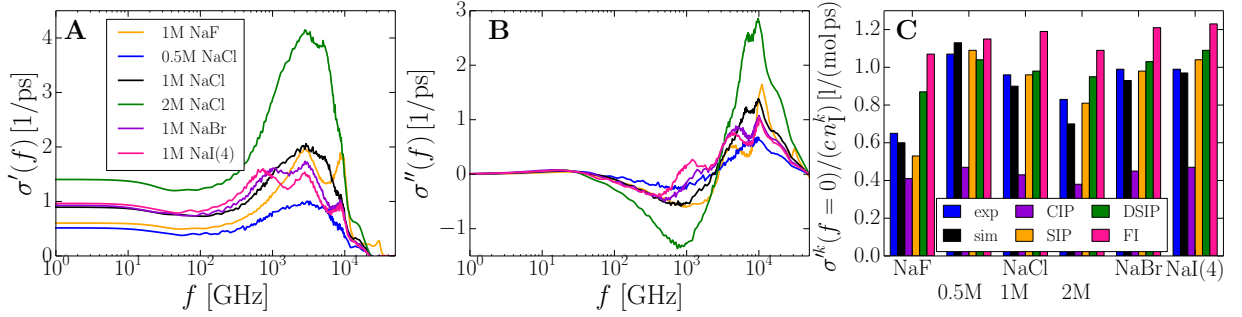
FIGURE 2.8: Analysis of the frequency dependent conductivity. (A) Real and (B) imaginary parts of the ionic conductivity $\sigma(f)$ of all studied salts. (C) Comparison of the total static conductance $\sigma(f=0)/c$ from simulations (black bars) and from experimental data[53, 54, 55] (blue bars) is favorable for all different salt solutions. The molar conductances $\sigma'^k(f=0)/(c\,n_I^k)$ of different ion-pair configurations demonstrate that contact ion pairs (CIP) have a significantly reduced conductance compared to free ions (FI), doubly solvent-separated ion pairs (DSIP) and single solvent-separated ion pairs (SIP) only show a weakly reduced conductance (except for fluoride, where also the SIP conductance is considerably reduced).

1 M). In contrast to our findings that the ionic process is much faster than bulk water, a slow process in the sub-GHz range appearing in experimental spectra is often interpreted as an ionic contribution[54, 55]. Within the limited accuracy of our data for $\phi_I(t)$, which is particularly prone to numerical errors (see Appendix B.1.3 for an in-depth discussion) and only allows us to sample fast relaxations, we can not say whether a slow ionic process exists or not. In our simulations the spectral contribution $\Delta\chi_I''(f)$ shows a red-shift as the anion size increases, which simply reflects that larger ions move more slowly through water. The real part $\Delta\chi_I'(f=0)$ amounts to a positive contribution to the total static dielectric constant of only about 1% for 1 M salt solutions, see the inset in Figure 2.7 B. Interestingly, the static dielectric contribution from ion positional fluctuations $\Delta\chi_I(f=0)$ scales roughly linearly with the salt concentration for NaCl, which indicates that it is due to uncorrelated and random ion positional fluctuations.

The frequency-dependent ionic conductivity $\sigma(f)$ is defined as the electric current response of free ionic charges to an external electric field and directly observable in simulations. According to equation 2.6, $\sigma(f)$ has two contributions, the first due to ion current self-correlations, $\sigma_I(f)$, and the second due to cross-correlations between the ion current and the water polarization, $\sigma_{IW}(f)$. Figures 2.8 A and B show our results for the frequency dependent real and imaginary parts of $\sigma(f)$ for all studied salt solutions, the results for NaCl are in good agreement with earlier studies[99]. There are obvious and trivial differences between the NaCl results for different salt concentrations, larger salt concentrations lead to higher conductivities at all frequencies, but no clear and systematic ion-specific trends can be discerned when comparing the spectra for different salts at equal concentration of 1 M. Only the static conductivity $\sigma_0 = \sigma(f=0) = \sigma_I(f=0)$ is directly observable in experiments, in fact, our simulation results for the molar conductance σ_0/c (black bars in Figure 2.8 C) are in fairly good agreement with experimental values[53, 54, 55] (blue bars in Figure 2.8 C) for all different salt types and salt concentrations. In Figure 2.8 C we also show the conductance $\sigma_0^k/(c\,n_I^k)$ for the different ion-pair configurations CIP, SIP, DSIP and FI, each properly normalized by the fraction of the different ion-pair configurations in solution n_I^k. We see, not surprisingly, that free ions FI exhibit the largest conductance, doubly solvent-separated (DSIP) and solvent-separated ion pairs (SIP) show a reduced conductance, and contact ion pairs (CIP) have a conductance that is typically reduced by more than a factor of two. Note that ion pairs contribute to the conductance by rotation and by small changes in the ion separation.

The experimental molar conductance of NaCl solutions decreases from infinite dilution to the saturating concentration by more than a factor of two[119]. Our decomposition into the conductances of different ion-pair contributions allows to shed new light on the concentration dependence of the total conductance of salt solutions. For this we write the total conductance $\sigma_0(c)/c$ as the sum of the conductances $\sigma_0^k/(c\, n_{\mathrm{I}}^k)$ of different ion-pair configurations according to

$$\frac{\sigma_0(c)}{c} = n_{\mathrm{I}}^{\mathrm{CIP}} \frac{\sigma_0^{\mathrm{CIP}}}{c\, n_{\mathrm{I}}^{\mathrm{CIP}}} + n_{\mathrm{I}}^{\mathrm{SIP}} \frac{\sigma_0^{\mathrm{SIP}}}{c\, n_{\mathrm{I}}^{\mathrm{SIP}}} + n_{\mathrm{I}}^{\mathrm{DSIP}} \frac{\sigma_0^{\mathrm{DSIP}}}{c\, n_{\mathrm{I}}^{\mathrm{DSIP}}} + n_{\mathrm{I}}^{\mathrm{FI}} \frac{\sigma_0^{\mathrm{FI}}}{c\, n_{\mathrm{I}}^{\mathrm{FI}}},$$

note that both σ_0^k and n_{I}^k are of course concentration dependent. For NaCl the simulated total molar conductance (black bars in Figure 2.8 C) decreases from $c = 0.5\,\mathrm{M}$ to $c = 2\,\mathrm{M}$ by $38\,\%$, in contrast, the molar conductance of individual ion-pair configurations shows a much weaker concentration dependence, the largest decrease of $\sigma_0^k/(c\, n_I^k)$ we observe for solvent-separated ion pairs (SIP) for which the molar conductance decreases by $26\,\%$ when going from $c = 0.5\,\mathrm{M}$ to $c = 2\,\mathrm{M}$. We conclude that a significant part of the molar conductance decrement as salt concentration increases comes from the growing weight $n_{\mathrm{I}}^{\mathrm{CIP}}$ of the weakly conducting contact-ion pairs and the reversely decreasing weight $n_{\mathrm{I}}^{\mathrm{FI}}$ of the highly conducting free ions, see Figure 2.1 E. Note that our reasoning breaks down at low concentrations, where long-ranged Coulombic interactions lead to a universal reduction of the conductance of free ions that scales as the square root of the salt concentration[120]. Rather, our findings explain the molar conductance reduction seen at larger concentrations above $100\,\mathrm{mM}$ in terms of the progressive replacement of highly conducting ion-pair configurations by weakly conducting ion-pair configurations.

2.7 Summary & Conclusions

From the good agreement between the experimental and simulated dielectric spectra we conclude that the halide force fields that were optimized based on thermodynamic properties[82] reproduce the ion specific dielectric effects quite well, this is in particular noteworthy for the dielectric relaxation time, which comes out naturally in good agreement with experimental data. The two force fields used for iodide, denoted by NaI(4) and NaI(1), were found to be of equal quality in our previous ion force-field optimization studies[82]. This degeneracy of the two iodide force fields could be lifted by the comparison of the simulated and experimental dielectric constants ϵ_{CC} and relaxation times τ_{CC} in the insets of Figures 2.3 B and D. This shows that dielectric properties can very well be used to optimize ionic force fields.

Due to improved simulation statistics and the correct treatment of the ion-water cross-correlation polarization term we show that this term is negative and considerably suppresses the total dielectric response. We also analyze the ion auto-correlation polarization contribution and show that it contributes only about one percent to the static dielectric constant. The decomposition of the dominant water polarization contribution into different solvation shells demonstrates that the first solvation shell shows the strongest ionic influence and is predominantly responsible for the blue shift and the dielectric decrement of the total dielectric spectra. By a further decomposition of the first water solvation shell into different ion-pair states we show that the static conductance of contact ion pairs is more than $50\,\%$ lower than for the other ion pairs, this partly explains the reduced conductance of concentrated salt solutions.

Our spectral decomposition suggests that the non-Debye-like character of salt solution spectra is not due to the superposition of different elementary relaxation processes with different relaxation times but rather an inherent spectral signature of the first solvation shell of water around ions. It would be interesting to investigate whether a different decomposition of the dielectric contribution from the first solvation shell into separate Debye processes is possible.

Although the experimental salt-concentration dependent and ion-specific trends of the dielectric constant and the dielectric relaxation time are well reproduced by our simulations, the absolute values are off, which we rationalize by a deficiency of the SPC/E water model we use. In the future, it would be crucial to redo the present simulations with a water model that reproduces the experimental dielectric properties of pure water, unfortunately the ion force fields would most likely have to be re-optimized for such a water model.

Chapter 3

Ion-Specific Solvation Water Dynamics: Single Water versus Collective Water Effects

Chapter 4

Dielectric Spectrum of Eight Residue Alanine: Impact of Peptide Secondary Structure and Hydration Shell Water

Bibliographic information: Parts of this chapter are under review for publication in the Journal of Chemical Physics (Ref. [i]).

4.1 Introduction

The dynamical interaction between protein and solvent at the protein-solvent interface is of major importance for protein function. Experimental spectral signals of protein solutions in electrolytes are often separated into dispersions of different time scales: Counter-ion diffusion can cause processes in the sub-kHz range (α-process)[143, 144], the faster β-process is caused rotational tumbling of the peptide[145, 146] or the polarization of membranes[143, 144, 147]. On the intermediate time scale between the β-process and the faster bulk water relaxation (γ-process) a weak δ-dispersion can appear, whose origin is unclear and is controversially discussed[62, 145, 146, 147]. Dielectric spectra of various proteins solvated in water have been measured protein concentration dependently[61, 62, 148, 149]. The behaviour and influence of the hydration shells on the dielectric signal can be estimated from those experiments, since the hydration shells overlap at higher concentrations.

In this chapter we are mostly interested in the effects of protein folding on the dielectric spectrum, but this is experimentally quite difficult, as we explain now: Bone[150] has measured the dielectric spectra of β-lactamase solvated in water-urea mixtures at three different urea concentrations to study the effect of the protein secondary structure in 1994. He found an increase of the static dielectric constant from 98 to 121 by increasing the urea concentration from 0 to 4 M and explained the growth by a higher number of absorbed water molecules in the unfolded state and a higher dipole moment of the denatured protein. Later the dielectric spectrum of bovine serum albumin (BSA) has also been measured for various urea concentrations of the solvent[151]. This study has taken into account that besides the protein unfolding due to higher urea concentrations the urea

itself also changes the dielectric spectrum. In this study the urea itself influences the dielectric spectra in the GHz range stronger than a conformational change of the protein. The red shift of the spectrum of pure aqueous urea solutions with increasing concentration has been observed in experiments[151] and MD simulations[152] and is explained by a change of the water structure near urea molecules. Due to the dominant effects of the denaturant urea, it is generally difficult the compare the dielectric signals of proteins in the native and unfolded states in these studies.

Another way to influence protein structures is a change in pH-value. THz-absorption measurements of protein solutions at different pH-concentrations have been used to obtain spectra of different structures[153]. But the charge density modification in the protein environment due to the pH-change might also affect the absorption. Moreover, the secondary structure can be changed by varying the temperature. In recent experiments a blue shift has been observed for aqueous solutions of lysozyme with increasing temperature[154]. The disadvantage of temperature dependent measurements is the temperature dependence of the water spectrum itself[52, 155], so that again the effects of protein unfolding on the spectrum are difficult to obtain.

In our MD simulations we can obtain the dielectric spectra of the model peptide eight residue alanine (Ala$_8$) for different secondary structures without changing the solvent, the solute concentration or the temperature. Instead, we use projections of equilibrium trajectories into different structural states. In an earlier MD simulation study the dielectric spectra of alanine and alanine dipeptide have been calculated already[156]. For these short peptides a split-up in folded and unfolded structures is not possible.

To the best of our knowledge secondary structure depending dielectric spectra have never been calculated out of equilibrium MD simulations. A similar projection of the protein dielectric spectra into folded and unfolded structures might be possible by coupling dielectric spectroscopy with a second method that allows to clearly distinguish folded from unfolded states with high time resolution[157, 158].

4.2 Methods

4.2.1 Dielectric Response Functions

The complex frequency-dependent dielectric susceptibility $\chi(f) = \chi'(f) - i\chi''(f)$ connects the total system polarization $\vec{P}(f)$ to the electric field $\vec{E}(f)$ via the linear-response relation $\vec{P}(f) = \chi(f)\epsilon_0\vec{E}(f)$, where ϵ_0 is the vacuum permittivity. According to the fluctuation dissipation theorem [106, 107] $\chi(f)$ follows from equilibrium polarization correlations via

$$\chi(f) = -\frac{1}{3Vk_BT\epsilon_0}\int_0^\infty e^{-2\pi ift}\langle\vec{P}(0)\cdot\dot{\vec{P}}(t)\rangle\mathrm{d}t, \qquad (4.1)$$

where $\dot{\vec{P}}(t) = \mathrm{d}\vec{P}(t)/\mathrm{d}t$ denotes the time derivative of the time-dependent total polarization $\vec{P}(t)$, V is the system volume and k_BT is the thermal energy. Via a partial integration equation 4.1 can be transformed into a form involving the polarization auto-correlation function $\phi(t) = \langle\vec{P}(0)\cdot$
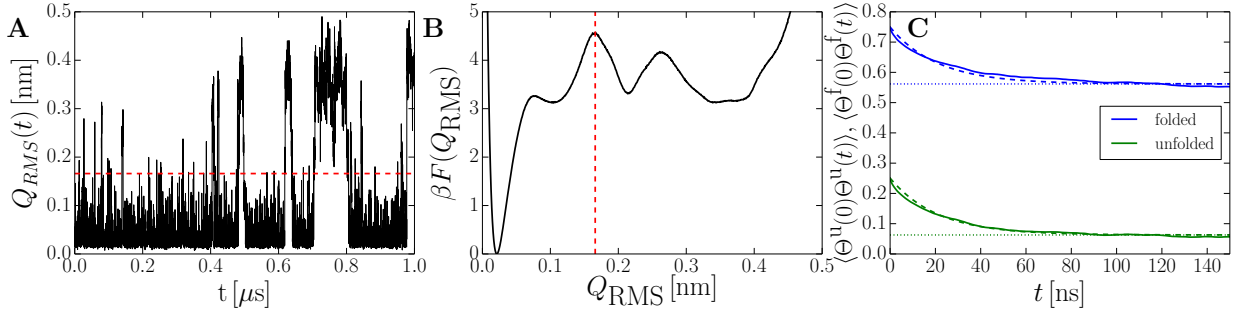
FIGURE 4.1: (A) A typical time evolution of the root mean squared deviation $Q_{RMS}(t)$ of the Ala_8 structure from the ideal α-helix. (B) The free energy landscape βF as a function of Q_{RMS}. The dashed red lines in (A) & (B) denote the threshold of $Q_{RMS} = 0.166\,\text{nm}$, which is used to distinguish between folded and unfolded structures. (C) The auto-correlation functions of the projection operators Θ^u (green) and Θ^f (blue). The dashed lines are exponential fits with a decay time $\tau = 20.9\,\text{ns}$ according to equations 4.5 & 4.7 and the dotted lines denote the long time limits.

$\vec{P}(t)\rangle/(3Vk_BT\epsilon_0)$, which can be obtained easily from simulations

$$\chi(f) = \frac{1}{3Vk_BT\epsilon_0}\left[\langle\vec{P}(0)\cdot\vec{P}(0)\rangle - i2\pi f\int_0^\infty e^{-2\pi ift}\langle\vec{P}(0)\cdot\vec{P}(t)\rangle\mathrm{d}t\right] \tag{4.2}$$

$$= \phi(0) - i2\pi f\int_0^\infty e^{-2\pi ift}\phi(t)\mathrm{d}t. \tag{4.3}$$

Since the end-capped Ala_8 is charge neutral, the whole system has no free charges and the polarization $\vec{P}$ is independent of the origin. In case of free charges, contributions from ionic currents must be included as demonstrated in chapter 2 on aqueous sodium-halide solutions. In the next subsections we introduce the decomposition formalisms for the polarization auto-correlation function $\phi(t)$ and the dielectric susceptibility $\chi(f)$ to study the contributions of different components and secondary structures.

4.2.2 Projection into Folded and Unfolded States

In order to define whether the peptide at time t is folded or not, we use the root mean squared deviation $Q_{RMS}(t)$ of the C_α-atoms of the alanine from the ideal α-helical configuration. A typical time evolution of $Q_{RMS}(t)$ is shown in Figure 4.1 A. The free energy landscape βF as a function of Q_{RMS} is shown in Figure 4.1 B. The projection operators $\Theta^f(t)$ and $\Theta^u(t) = 1 - \Theta^f(t)$ are defined to distinguish between folded and unfolded structures:

$$\Theta^f(t) = \begin{cases} 1, & \text{if } Q_{RMS}(t) < 0.166\,\text{nm} \\ 0, & \text{else} \end{cases} \tag{4.4}$$

The time-average of the projection operator of the folded structure $\langle\Theta^f(t)\rangle_t = p^f = 1 - p^u = 0.75$ is identical to the realization probability of the folded structure p^f. The auto-correlation functions of the projection operators are shown in Figure 4.1 C and can be well described by an exponential

decay down to their long time limits $\langle\Theta^{\mathrm{u}}(t)\rangle_t^2$ and $\langle\Theta^{\mathrm{f}}(t)\rangle_t^2$ according to the following equations:

$$c^{\mathrm{u}}(t) = \langle\Theta^{\mathrm{u}}(0)\Theta^{\mathrm{u}}(t)\rangle_t = e^{-t/\tau}(\langle\Theta^{\mathrm{u}}(t)\rangle_t - \langle\Theta^{\mathrm{u}}(t)\rangle_t^2) + \langle\Theta^{\mathrm{u}}(t)\rangle_t^2 \tag{4.5}$$

$$= p^{\mathrm{u}}\left(e^{-t/\tau}p^{\mathrm{f}} - p^{\mathrm{u}}\right) \tag{4.6}$$

$$c^{\mathrm{f}}(t) = \langle\Theta^{\mathrm{f}}(0)\Theta^{\mathrm{f}}(t)\rangle_t = e^{-t/\tau}(\langle\Theta^{\mathrm{f}}(t)\rangle_t - \langle\Theta^{\mathrm{f}}(t)\rangle_t^2) + \langle\Theta^{\mathrm{f}}(t)\rangle_t^2 \tag{4.7}$$

$$= p^{\mathrm{f}}\left(e^{-t/\tau}p^{\mathrm{u}} - p^{\mathrm{f}}\right), \tag{4.8}$$

where the equations fulfil the relation $\partial c^{\mathrm{u}}(t)/\partial t = \partial c^{\mathrm{f}}(t)/\partial t$ to obey detailed balance and where the time constant $\tau = 20.9\,\mathrm{ns}$ (fitted to the data in Figure 4.1 C) is a measure for the time between changes of the secondary structure. Since τ is much longer than the polarization relaxation times which are of the order of hundreds of picoseconds, the dynamics of the folding and unfolding processes do not affect our spectral results in the GHz range. MHz spectroscopy measurements might be able to see a mode caused by the dynamics of the conformational change.

Using the projection operator we can decompose the polarization and the spectral signal depending on the peptide secondary structure:

$$\phi^{\mathrm{f}}(t) = \langle\Theta^{\mathrm{f}}(0)\vec{P}(0)\cdot\vec{P}(t)\rangle/(3Vk_BT\epsilon_0 p^{\mathrm{f}}) \tag{4.9}$$

$$\phi^{\mathrm{u}}(t) = \langle\Theta^{\mathrm{u}}(0)\vec{P}(0)\cdot\vec{P}(t)\rangle/(3Vk_BT\epsilon_0 p^{\mathrm{u}}) \tag{4.10}$$

$$\phi(t) = p^{\mathrm{f}}\phi^{\mathrm{f}}(t) + p^{\mathrm{u}}\phi^{\mathrm{u}}(t) \tag{4.11}$$

$\phi^{\mathrm{f}}(t)$ is equal to the polarization auto-correlation function of a permanently folded system for times up to the order of $\tau \approx 20\,\mathrm{ns}$, where a conformational change becomes likely. The spectral signal $\chi^{\mathrm{f}}(f)$ is identical to the spectra of a permanently folded system, since unfolding processes of the time scale of tens of nanoseconds are not covered within our study ranging from $100\,\mathrm{MHz}$ to $1\,\mathrm{THz}$:

$$\chi^{\mathrm{f}}(f) = \phi^{\mathrm{f}}(0) - i2\pi f \int_0^\infty e^{-2\pi ift}\phi^{\mathrm{f}}(t)\mathrm{d}t \tag{4.12}$$

$$\chi^{\mathrm{u}}(f) = \phi^{\mathrm{u}}(0) - i2\pi f \int_0^\infty e^{-2\pi ift}\phi^{\mathrm{u}}(t)\mathrm{d}t \tag{4.13}$$

$$\chi(f) = p^{\mathrm{f}}\chi^{\mathrm{f}}(f) + p^{\mathrm{u}}\chi^{\mathrm{u}}(f) \tag{4.14}$$

4.2.3   Decomposition into Water and Peptide Contribution

In the absence of free charges the polarization $\vec{P}$ of a peptide solution consists of the water polarization $\vec{P}_{\mathrm{W}}$ and the peptide polarization $\vec{P}_{\mathrm{P}}$ according to $\vec{P} = \vec{P}_{\mathrm{W}} + \vec{P}_{\mathrm{P}}$. The water polarization $\vec{P}_{\mathrm{W}}$ can be split into the polarization of the hydration shell water $\vec{P}_{\mathrm{H}}$ and the remaining bulk-like water $\vec{P}_{\mathrm{B}} = \vec{P}_{\mathrm{W}} - \vec{P}_{\mathrm{H}}$. Water molecules, whose oxygen atom have a distance of less than $3\,\text{Å}$ from the nearest peptide atom, are denoted as hydration shell water. We use this relatively low threshold, in order to concentrate on the dominant effects in the first hydration shell. In the THz range hydration shell radii above one nanometer have been measured in experiments[159, 160]. Defining

the cross-correlation functions between the polarization components and the total polarization as

$$\phi_{\text{W}}(t) \quad = \quad \frac{\langle \vec{P}_{\text{W}}(0) \cdot \vec{P}(t) \rangle}{3V k_B T \epsilon_0} \tag{4.15}$$

$$\phi_{\text{H}}(t) \quad = \quad \frac{\langle \vec{P}_{\text{H}}(0) \cdot \vec{P}(t) \rangle}{3V k_B T \epsilon_0} \tag{4.16}$$

$$\phi_{\text{B}}(t) \quad = \quad \frac{\langle \vec{P}_{\text{B}}(0) \cdot \vec{P}(t) \rangle}{3V k_B T \epsilon_0} \tag{4.17}$$

$$\phi_{\text{P}}(t) \quad = \quad \frac{\langle \vec{P}_{\text{P}}(0) \cdot \vec{P}(t) \rangle}{3V k_B T \epsilon_0}, \tag{4.18}$$

we can express the spectral contribution of each system component as

$$\chi_{\text{W}}(f) \quad = \quad \phi_{\text{W}}(0) - i2\pi f \int_0^\infty e^{-2\pi i f t} \phi_{\text{W}}(t) \mathrm{d}t \tag{4.19}$$

$$\chi_{\text{H}}(f) \quad = \quad \phi_{\text{H}}(0) - i2\pi f \int_0^\infty e^{-2\pi i f t} \phi_{\text{H}}(t) \mathrm{d}t \tag{4.20}$$

$$\chi_{\text{B}}(f) \quad = \quad \phi_{\text{B}}(0) - i2\pi f \int_0^\infty e^{-2\pi i f t} \phi_{\text{B}}(t) \mathrm{d}t \tag{4.21}$$

$$\chi_{\text{P}}(f) \quad = \quad \phi_{\text{P}}(0) - i2\pi f \int_0^\infty e^{-2\pi i f t} \phi_{\text{P}}(t) \mathrm{d}t. \tag{4.22}$$

The total polarization auto-correlation function $\phi(t)$ as well as the total susceptibility $\chi(f)$ can be expressed as sums over different contributions

$$\phi(t) \quad = \quad \phi_{\text{W}}(t) + \phi_{\text{P}}(t) \tag{4.23}$$

$$= \quad \phi_{\text{H}}(t) + \phi_{\text{B}}(t) + \phi_{\text{P}}(t) \tag{4.24}$$

$$\chi(f) \quad = \quad \chi_{\text{W}}(f) + \chi_{\text{P}}(f) \tag{4.25}$$

$$= \quad \chi_{\text{H}}(f) + \chi_{\text{B}}(f) + \chi_{\text{P}}(f). \tag{4.26}$$

In addition, we define the cross-correlation between the polarization of components k and l as

$$\phi_{k\,l}(t) \quad = \quad \frac{\langle \vec{P}_k(0) \cdot \vec{P}_l(t) \rangle}{3V k_B T \epsilon_0}, \tag{4.27}$$

where k and l can represent protein P, water W, hydration shell water H or bulk water B. So for instance, the polarization cross-correlation between hydration shell water (H) at time zero and bulk-like water (B) at time t is

$$\phi_{\text{HB}}(t) \quad = \quad \frac{\langle \vec{P}_{\text{H}}(0) \cdot \vec{P}_{\text{B}}(t) \rangle}{3V k_B T \epsilon_0}, \tag{4.28}$$

where the respective spectral contributions are given analogously to equations 4.19–4.22 and the total spectra consists of three, four or six terms depending on the level of decomposition

$$\chi(f) \;=\; \chi_{\text{WW}}(f) + \chi_{\text{PP}}(f) + 2\chi_{\text{WP}}(f) \tag{4.29}$$

$$\;=\; \chi_{\text{HW}}(f) + \chi_{\text{BW}}(f) + \chi_{\text{PP}}(f) + 2\chi_{\text{WP}}(f) \tag{4.30}$$

$$\;=\; \chi_{\text{HH}}(f) + \chi_{\text{BB}}(f) + \chi_{\text{PP}}(f) + 2\chi_{\text{HB}}(f) + 2\chi_{\text{HP}}(f) + 2\chi_{\text{BP}}(f). \tag{4.31}$$

The water terms WW, HW and BW can be further decomposed into self and collective correlations. We only write down the definition for the hydration shell water here. For bulk water and the total water contributions the definitions are analogous:

$$\phi_{\text{HW,self}}(t) \;=\; \frac{1}{3Vk_BT\epsilon_0} \sum_{i\in\{N_H\}} \langle \vec{p}_i(0) \cdot \vec{p}_i(t) \rangle \tag{4.32}$$

$$\phi_{\text{HW,coll}}(t) \;=\; \frac{1}{3Vk_BT\epsilon_0} \sum_{i\in\{N_H\}} \sum_{j\neq i}^{N} \langle \vec{p}_i(0) \cdot \vec{p}_j(t) \rangle, \tag{4.33}$$

where $\{N_H\}$ is the ensemble of hydration shell water and $N = 688$ is the total number of water molecules. By construction, the sum over the self and collective terms returns the cross-correlation function between the polarization of hydration shell water and all water,

$$\phi_{\text{HW}}(t) = \phi_{\text{HW,self}}(t) + \phi_{\text{HW,coll}}(t). \tag{4.34}$$

The decomposed spectral contributions follow as

$$\chi_{\text{HW,self}}(f) \;=\; \phi_{\text{HW,self}}(0) - i2\pi f \int_0^\infty e^{-2\pi i f t} \phi_{\text{HW,self}}(t)\mathrm{d}t \tag{4.35}$$

$$\chi_{\text{HW,coll}}(f) \;=\; \phi_{\text{HW,coll}}(0) - i2\pi f \int_0^\infty e^{-2\pi i f t} \phi_{\text{HW,coll}}(t)\mathrm{d}t. \tag{4.36}$$

All component dependent decompositions can be combined with a projection into folded or unfolded states analogously to equations 4.9–4.14 to generate polarization terms as $\phi_{kl}^{\text{f}}(t)$ and $\phi_{kl}^{\text{u}}(t)$ and the corresponding spectral terms $\chi_{kl}^{\text{f}}(f)$ and $\chi_{kl}^{\text{u}}(f)$.

4.2.4 Simulations Methods

We use GROMACS 4.5.4[71] to simulate seven starting configurations of end-capped eight residue alanine (Ala$_8$) solvated in 688 SPC/E water molecules in the NPT ensemble at 300 K and atmospheric pressure for 1 μs each run. The amber03 force field[83], the GROMACS v-rescale thermostat[161], a Parrinello-Rahman barostat[162] and a 2 fs integration time step are used. The neighbor list is updated every 20 fs and the trajectories are collected every 100 fs. The electrostatics are computed by Particle Mesh Ewald and the Lennard-Jones interaction are cut off at 0.9 nm. Because of memory limitations all trajectories are split in segments of 200 ns length for data analysis. The polarization components of each segment are Fourier transformed via Fast Fourier Transformation (FFT) and correlations are calculated by multiplication in Fourier space.

After back transformation into the time domain the correlation functions are averaged over all segments. A time cutoff is used during calculation of the spectra via Laplace transformation of the correlation functions, so that the correlation functions are only integrated up to the time, where they first drop below zero. For the calculation of the polarization correlation functions we update the decomposition of water into different solvation shells every 100 fs according to the current configuration, consequently, the water partitioning changes in time. For the calculation of the self polarization correlations the trajectories are split in segments of 1 ns length. The dipolar auto-correlation function of each water molecule is calculated and then clustered into the different solvation shells depending on the water configuration at the beginning of each trajectory segment. 1 ns is sufficiently long to obtain correlations in the relevant time range, since the single dipole auto-correlation function drops below zero within 300 ps in our simulations. The collective correlations become negative within 3 ns and are obtained by subtracting the self correlation from the total water polarization correlations. The peptide polarization auto-correlation function ϕ_{PP} becomes negative at about 6 ns.

4.3 Spectral Decomposition

4.3.1 Spectral Fits wih Cole-Cole and Double Debye Functions

For a quantitative analysis we fit a Cole-Cole function according to

$$\chi(f) \quad = \quad \frac{\epsilon}{1 + (i\,2\pi f\tau)^{1-\alpha}} + \chi_{\infty}, \qquad (4.37)$$

to the different spectral components with the fit parameters ϵ, τ, α and χ_{∞}. We do not set $\chi_{\infty} = 0$, since for some components the real part of the high frequency susceptibilities is not equal to zero, due to integration errors caused by the finite time resolution of our data of 100 fs. In the analysis of our simulation data we fit the real and imaginary parts of the dielectric spectrum simultaneously with the error functional $(\Delta\chi')^2 + (2\Delta\chi'')^2$ using a logarithmic distribution of sample frequencies in the range between 0.1 and 100 GHz. We restrict the fitting range up to 100 GHz, since the high frequencies might be affected by integration errors due to the data collecting time of 100 fs. In order to roughly achieve the same relative errors for real and imaginary parts, we use a higher weight for the imaginary part, since it has a lower absolute value. The results for the fit parameters are listed for all states in Table 4.1 and are discussed in the following sections focusing on the different contributions.

As will be discussed later, some spectral components in particular total χ, χ_{HH}, χ_{HB}, χ_{HW} and $\chi_{HW,coll}$ can not be well described by Cole-Cole fits and we perform double Debye fits according to

$$\chi(f) \quad = \quad \frac{\epsilon_1}{1 + i\,2\pi f\tau_1} + \frac{\epsilon_2}{1 + i\,2\pi f\tau_2} + \chi_{\infty}, \qquad (4.38)$$

to improve the fitting quality. The results are listed in Table 4.2 and we will refer to them in the upcoming sections. The spectral contribution χ_{HH} can not be well reproduced by a double Debye fit (not shown). So, we perform a triple Debye fit according to

$$\chi(f) \quad = \quad \frac{\epsilon_1}{1 + i\,2\pi f\tau_1} + \frac{\epsilon_2}{1 + i\,2\pi f\tau_2} + \frac{\epsilon_3}{1 + i\,2\pi f\tau_3} + \chi_{\infty}, \qquad (4.39)$$

	ϵ	ϵ^{f}	ϵ^{u}	τ [ps]	τ^{f} [ps]	τ^{u} [ps]	α	α^{f}	α^{u}	χ_∞
total χ	72.63	74.36	67.80	12.04	12.12	11.82	0.122	0.145	0.047	-1.42
χ_{P}	5.83	7.00	2.43	715.37	730.82	538.08	0.037	0.024	0.187	0.07
χ_{W}	66.85	67.25	65.40	11.72	11.71	11.75	0.041	0.047	0.021	1.01
χ_{B}	62.38	62.55	61.16	11.51	11.53	11.56	0.030	0.030	0.018	1.24
χ_{H}	4.76	4.90	4.49	17.12	18.16	15.20	0.261	0.315	0.105	-0.35
χ_{PP}	3.85	4.70	1.35	719.14	734.18	550.03	0.025	0.014	0.161	0.07
χ_{WP}	1.96	2.21	1.09	702.63	699.08	543.34	0.051	0.018	0.224	0.01
χ_{BP}	1.23	1.40	0.72	674.26	684.39	531.32	0.040	0.014	0.220	0.00
χ_{HP}	0.70	0.82	0.36	723.88	739.21	576.78	0.039	0.020	0.232	0.01
χ_{WW}	65.11	65.17	64.95	11.64	11.62	11.71	0.018	0.019	0.016	1.71
$\chi_{\mathrm{WW,self}}$	16.12	15.39	18.30	5.13	5.13	5.13	0.048	0.048	0.048	1.86
$\chi_{\mathrm{WW,coll}}$	50.85	51.91	47.69	14.19	14.10	14.35	-0.012	-0.001	-0.042	-1.35
χ_{BW}	62.92	63.37	61.27	11.56	11.55	11.58	0.037	0.042	0.019	1.04
$\chi_{\mathrm{BW,self}}$	15.31	14.61	17.37	5.12	5.13	5.12	0.048	0.048	0.048	1.77
$\chi_{\mathrm{BW,coll}}$	47.79	48.88	44.42	13.95	13.85	14.14	-0.015	-0.005	-0.045	-1.24
χ_{HW}	3.89	3.80	4.13	15.21	15.46	14.66	0.081	0.091	0.042	-0.00
$\chi_{\mathrm{HW,self}}$	0.82	0.78	0.94	5.25	5.24	5.25	0.054	0.054	0.054	0.09
$\chi_{\mathrm{HW,coll}}$	3.08	3.03	3.22	18.63	18.97	17.61	0.024	0.036	-0.019	-0.13
χ_{HB}	2.58	2.53	2.73	17.47	17.70	16.71	0.007	0.015	-0.022	-0.40
χ_{BB}	58.77	58.96	58.29	11.25	11.24	11.29	0.014	0.014	0.017	2.03
χ_{HH}	1.36	1.32	1.45	9.16	9.19	9.17	0.214	0.236	0.154	0.33

TABLE 4.1: Cole-Cole fit parameters for the total spectrum and the decomposed simulation spectra: All components involving the peptide (P) are very slow. They are even slower and have a higher amplitude if the peptide is folded. H denotes hydration water, while B denotes the remaining bulk-like water. The total water ensemble is labelled by W. Collective water relaxations (coll) and the cross-correlation HB have slower relaxation times than the self relaxations. The stretching parameter α of the hydration water terms χ_{H} and χ_{HH} is quite large reflecting a multiple Debye structure of the spectra.

in this case. The fit parameters are listed in Table 4.3.

4.3.2 Peptide Contribution

In Figure 4.2 we present the real (A) and imaginary part (D) of the total dielectric spectra for the complete trajectory (black line), folded structure (blue line) and unfolded structure (green line). A second absorption peak in the sub-GHz range appears in addition to the well-known bulk water resonance (red line), especially the peptide is folded. Therefore, only a double Debye fit to the folded state (dotted lines) with relaxation times of 11.6 ps and roughly 600 ps reproduces the signal well. A Cole-Cole fit is not sufficient as can be seen in Figure 4.3. The low frequency absorption is mainly caused by the peptide $\chi_{\mathrm{P}}(f)$ (B & E) and is much stronger if the peptide is folded. The relative influence of the secondary structure on the water absorption $\chi_{\mathrm{W}}(f)$ is weak (C & F). The absolute changes in the water spectrum are discussed later in a further decomposition. But first we want to focus on the absorption signal from the peptide.

In Figure 4.4 A we show a two-dimensional plot of the logarithm of the probability density ρ as function of the root mean squared deviation of the Ala$_8$ structure from the ideal α-helix Q_{RMS} and the static dielectric susceptibility of the peptide $\chi'_{\mathrm{PP}}(f = 0) = |\vec{P}_{\mathrm{P}}^2|/(3V k_B T \epsilon_0)$: The highest

	χ	χ_{HH}	χ_{HB}	χ_{HW}	$\chi_{HW,coll}$
ϵ_1	8.61	0.17	0.21	0.37	0.33
ϵ_1^f	10.27	0.18	0.24	0.41	0.38
ϵ_1^u	3.74	0.71	0.13	0.26	0.20
ϵ_2	63.84	1.06	2.53	3.55	2.96
ϵ_2^f	63.75	1.02	2.46	3.42	2.87
ϵ_2^u	63.73	0.66	2.76	3.89	3.24
τ_1 [ps]	604.65	195.94	1047.21	548.63	1041.31
τ_1^f [ps]	634.62	286.77	1029.34	592.95	1038.51
τ_1^u [ps]	332.67	17.88	1043.47	339.24	1132.76
τ_2 [ps]	11.61	8.77	16.97	14.55	17.81
τ_2^f [ps]	11.57	9.01	17.05	14.64	17.94
τ_2^u [ps]	11.60	4.72	16.65	14.23	17.48
χ_∞	2.32	0.47	-0.41	0.12	-0.12

TABLE 4.2: Double Debye fit parameters for the total spectrum and some of the decomposed spectra: They consist of one fast bulk water-like process and another much slower process. HH denotes auto-correlation of the hydration shell water, HB denotes the cross-term between hydration water and bulk-like water, HW denotes the hydration water contribution and HW,coll its collective part.

	ϵ_1	ϵ_2	ϵ_3	τ_1 [ps]	τ_2 [ps]	τ_3 [ps]	χ_∞
χ_{HH}	0.14	0.83	0.35	577.77	13.23	2.94	0.40
χ_{HH}^f	0.15	0.80	0.33	625.18	13.36	2.94	0.39
χ_{HH}^u	0.10	0.96	0.38	360.03	12.47	2.87	0.43

TABLE 4.3: Triple Debye fit parameters for spectral contribution χ_{HH} of the polarization auto-correlation of the hydration shell water.

probability occurs for folded states in connection with a high peptide polarization. A side maximum appears for unfolded states and a weak polarization of the peptide. A snapshot of the folded structure in Figure 4.4 B illustrates the high polarization of the folded peptide, since the negatively charged oxygen atoms (red) point down, while the positively charged nitrate groups (nitrogen is colored in blue) point upwards. Since the strong polarization is caused by the backbone and not the side chains, α-helical peptides with other amino acid sequences likely show similar effects. The snapshot of an unfolded peptide shows no significant polarization (Figure 4.4 C).

Boresch et al.[156] have decomposed the alanine and alanine dipeptide spectral contribution χ_P into a term of the peptide polarization auto-correlation χ_{PP} and the cross-terms with the hydration χ_{HP} and the bulk water χ_{BP} and have shown that the contributions have almost identical relaxation times. The time scale increases with peptide length from alanine to alanine dipetide. Although our peptide is much larger than in their study, we find in line with those results that the Cole-Cole relaxation time $\tau \approx 700$ ps is nearly the same for all three components χ_{PP}, χ_{HP} and χ_{BP} (Table 4.1). An even slower polarization relaxation time of about 2.5 ns is reported for the large 76 amino acid Ubiquitin[163], which confirms the intuitive trend that larger peptides relax slower. In our study the peptide polarization relaxation time matches with the rotational tumbling time of the peptide: The auto-correlation of the end-to-end vector $\vec{R}_{ee}(t)$ between the C_α atom of the first and last alanine monomer decays exponentially with a decay time of $\tau_R = 832$ ps (Figure 4.4 D, black line). The end-to-end unit vector $\vec{R}_{ee}(t)/|\vec{R}_{ee}(t)|$ (blue line, $\tau_r = 779$ ps) and the difference from the average distance $|\vec{R}_{ee}(t)| - \langle|\vec{R}_{ee}|\rangle$ (green line, $\tau_{|R|} = 813$ ps) have nearly the same decay
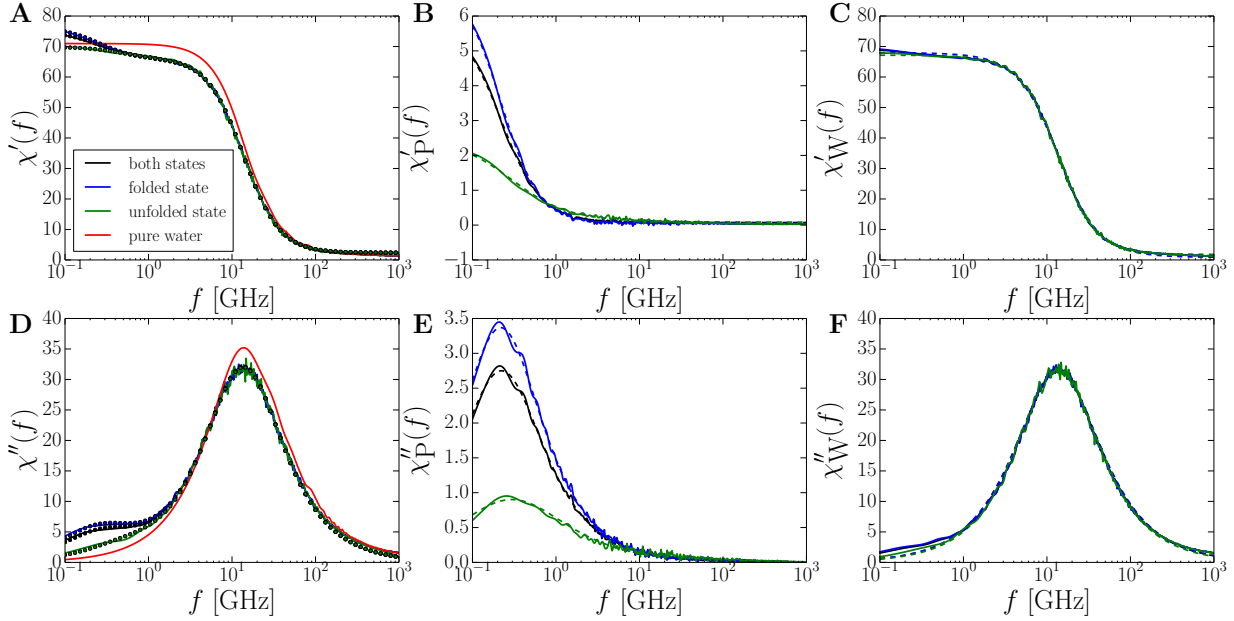
FIGURE 4.2: The real (A) and imaginary part (D) of the dielectric susceptibility $\chi(f)$ for folded (blue), unfolded state (green) and both states (black line). The pure water spectrum is plotted for comparison (red line): The low frequency response is a bit stronger for the folded structure. The real (B) and imaginary part (E) of the dielectric susceptibility of the peptide $\chi_P(f)$ is much stronger of the folded peptide. The water contribution $\chi_W(f)$ (C & F) has a relatively weak dependence on the secondary structure. The solid lines are our data, while the dashed lines are Cole-Cole fits. In (A) & (D) double Debye fits are shown as dotted lines instead of the Cole-Cole fits. Note that $\chi(f) = \chi_W(f) + \chi_P(f)$.

times. We compare the rotational tumbling time of the peptide measured in the simulation with the hydrodynamical rotational diffusion time of a cylinder of length L and radius R: The rotational diffusion constant D_{rot} in first order of R/L is[164]

$$D_{rot} \quad = \quad \frac{3k_BT}{\pi L^3 \eta} \left(\ln(L/R) - 1.57 + 7(1/(\ln(L/R)) - 0.28)^2 \right). \quad (4.40)$$

We use the dynamic viscosity of water $\eta = 8.54 \cdot 10^{-4} \, \mathrm{N/(m\,s)}$ and the relation $\tau_{rot} = 1/(2D_{rot})$. The radius of the ideal α-helix formed by the backbone carbon atoms is $R = 0.23 \, \mathrm{nm}$ and the length is $L = 1.2 \, \mathrm{nm}$ (0.15 nm per monomer). Using these values we obtain $\tau_{rot} = 227 \, \mathrm{ps}$, which is a factor 3.5 lower than found in the simulation. If the presence of side-chains and end-caps is modelled by increasing the dimensions to $L = 1.5 \, \mathrm{nm}$ and $R = 0.33 \, \mathrm{nm}$ (note that increasing R decreases τ_{rot}) the prediction of equation 4.40 is 381 ps. A further increase of the cylinder length to $L = 1.8 \, \mathrm{nm}$ would reproduce the simulation results.

The similar shape of the three contributions χ_{PP}, χ_{HP} and χ_{BP} is presented in Figure 4.5. The peptide auto-correlation term dominates the amplitude of the sum of the cross-terms by a factor of two. Further, the cross-term between bulk water and peptide exceeds the term between hydration water and peptide by a factor two. But increasing the hydration shell radius from 3 Å to 6 Å only enhances the amplitude of the hydration-peptide cross-absorption $\chi'_{HP}(f = 0, R_H)$ by less than 20 % from 0.69 to 0.82 for the full trajectory (Table 4.4). This weak correlation between the peptide and the second hydration shell, justifies the choice of the relatively small hydration shell radius of 3 Å. About 30 % of the cross-amplitude $\chi'_{WP}(f = 0)$ is caused by water molecules in more than 1 nm distance to the peptide (comparison of the last two rows of Table 4.4), showing the long
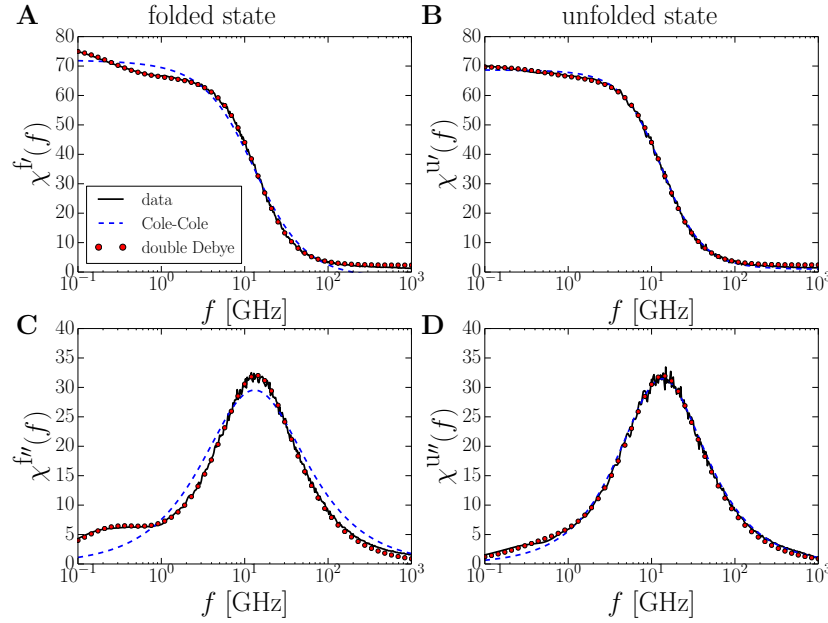
FIGURE 4.3: Comparison of Cole-Cole (blue dashed lines) and double Debye fits (red dots) to the overall spectrum $\chi(f)$ (black solid lines) for the folded (A & C) and the unfolded state (B & D): Especially for the folded state the Cole-Cole fit is not adequate.
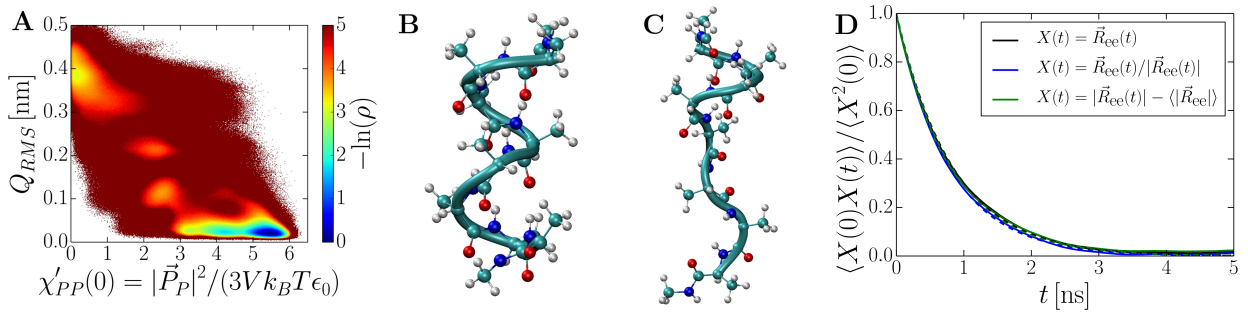

FIGURE 4.4: (A) The two-dimensional landscape of the logarithm of the probability density ρ as function of the root mean squared deviation Q_{RMS} of the Ala_8 structure from the ideal α-helix and the static dielectric susceptibility of the peptide $\chi'_{PP}(0) = |\vec{P}_P^2|/(3Vk_BT\epsilon_0)$.
(B) Snapshot of the α-helical peptide structure: The negatively charged oxygen (red) points down, while the positively charged nitrate group (nitrogen is colored in blue) points upwards. As a consequence, this configuration has a high dipole moment pointing upwards. (C) Snapshot of an unfolded structure. (D) Auto-correlation function of the end-to-end vector $\vec{R}_{ee}$ (black), the end-to-end unit vector $\vec{R}_{ee}/|\vec{R}_{ee}|$ (blue) and the difference from the average distance $|\vec{R}_{ee}(t)| - \langle|\vec{R}_{ee}|\rangle$ (green). All three correlation functions decay exponentially with decay times of about 800 ps (dashed lines).

range of the dipole-dipole correlations and collective effects. These effects might be the origin of the extended hydration shells observed in experiments[159, 160]. The spectral shape of $\chi_{HP}(f, R_H)$ is shown for various radii R_H in Figure 4.6. The peptide secondary structure leads to a blue shift for all three contributions shown in Figure 4.5 from the folded (blue lines) to the unfolded state (green lines). The relaxation times of the Cole-Cole fits decrease by about 35 % for an unfolded peptide (540 ps) compared to a folded peptide (730 ps, Table 4.1).
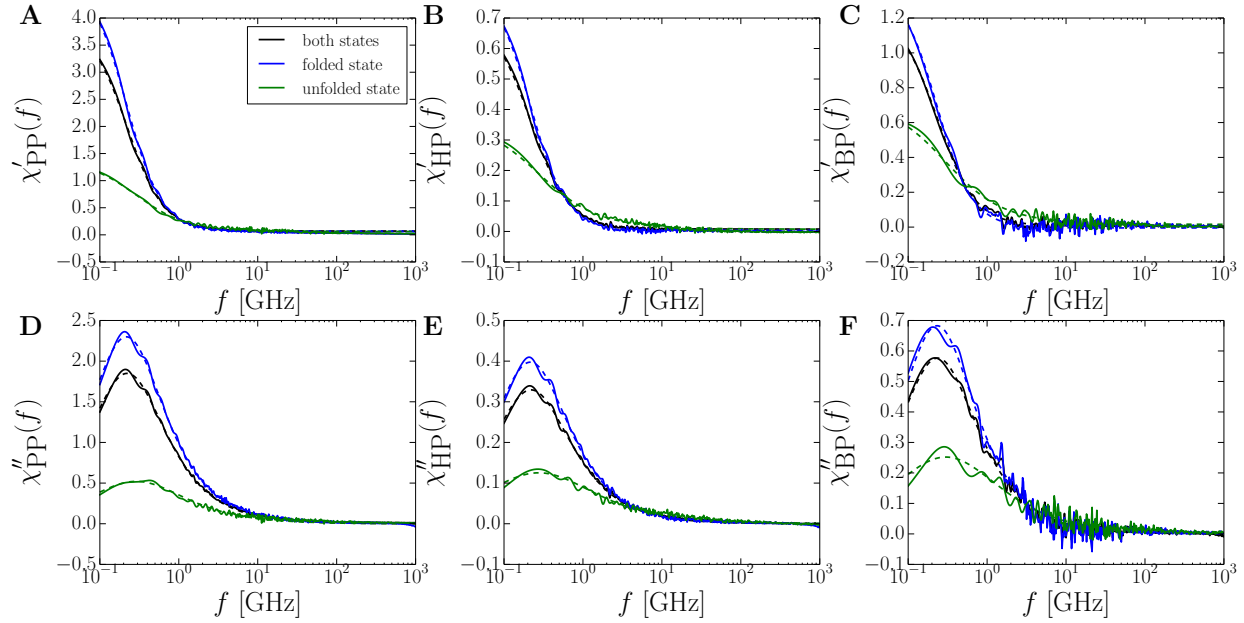
FIGURE 4.5: The real (A) and imaginary part (D) of the dielectric susceptibility $\chi_{PP}(f)$ due to the peptide polarization auto-correlation for folded (blue), unfolded state (green) and the complete trajectory (black line): The dominant response appears in the sub-GHz range and is much stronger if the peptide is folded. The signals due to the cross-correlation between hydration-water and peptide $\chi_{HP}(f)$ (B & E) and between bulk water and peptide $\chi_{BP}(f)$ (C & F) have a similar shape.

R_H [Å]	$\chi'_{HP}(f = 0, R_H)$	$\langle N_H(R_H) \rangle$	$n_H(R_H)$
3	0.69	34.7	0.051
4	0.64	82.9	0.121
5	0.70	119.1	0.173
6	0.82	172.3	0.250
7	0.91	232.8	0.338
8	1.04	296.9	0.432
9	1.17	364.4	0.530
10	1.31	434.5	0.632
∞	1.91	688.0	1.000

TABLE 4.4: Effect of the hydration shell radius R_H on the static contribution of the cross-correlation between hydration water and peptide polarization $\chi'_{HP}(f = 0, R_H)$, the average number of hydration shell water molecules $\langle N_H(R_H) \rangle$ and the hydration water fraction $n_H(R_H) = \langle N_H(R_H) \rangle / N$: More than one third of the cross-term amplitude is caused by a 3 Å shell. On the other hand 30 % of the amplitude is raised by water molecules, which are in more than 1 nm distance to the peptide. Note that with the exception of Figure 4.6 all spectra shown in this work are obtained using $R_H = 3$ Å.

4.3.3   Water Contribution

In the previous section we have focused on the effect of the secondary structure on spectral contributions involving the peptide polarization including cross-terms with the water-polarization. In addition to these terms it is conceivable that the peptide structure also influences polarization correlations between water molecules. Therefore, we decompose the contribution of the water auto-correlation χ_{WW} into contributions of the auto-correlations of the hydration shell polarization χ_{HH} and bulk water χ_{BB} and the cross-contribution χ_{HB} analogously to Boresch et al.[156]
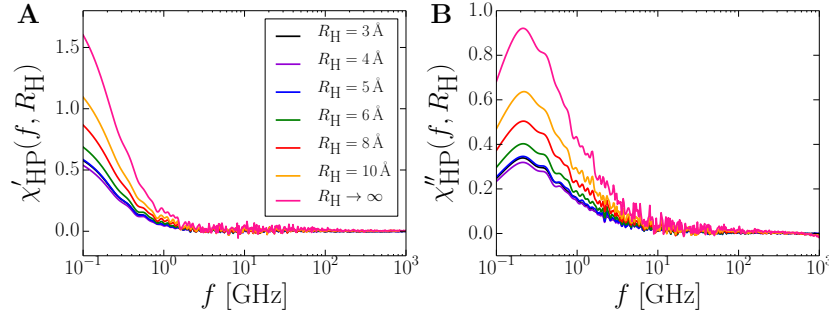
FIGURE 4.6: Comparison of the real (A) and imaginary part (B) of the cross-contribution $\chi_{HP}(R_H)$ between hydration water and peptide for various hydration shell radii R_H. Note that the black line ($R = 3\,\text{Å}$) and the blue line ($R = 5\,\text{Å}$) are almost identical and that $\chi_{HP}(R_H \to \infty) = \chi_{WP}$.
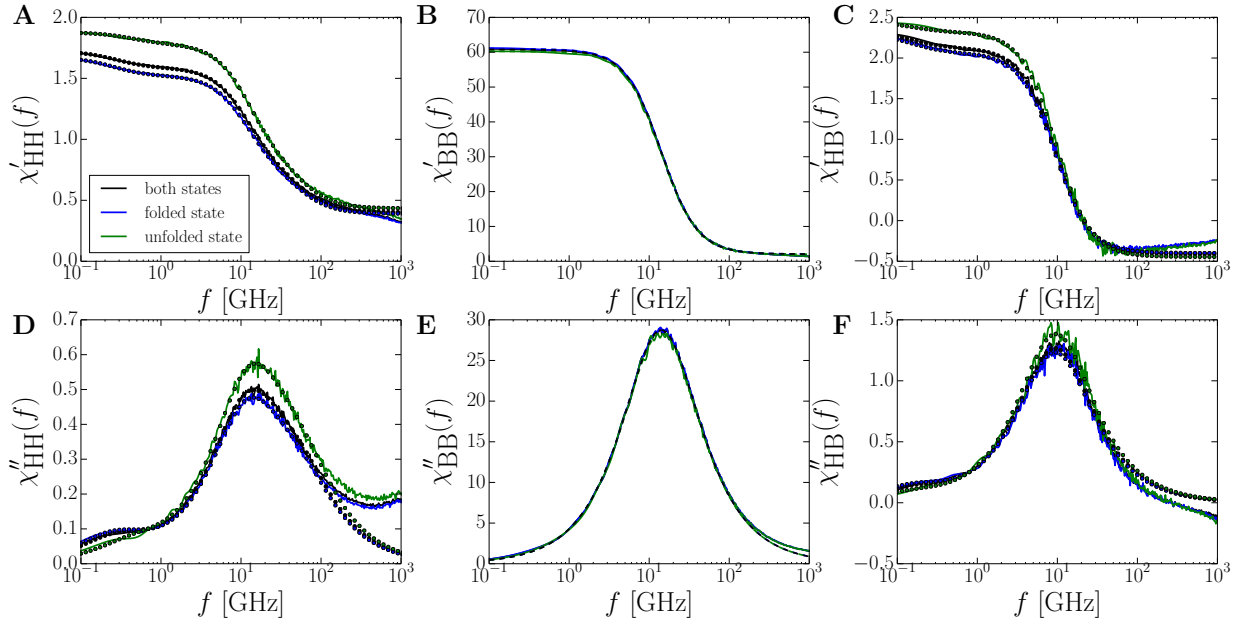

FIGURE 4.7: The real (A) and imaginary part (D) of the dielectric susceptibility due to the hydration-water auto-correlation $\chi_{HH}(f)$ for folded (blue), unfolded state (green) and both states (black line). The dielectric susceptibility due to the bulk-water auto-correlation $\chi_{BB}(f)$ (B & E) does not depend on the peptide structure. The signal due to the cross-correlation between hydration-water and bulk water $\chi_{HB}(f)$ (C & F) is slightly larger for an unfolded peptide. The relaxation of the cross-correlation is slower than the relaxations of the auto-correlations HH and BB. Triple Debye fits are shown for χ_{HH} as dotted lines, while Cole-Cole fits (dashed lines) are already almost indistinguishable from the data for χ_{BB}. Double Debye fits are shown for χ_{HB} as dotted lines.

and extend their decomposition with the projection into folded and unfolded states in Figure 4.7. An impact of the peptide structure on the bulk water dielectric response χ_{BB} (Figures 4.7 B & E) is not observable. The number of fraction of hydration shell water n_H (relative to the total number of water in the system) is $5.68\,\%$, if the peptide is unfolded. In case of a folded peptide n_H decreases to $4.84\,\%$ (the ensemble average is $5.05\,\%$). As a consequence, the amplitude of the hydration water absorption peak (Figures 4.7 A & D) is increased if the peptide is unfolded. In the sub-GHz range the absorptions χ_{HH} and χ_{HB} are increased in case of a folded peptide.

For very high frequencies the absorption $\chi''_{HH}(f)$ seems to have an extremely fast peak and while the absorption $\chi''_{HB}(f)$ is significantly negative in this range. Since the two contributions almost

cancel out each other, they might be an artifact of the decomposition into hydration and bulk water. Molecules, whose distance to the nearest peptide atom to very close to the hydration shell radius $R_H = 3\,\text{Å}$, might leave and reenter the hydration shell with a very high frequency and cause the observed signal.
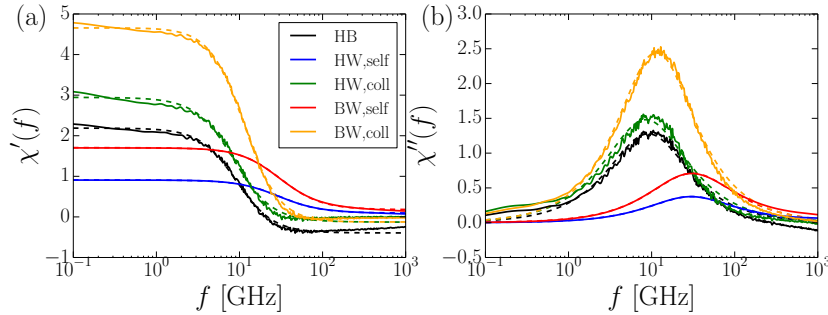

FIGURE 4.8: Comparison of different components of the real (A) and imaginary part (B) of the water susceptibilities: The signals due to the cross-correlation between the hydration water and bulk-like water HB (black line) and the collective signal of the hydration water HW,coll (green line) and collective relaxations of bulk water BW,coll (orange line) occur on the same time scale. The self relaxation of individual water molecules of the hydration shell (blue line) and in bulk (red line) are much faster than the collective relaxations. The dashed lines are Cole-Cole fits and the bulk signals (orange and red) have been decreased by one order of magnitude for better visibility.

In line with earlier research on alanine and alanine dipeptide[156] as well as on NAGMA and NALMA[129] we find that the the cross-term HB is slower ($\tau \approx 17.5\,\text{ps}$) than the terms HH and BB (τ approximately 9 and 11 ps, Table 4.1). In order to come up with an explanation for the slower cross-term HB we refer to the self relaxation of single molecules and the collective relaxation between different water molecules. It is known that the self relaxation of water is faster than the collective relaxation in pure water and ionic solutions[121, 122, 123, 124, 125]. Unless the water molecules do not frequently leave or enter the hydration shell within the relaxation time τ, the cross-term HB only consists of collective relaxations ($\chi_{HB}(f) \approx \chi_{HB,coll}(f)$). The water terms HW and BW are decomposed into self and collective terms as defined in equations 4.32 & 4.33 analogously to our work on ionic solutions in chapter 3. A direct comparison of the five terms is shown in Figure 4.8, where the dominant BW terms are rescaled by a factor 0.1 for better visibility. In Figure 4.8 B we show that the three collective parts HB (black), HW (green) and BW (orange) occur on the same time scales, while the two self relaxation contributions of HW (blue) and BW (red) are significantly faster. The fit parameters listed in Table 4.1 support the impression received from the graphic. The HB relaxation of 17.5 ps is in the small range between by the faster bulk BW collective relaxation of 14.0 ps and the slower collective hydration water HW relaxation time of 18.6 ps. So, the relatively slow dielectric signal of cross-term χ_{HH} (17.5 ps) compared to the hydration water χ_{HH} (9.2 ps) and bulk-like water χ_{BB} (11.3 ps) is due to the slower collective relaxation of water in general and not related to the presence of the peptide. Since the cross-contribution HB ($\tau = 17.5\,\text{ps}$, Table 4.1) is only 25% slower than the collective relaxations in bulk water (BW,coll: $\tau = 14.0\,\text{ps}$), we do not think that this term is the intermediate time-scale δ-process seen in experiments. Although three Debye processes are necessary to describe the spectral shape of χ_{HH} in Figures 4.7 A & D, one has to be cautious by identifying the δ-process: In the decomposition $\chi_{WW} = \chi_{HH} + 2\chi_{HB} + \chi_{BB}$ the auto-correlation term χ_{HH} contains disproportionately more self-relaxations in comparison with χ_{WW}, since the self-relaxation is almost absent in χ_{HB} and transfered to χ_{HH}. So the fast peak (2.9 ps in Table 4.4) in χ_{HH} might be the large amount of self-relaxation and the intermediate peak

(13.2 ps) the fast collective contributions similar to pure water. Note that a decomposition of the single Debye-like pure water signal with $\tau = 10.7$ ps into self and collective processes leads to two processes of Cole-Cole relaxation times 4.3 and 13.0 ps, as shown in chapter 3. The slowest process of the triple Debye fit with $\tau = 578$ ps should be too close to the peptide polarization relaxation time of about 700 ps to be identified as a separate peak in experiments.
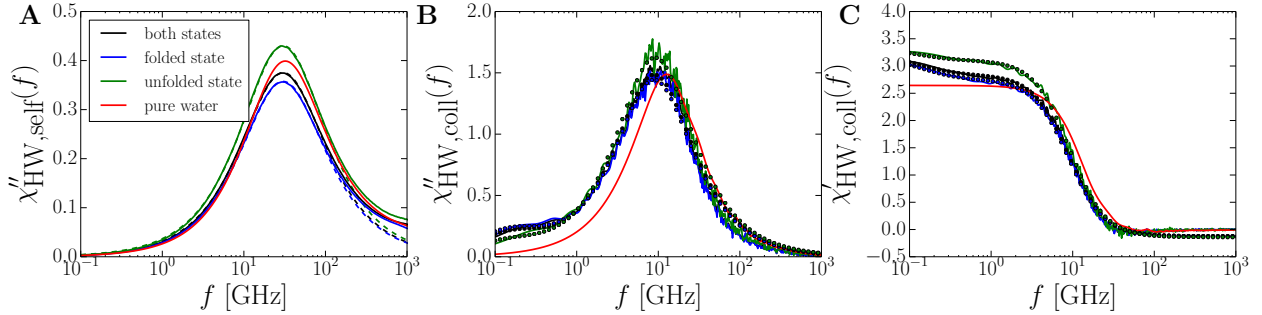

FIGURE 4.9: (A) Imaginary part of the self relaxation of the hydration shell water for folded (blue), unfolded state (green), both states (black line) and pure water (red line): The shape of the response does not depend on the peptide structure. The signal is red-shifted compared to pure bulk water and well described by a Cole-Cole process (dashed lines). In case of an unfolded peptide the amplitude is only higher due to a larger fraction of hydration water. (B) Imaginary part of the collective processes of hydration shell water: Especially for a folded peptide, the spectrum has a second peak in the sub-GHz range. Double Debye fits reproduce the spectral shape well (dotted lines). The main peak is slightly red-shifted compared to bulk water. (C) The static dielectric contribution of the collective processes in the hydration shell is higher than the rescaled collective contribution in pure water. The dielectric spectrum of pure water (red line) is multiplied with the hydration water fraction of 0.05 to compare the amplitudes in all subfigures.

The spectral contributions χ_{HH} (Figure 4.7 D) and χ_{HB} (Figure 4.7 F) show a slow process and a weak secondary structure dependence. In order to further investigate these effects the self relaxation and the collective processes of the combined signal $\chi_{HW} = \chi_{HH} + \chi_{HB}$ are shown secondary structure dependently in Figure 4.9. The self relaxation has a higher amplitude for an unfolded peptide because of the earlier mentioned larger hydration water fraction in this case (Figure 4.9 A, green line). Independent of the secondary structure the self relaxation peak is slightly red-shifted compare to a similar number fraction of pure bulk water (red line) and well described by a Cole-Cole process. The fast self-relaxation time of the hydration shell water of 5.3 ps (Table 4.1) and the absence of slow relaxations shows that all water dipoles even close to the peptide rotate fast.

A slow process only appears in the collective relaxation of the hydration shell water with other water dipoles and is more pronounced for a folded peptide (Figure 4.9 B, blue line). The two peaks can not be well described by a single Cole-Cole fit (not shown). Only a double Debye fit reproduces the spectral shape (dotted lines). The relaxation time of the slower process in a double Debye fit of about 1 ns is almost independent of the secondary structure and the time-scale match with the peptide polarization relaxation time. The amplitude of the slow peak ϵ_1 decreases from 0.38 for folded to 0.20 for unfolded (Table 4.2). The main peak is extended to lower frequencies compare to the rescaled absorption signal of pure bulk water (red line, Figure 4.9 B). The pure water collective contribution, taken from chapter 3, is multiplied with the average hydration water fraction n_H of 0.05 to allow a comparison of the amplitudes in Figure 4.9. The importance of collective effects for dielectric spectra has been stressed before[62] and our findings are in complete agreement with that discussion. Due to the discussed slow process in addition to the bulk resonance, the static

dielectric contribution of the collective relaxations of the hydration shell water is about 20% higher than the collective signal of the same amount of pure water (Figure 4.9 C). The observed dielectric behavior of the hydration shell water with increasing effective static contribution and retarded relaxation time is opposite to effects in the solvation shell of most ions. For instance, sodium-halide solutions show a dielectric decrement and an accelerated collective dynamics compared to pure bulk water, as shown chapter 3. But the effects in this peptide solution as well as in the sodium-halide solutions are line with the Madden-Kivelson-Equation[92], which predicts slower overall dynamics with increasing static dielectric constant due to collective contributions. Mirror-inverted, faster overall dynamics are related to weaker collective effects and a lower static dielectric constant in this theory.

4.4 Summary & Conclusions

Via a projection into folded and unfolded states we have shown that the dielectric spectra of Ala_8 in water are significantly impacted by the peptide structure, especially in the sub-GHz range. If the peptide is folded, the dielectric constant is higher and the low-frequency absorption is increased compared to an unfolded state. In a decomposition we show that the secondary structure mainly affects the spectral contributions involving the peptide polarization. In line with earlier work we find that the contribution of the hydration water polarization auto-correlation exhibits a low frequency process at the similar time-scale as the peptide processes. Our further decomposition of the water polarization correlations into self and collective relaxations points out that the sub-GHz absorption only appears for the collective processes. The absence of slow self relaxations demonstrates that the studied peptide Ala_8 is not able to fix the orientation of single water dipoles over a long time. The existence of slow collective processes inside the hydration shell might be related to the controversially discussed picture of "slaving water" around proteins, where solvent fluctuations control protein dynamics via activation enthalpy[12, 13, 165]. Of course, another possible explanation of the observed slow collective process in the hydration shell is that a slow reorientation of the peptide leads to a collective change in the hydration shell, which would be the picture of a "slaved hydration shell". The second interpretation is supported by the fact that the slow water dielectric relaxation time matches with the rotational tumbling time of the peptide.

The at the first view astonishingly slow relaxation of the cross-term between the polarizations of the hydration shell and outer shell water noticed in earlier publications is explained. Since the cross-term almost exclusively contains collective relaxations between different water molecules, its relaxation time should be compared to the relaxation time of the collective part of the contributions of the different water populations. In this decomposition the cross-term is slower than the collective bulk water relaxation, but faster than the collective hydration water relaxation.

Since the HB cross-contribution ($\tau = 17.5$ ps, Table 4.1) is only 25% slower than collective relaxations in bulk water (BW,coll: $\tau = 14.0$ ps), we do not think that this term is the intermediate time-scale δ-process seen in experiments. Our results show two main peaks: The common bulk water peak and a slow peak at $\tau \approx 1$ ns caused by the peptide and a slow collective water relaxation in the hydration shell. The small differences of the polarization relaxation times of the different components keep the assignment of the intermediate δ-process challenging and prone to

failure. In the future, it would be desirable to redo similar simulations with a much larger peptide and therefore a much slower peptide relaxation time in order to find out whether the slow collective processes in the hydration shell water will adapt to the slower peptide relaxation time. If the adaption is not observed, the slow collective interactions in the hydration shell might be distinguished from the peptide process and found to be the experimentally observed δ-dispersion at intermediate time-scales. Furthermore, experimental spectra for Ala_8 or similar-sized peptides would be welcome to compare them with the simulation results of this study.

Chapter 5

Nanoscale Pumping of Water by AC Electric Fields

Bibliographic information: Parts of this chapter and Appendix C have previously been published. Reprinted with permission from Ref. [iv]. Copyright 2012 by the American Chemical Society.

5.1   Introduction

Carbon nanotubes (CNTs) are ideal connectors for nanofluidic devices, since they allow almost frictionless passage of fluids[20, 22, 23, 24]. To generate flow in these channels, various pump designs based on temperature gradients[25], Coulomb dragging[26] or surface waves[27] were proposed. Two studies suggested the use of static electric fields to pump water through CNTs[166, 167], which in principle seems like a robust and realizable method to drive fluids on the nanoscale. However, this DC-field pumping scenario turned out to be a computer artifact[168, 169, 170], leading directly to the question: can electric fields be used to pump water on the nanoscale, and if so, what is the minimal design for such a pump? We tackle this problem by molecular dynamics (MD) simulations of water inside a single CNT to which an array of electrodes is attached. We indeed find that pumping is possible if the electric field meets two requirements: First, one needs AC fields in a broad GHz frequency range comparable to the dielectric relaxation frequency of water, and secondly, the electrodes must exhibit a finite phase shift that breaks the spatio-temporal symmetry along the CNT axis.

5.2   Pump Design

Our pump design and simulation setup is shown in Figure 5.1 A: A water-filled (20,0) CNT of radius $R = 0.78$ nm and length L of typically 8.5 nm is contacted by an array of n point-like electrodes, which have a mutual separation of d and a distance $\delta = 0.5$ nm to the CNT. The CNT atoms are fixed in space and time, and the SPC/E water model is employed[78]. We use the LAMMPS simulation package[72] with periodic boundary conditions in all three dimensions, fixed water
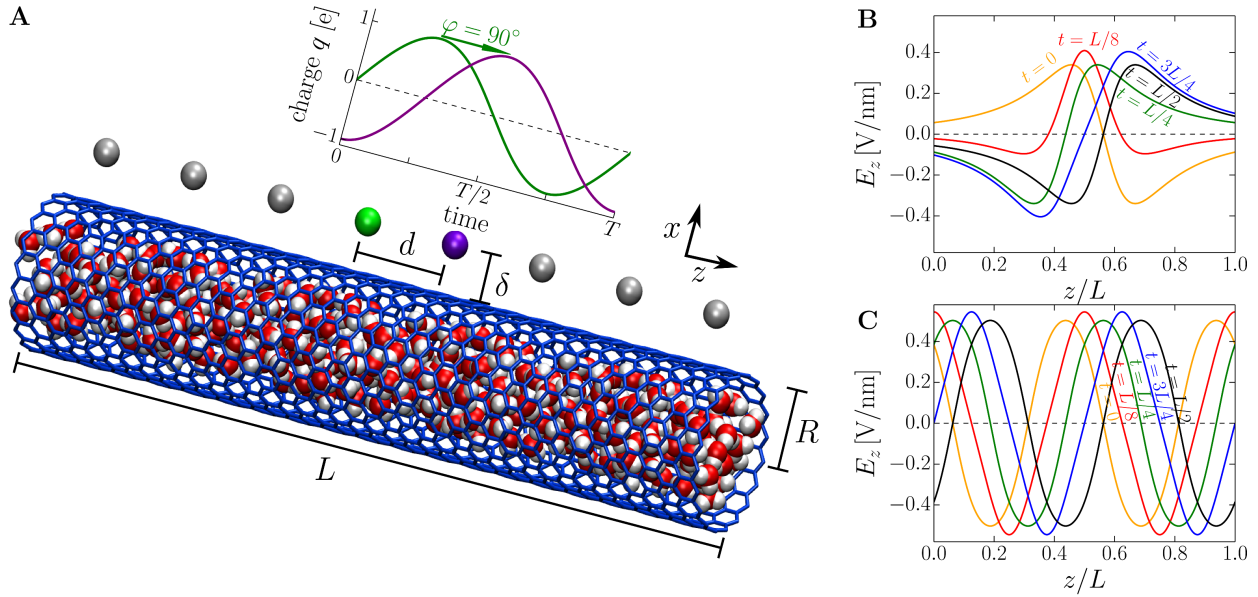
FIGURE 5.1: (A) Illustration of the simulation setup: A water-filled (20,0) CNT of radius $R = 0.78$ nm is contacted by n electrodes placed at mutual separation d and distance $\delta = 0.5$ nm to the CNT atoms. The system is periodically replicated in z-direction. The electrodes correspond to oscillating point charges with period T and phase shift φ between neighboring electrodes, see inset. (B) The electric field in the tube center created by $n = 2$ electrodes, shown at different times during the oscillation period T, is localized and propagates along the z-direction ($d = 1.07$nm, $\varphi = 90°$, $q = 1\,e$) (C) For $n = 8$ electrodes, i.e. a periodic array of equally spaced electrodes, a travelling, almost sinusoidal wave is obtained.

molecule number N and temperature 300 K imposed through a Nose/Hoover thermostat. Before the actual production runs, the CNT is put in contact with a large water reservoir at atmospheric pressure, so that the number of water molecules N inside the CNT can adjust according to the bulk chemical potential; details are given in Appendix C.5. The electrodes are sinusoidally charged with amplitude q, oscillation period T and a finite phase shift φ between neighboring electrodes. In Figure 5.1 B we present the z-component of the electric field in the CNT center caused by $n = 2$ electrodes as function of z at different times for $d = 1.07$ nm, $\varphi = 90°$ and $q = 1\,e$. The spatio-temporal structure of the field corresponds to a wave package with a finite phase velocity which thus polarizes the water and drags polarized molecules along. For a periodic array of $n = 8$ electrodes with a spacing $d = L/8$ the field corresponds to a travelling wave with almost sinusoidal shape, see Figure 5.1 C.

5.3 Polarization Dragging Theory

The finite oscillation period T and finite phase shift φ are key to our nanoscale pumping mechanism: For static electric fields, i.e. for $T \to \infty$, no work is performed on the system once a stationary state is reached since there are no free charges, and according to the laws of thermodynamics, no pumping can be achieved. Finite pumping is only expected for finite T, and we anticipate optimal pumping when T is of the order of the water dielectric relaxation time, as indeed borne out by our simulations and analytic theory. Likewise, when the phase shift is $\varphi = 0$ or $\varphi = 180°$, a standing wave is produced which does not break the spatio-temporal symmetry along the CNT axis. Although the electric field performs work by periodically polarizing water, no direction is

singled out and the flow must be identically zero. For pumping, the phase shift must thus be different from $\varphi = 0$ and $\varphi = 180°$.
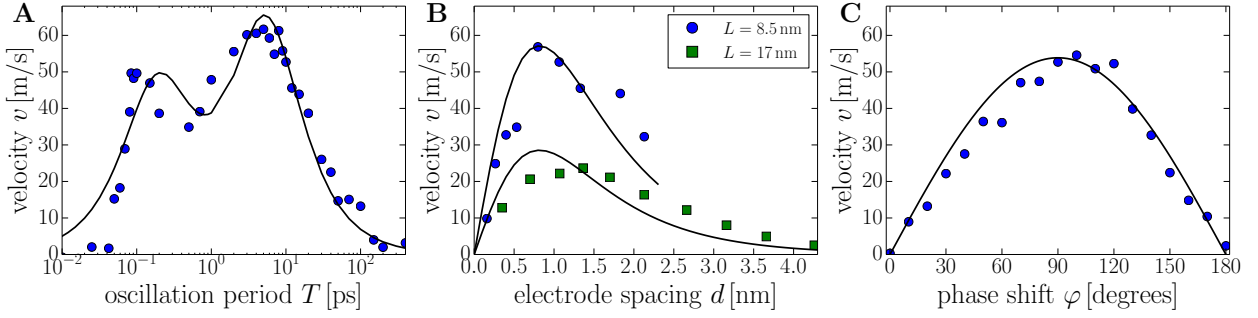

FIGURE 5.2: The simulated average pumping velocity v (data points) for $n = 2$, $q = 1\,e$ is compared with our polarization-dragging theory equation 5.9 (lines). (A) v as a function of the electric field period T is substantial over three orders of magnitude of T ($\varphi = 90°$, $d = 1.07\,\text{nm}$). (B) v as a function of the inter-electrode distance d shows a maximum at $d \approx 1\,\text{nm}$ ($T = 10\,\text{ps}$, $\varphi = 90°$). Here we also include data for tube length $L = 17\,\text{nm}$ which show reduced pumping velocity due to the increased friction. (C) Highest pumping speed is obtained for phase shifts of $\varphi \approx 90°$ ($T = 10\,\text{ps}$, $d = 1.07\,\text{nm}$).

Indeed, Figure 5.2 A exhibits substantial fluid flow for electric-field oscillation periods in the broad range of $T \approx 0.05\,\text{ps}$ to $T \approx 100\,\text{ps}$ (corresponding to frequencies of 10 GHz to 20 THz) for $n = 2$ electrodes and charge amplitude $q = 1\,e$. We attribute the two maxima at $T = 0.1\,\text{ps}$ and 8 ps (corresponding to frequencies of 125 GHz and 10 THz) to the familiar relaxation and libration processes, which occur at somewhat different frequencies than in bulk[171]. Away from these characteristic frequencies, pumping becomes inefficient, as will be explained further below. Figure 5.2 B shows that the optimal electrode-electrode distance is $d \approx 1\,\text{nm}$, of the order of the distance $\delta = 0.5\,\text{nm}$ between electrodes and CNT. Doubling the tube length to $L = 17\,\text{nm}$ results in enhanced water-CNT friction and thus reduces the flow speed by about a factor of two (note that all other data in this chapter are obtained for $L = 8.5\,\text{nm}$). Figure 5.2 C indeed demonstrates that pumping disappears for phase shifts of $\varphi \to 0$ and $\varphi \to 180°$, as argued above, and that the flow velocity is rather symmetric around its maximum at $\varphi = 90°$. All simulation results are in quantitative agreement with a simple theory (shown as lines in Figure 5.2) that is based on a polarization-dragging mechanism and will be introduced in the following.

Neglecting dielectric effects, the electric field created by n oscillating charges with amplitude q at positions $\vec{r}_j$ is

$$\vec{E}(\vec{r}, t) = \frac{q}{4\pi\epsilon_0} \sum_{j=0}^{n-1} \frac{\vec{r} - \vec{r}_j}{|\vec{r} - \vec{r}_j|^3} \sin(\omega t - j\varphi), \tag{5.1}$$

where $\omega = 2\pi/T$ denotes the oscillation frequency and ϵ_0 the vacuum permittivity. For our relatively large tube radius $R = 0.78\,\text{nm}$, water is unstructured[172], so for weak electric fields the dipole moment per water molecule, $\vec{m}(\vec{r}, t)$, should be linear in $\vec{E}$,

$$\vec{m}(\vec{r}, t) = \sum_{k=1}^{2} \alpha_k \tau_k^{-1} \int_{-\infty}^{t} e^{\frac{t'-t}{\tau_k}} \vec{E}(\vec{r}, t') dt' \tag{5.2}$$

where (in hindsight of the simulation results) we assumed two distinct water relaxation modes with relaxation times τ_k and polarizabilities per water molecule α_k and neglected collective polarization effects. In order to relate the dragging force in z-direction $F_z(\vec{r})$ to the local polarization $\vec{m}(\vec{r})$ we expand the electric field $E(\vec{r})$ acting on the three partial charges q_i of a water molecule up to first order:

$$
\begin{aligned}
F_z(\vec{r}) &= \sum_{i=1}^{3} q_i E_z(\vec{r}_i) = -\sum_{i=1}^{3} q_i \frac{\partial}{\partial z}\phi(\vec{r}_i) & (5.3) \\
&= -\sum_{i=1}^{3} q_i \left[\frac{\partial}{\partial z}\phi(\vec{r}) + (\vec{r}_i - \vec{r}) \cdot \vec{\nabla}\frac{\partial}{\partial z}\phi(\vec{r}) + \mathcal{O}^2(\vec{r}_i - \vec{r}) \right] & (5.4) \\
&= -\sum_{i=1}^{3} q_i \left[(\vec{r}_i - \vec{r}) \cdot \vec{\nabla}\frac{\partial}{\partial z}\phi(\vec{r}) + \mathcal{O}^2(\vec{r}_i - \vec{r}) \right] & (5.5) \\
&= -\vec{m} \cdot \vec{\nabla}\frac{\partial}{\partial z}\phi(\vec{r}) + \mathcal{O}^2(\vec{r}_i - \vec{r}) & (5.6) \\
&\approx -\vec{m} \cdot \vec{\nabla}\frac{\partial}{\partial z}\phi(\vec{r}) = -\vec{m} \cdot \frac{\partial}{\partial z}\vec{\nabla}\phi(\vec{r}) & (5.7) \\
&= \vec{m}(\vec{r}) \cdot \vec{\nabla}E_z(\vec{r}) = \vec{m}(\vec{r}) \cdot \frac{\partial}{\partial z}\vec{E}(\vec{r}), & (5.8)
\end{aligned}
$$

where we use the charge neutrality in the step from equation 5.4 to 5.5 to eliminate the zeroth order term. So to leading order, the axial force on a water molecule at position $\vec{r}$ is given by $F_z(\vec{r}, t) = \vec{m}(\vec{r}, t)\partial\vec{E}(\vec{r}, t)/\partial z$. Assuming a homogeneous water distribution within the CNT, we calculate the average force $\bar{F}_z$ on a water molecule by integrating $F_z(\vec{r}, t)$ over the CNT volume and oscillation period T. Presuming a linear force-velocity relation, the average pumping velocity v follows as

$$
v = \frac{N\bar{F}_z}{\gamma L} = \frac{N I_{CNT} \sin\varphi}{\gamma L^2} \left(\frac{q}{4\pi\epsilon_0} \right)^2 \sum_{k=1}^{2} \alpha_k \frac{\omega\tau_k^{-1}}{\omega^2 + \tau_k^{-2}}, \tag{5.9}
$$

where $N = 280$ is the number of water molecules inside the CNT and I_{CNT} is a geometric factor that only depends on the CNT shape and the electrode positions and is calculated in the next section. Equation 5.9 directly demonstrates that the pumping vanishes for high frequencies ($\omega \to \infty$) as well as for the static limit ($\omega \to 0$). By a least square fit to the velocity data in Figure 5.2 A, we obtain $\tau_1 = 0.86\,\text{ps}$, $\tau_2 = 0.03\,\text{ps}$, $\alpha_1 = 7.7 \cdot 10^{-40}\,\text{Cm}^2/\text{V}$ and $\alpha_2 = 5.7 \cdot 10^{-40}\,\text{Cm}^2/\text{V}$. The relaxation times τ_k are about one order of magnitude smaller than in bulk, which is plausible in light of the reduced dimensionality of our system. The polarizabilities α_k are also substantially smaller than in bulk, which reflects that they are effective parameters that take dielectric effects into account.

5.4 Derivation of the Geometric Factor I_{CNT}

In general the geometric factor I_{CNT} can not be obtained analytically. In this section we present numerical results, while in section 5.5 an analytical result in the limit of a long and thin tube is shown. The discussion of our simulation results continues in section 5.6.

For an array of n electrodes at positions $\vec{r}_j$ and a temporal phase shift φ between neighboring electrodes we obtain for the polarization by using equation 5.2:

$$\vec{m}(\vec{r},t) = \sum_{j=0}^{n-1} \sum_{k=1}^{2} \frac{\alpha_k \tau_k^{-1}}{\omega^2 + \tau_k^{-2}} \vec{E}(\vec{r} - \vec{r}_j) \left[\tau_k^{-1} \sin(\omega t - j\varphi) - \omega \cos(\omega t - j\varphi) \right] \qquad (5.10)$$

The z-derivative of the electric field has the following components:

$$\partial E_x(\vec{r},t)/\partial z = \frac{q}{4\pi\epsilon_0} \sum_{j=0}^{n-1} \frac{-3(x-x_j)(z-z_j)}{|\vec{r}-\vec{r}_j|^5} \sin(\omega t - j\varphi) \qquad (5.11)$$

$$\partial E_y(\vec{r},t)/\partial z = \frac{q}{4\pi\epsilon_0} \sum_{j=0}^{n-1} \frac{-3(y-y_j)(z-z_j)}{|\vec{r}-\vec{r}_j|^5} \sin(\omega t - j\varphi) \qquad (5.12)$$

$$\partial E_z(\vec{r},t)/\partial z = \frac{q}{4\pi\epsilon_0} \sum_{j=0}^{n-1} \frac{|\vec{r}-\vec{r}_j|^2 - 3(z-z_j)^2}{|\vec{r}-\vec{r}_j|^5} \sin(\omega t - j\varphi) \qquad (5.13)$$

The force (averaged in space and time) on a water dipole inside a tube can be obtained by integration assuming a homogeneous water density within the effective tube radius $R_{\mathrm{eff}} = R - \sigma_{\mathrm{CO}}/2 = 0.62\,\mathrm{nm}$, where $\sigma_{\mathrm{CO}} = 0.326\,\mathrm{nm}$ is the CNT-water Lennard-Jones diameter:

$$\bar{F}_z = \frac{1}{\pi R_{\mathrm{eff}}^2 L} \int_0^L dz \int_0^{R_{\mathrm{eff}}} \rho\,d\rho \int_0^{2\pi} d\phi \int_0^T \frac{dt}{T} F_z(r, \phi, z, t) \qquad (5.14)$$

Here L is the tube length and T the oscillation period.

Alternatively one could also use the Gibbs radius $R_{\mathrm{Gibbs}} = \sqrt{\frac{N\,m_W}{\pi\,L\,\rho}} = 0.56\,\mathrm{nm}$ as effective radius, where $m_W = 3 \cdot 10^{-26}\,\mathrm{kg}$ is the mass of one water molecule and $\rho = 10^3 \mathrm{kg/m}^3$ is the bulk density of water. An effective radius of $0.56\,\mathrm{nm}$ would increase the relevant geometric coefficient I_{CNT}, which we define later in equation 5.21, by 8%. As a consequence, usage of the Gibbs radius would merely lead to a 8% lower fit value for the polarizability of the k-th mode, α_k, compared to $R_{\mathrm{eff}} = 0.62\,\mathrm{nm}$, without changing the comparison between our simulation data and the theoretical predictions. For our pump with two electrodes at positions $x_1 = x_2 = \delta + R$, $y_1 = y_2 = 0$, $z_1 = L/2 - d/2$ and $z_2 = L/2 + d/2$, equation 5.14 takes the following form:

$$\begin{aligned}
\bar{F}_z = {} & \frac{1}{L} \sum_{k=1}^{2} \left(\frac{q}{4\pi\epsilon_0} \right)^2 \frac{\alpha_k \tau_k^{-1}}{\omega^2 + \tau_k^{-2}} \int_0^T \frac{dt}{T} \left[I_1 \left(\tau_k^{-1} \sin(\omega t) - \omega \cos(\omega t) \right) \sin(\omega t) \right. \\
& + I_2 \left(\tau_k^{-1} \sin(\omega t - \varphi) - \omega \cos(\omega t - \varphi) \right) \sin(\omega t) \\
& + I_3 \left(\tau_k^{-1} \sin(\omega t) - \omega \cos(\omega t) \right) \sin(\omega t - \varphi) \\
& \left. + I_4 \left(\tau_k^{-1} \sin(\omega t - \varphi) - \omega \cos(\omega t - \varphi) \right) \sin(\omega t - \varphi) \right],
\end{aligned} \qquad (5.15)$$

where the spatial integrals I_i are calculated numerically and defined as

$$I_1 = \int \frac{x-x_1}{|\vec{r}-\vec{r}_1|^3} \frac{-3(x-x_1)(z-z_1)}{|\vec{r}-\vec{r}_1|^5} + \frac{z-z_1}{|\vec{r}-\vec{r}_1|^3} \frac{|\vec{r}-\vec{r}_1|^2 - 3(z-z_1)^2}{|\vec{r}-\vec{r}_1|^5} \frac{\mathrm{d}V}{\pi R_{\mathrm{eff}}^2} \qquad (5.16)$$

$$I_2 = \int \frac{x-x_2}{|\vec{r}-\vec{r}_2|^3} \frac{-3(x-x_1)(z-z_1)}{|\vec{r}-\vec{r}_1|^5} + \frac{z-z_2}{|\vec{r}-\vec{r}_2|^3} \frac{|\vec{r}-\vec{r}_1|^2 - 3(z-z_1)^2}{|\vec{r}-\vec{r}_1|^5} \frac{\mathrm{d}V}{\pi R_{\mathrm{eff}}^2} \qquad (5.17)$$

$$I_3 = \int \frac{x-x_1}{|\vec{r}-\vec{r}_1|^3} \frac{-3(x-x_2)(z-z_2)}{|\vec{r}-\vec{r}_2|^5} + \frac{z-z_1}{|\vec{r}-\vec{r}_1|^3} \frac{|\vec{r}-\vec{r}_2|^2 - 3(z-z_2)^2}{|\vec{r}-\vec{r}_2|^5} \frac{\mathrm{d}V}{\pi R_{\mathrm{eff}}^2} \qquad (5.18)$$

$$I_4 = \int \frac{x-x_2}{|\vec{r}-\vec{r}_2|^3} \frac{-3(x-x_2)(z-z_2)}{|\vec{r}-\vec{r}_2|^5} + \frac{z-z_2}{|\vec{r}-\vec{r}_2|^3} \frac{|\vec{r}-\vec{r}_2|^2 - 3(z-z_2)^2}{|\vec{r}-\vec{r}_2|^5} \frac{\mathrm{d}V}{\pi R_{\mathrm{eff}}^2}, \qquad (5.19)$$

where $\mathrm{d}V = \rho \, \mathrm{d}\rho \, \mathrm{d}\Phi \, \mathrm{d}z$ is a short hand notation for the volume element. Exploiting the symmetry of the system, we obtain for $\delta = 0.5\,\mathrm{nm}$, $d = 1.07\,\mathrm{nm}$ and $L = 8.5\,\mathrm{nm}$ numerically:

$$I_4 = -I_1 \simeq 1.2 \cdot 10^{-5}\mathrm{nm}^{-4} \qquad (5.20)$$

$$I_{\mathrm{CNT}} \equiv I_3 = -I_2 \simeq 4.9 \cdot 10^{-1}\mathrm{nm}^{-4} \qquad (5.21)$$

After performing the time integration in equation 5.15 we obtain

$$\bar{F}_z = \frac{I_{\mathrm{CNT}} \sin\varphi}{L} \left(\frac{q}{4\pi\epsilon_0}\right)^2 \sum_{k=1}^{2} \alpha_k \frac{\omega\tau_k^{-1}}{\omega^2 + \tau_k^{-2}}. \qquad (5.22)$$

By using the linear relation $v = N\bar{F}_z/\gamma L$, we calculate the pumping velocity as

$$v = \frac{NI_{CNT}\sin\varphi}{\gamma L^2} \left(\frac{q}{4\pi\epsilon_0}\right)^2 \sum_{k=1}^{2} \alpha_k \frac{\omega\tau_k^{-1}}{\omega^2 + \tau_k^{-2}},$$

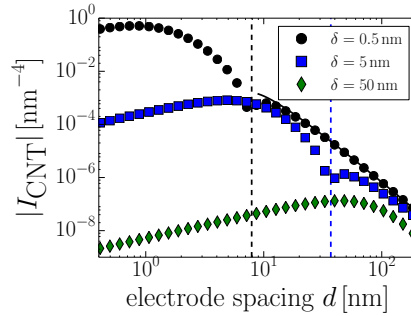which is the result presented on the right side of equation 5.9.

FIGURE 5.3: The absolute value of the geometric coefficient I_{CNT} (dots) as a function of d for $L = 1704\,\mathrm{nm}$, $R = 0.78\,\mathrm{nm}$ and three different values of δ: The coefficient I_{CNT} is positive for small d and changes sign for $d \gg \delta$ (dashed vertical lines). The numerical results for $\delta = 0.5\,\mathrm{nm}$ converge against the analytically determined asymptotic behavior (black, solid line).

We can also calculate I_{CNT} numerically for large systems that cannot be studied in MD simulations. In Figure 5.3 we present our numerical results for a tube length L of $1704\,\mathrm{nm}$ as a function of the electrode separation d for three different values of δ. We first observe that for parameters $d = 1.07\,\mathrm{nm}$ and $\delta = 0.5\,\mathrm{nm}$ we recover the same result for I_{CNT} as found previously for $L = 8.52\,\mathrm{nm}$, showing that the finite tube length influences the result only very weakly. As the electrode

separation d increases, the magnitude of I_{CNT} goes down and for large d we observe a sign change (dashed vertical lines in Figure 5.3), meaning that the flow changes its direction.

In the limit of $L \to \infty$ and $d \gg \delta + R$ the analytic asymptotic behavior of I_{CNT}, which is derived in detail in the following section, reads

$$I_{\mathrm{asy}} = -24 d^{-4} \ln(d/R) + \mathcal{O}(d^{-4}), \tag{5.23}$$

which is shown as a black solid line in Figure 5.3 and describes the data well for large d.

5.5 Analytic Expansion for Long Thin Tubes

In this section we expand I_{CNT} in the long tube limit ($L \to \infty$, $d \gg R + \delta$) to obtain an analytic result. By defining $\epsilon = R_{\mathrm{eff}}/d$ and $\tilde{b} = (\delta + R)/R_{\mathrm{eff}}$ we can rewrite $I_{\mathrm{CNT}} = I_3 = \frac{\epsilon^2}{\pi R_{\mathrm{eff}}^4} F(\epsilon)$ as

$$F(\epsilon) = \int\limits_0^\epsilon \mathrm{d}\tilde{\rho} \int\limits_0^{2\pi} \mathrm{d}\phi \int\limits_{-\infty}^\infty \mathrm{d}\tilde{z} \frac{\tilde{\rho}(\tilde{z}+0.5)[(\tilde{\rho}\cos\phi - \tilde{b}\epsilon)^2 + \tilde{\rho}^2\sin^2\phi - 2(\tilde{z}-0.5)^2]}{[(\tilde{\rho}\cos\phi - \tilde{b}\epsilon)^2 + \tilde{\rho}^2\sin^2\phi + (\tilde{z}+0.5)^2]^{1.5}[(\tilde{\rho}\cos\phi - \tilde{b}\epsilon)^2 + \tilde{\rho}^2\sin^2\phi + (\tilde{z}-0.5)^2]^{2.5}}. \tag{5.24}$$

In the limit of large d we expand $F(\epsilon)$ in a Taylor series of small ϵ around 0:

$$F(\epsilon) \approx F_0(\epsilon = 0) + F_1(\epsilon = 0)\epsilon + F_2(\epsilon = 0)\epsilon^2/2, \tag{5.25}$$

where $F_k(\epsilon) = \partial^k F(\epsilon)/\partial \epsilon^k$. The first derivative of $F(\epsilon)$ cancels the $\tilde{\rho}$-integration and we have

$$F_1(\epsilon) = \int\limits_0^{2\pi} \mathrm{d}\phi \int\limits_{-\infty}^\infty \mathrm{d}\tilde{z} \frac{\epsilon(\tilde{z}+0.5)[\epsilon^2(1 - 2\tilde{b}\cos\phi + \tilde{b}^2) - 2(\tilde{z}-0.5)^2]}{[\epsilon^2(1 - 2\tilde{b}\cos\phi + \tilde{b}^2) + (\tilde{z}+0.5)^2]^{1.5}[\epsilon^2(1 - 2\tilde{b}\cos\phi + \tilde{b}^2) + (\tilde{z}-0.5)^2]^{2.5}}, \tag{5.26}$$

where we use the notations $b^2 = b^2(\phi) = (1 - 2\tilde{b}\cos\phi + \tilde{b}^2)$ and $\eta = b\epsilon$. By excluding the integration over ϕ and using $z = \tilde{z}$ we can write equation 5.26 in more compact form:

$$\tilde{F}_1(\eta) = \frac{1}{b} \int\limits_{-\infty}^\infty \mathrm{d}z \frac{\eta(z+0.5)[\eta^2 - 2(z-0.5)^2]}{[\eta^2 + (z+0.5)^2]^{1.5}[\eta^2 + (z-0.5)^2]^{2.5}} \tag{5.27}$$

In the limit of $\eta \to 0$ the integrand vanishes. Therefore, we go to the next order:

$$F_2(\epsilon) = \int\limits_0^{2\pi} \mathrm{d}\phi \int\limits_{-\infty}^\infty \mathrm{d}\tilde{z} \frac{(\tilde{z}+0.5)[\epsilon^2(1 - 2\tilde{b}\cos\phi + \tilde{b}^2) - 2(\tilde{z}-0.5)^2]}{[\epsilon^2(1 - 2\tilde{b}\cos\phi + \tilde{b}^2) + (\tilde{z}+0.5)^2]^{1.5}[\epsilon^2(1 - 2\tilde{b}\cos\phi + \tilde{b}^2) + (\tilde{z}-0.5)^2]^{2.5}}$$

$$+ \frac{2\epsilon^2(\tilde{z}+0.5)(1 - 2\tilde{b}\cos\phi + \tilde{b}^2)}{[\epsilon^2(1 - 2\tilde{b}\cos\phi + \tilde{b}^2) + (\tilde{z}+0.5)^2]^{1.5}[\epsilon^2(1 - 2\tilde{b}\cos\phi + \tilde{b}^2) + (\tilde{z}-0.5)^2]^{2.5}}$$

$$+ \frac{-3\epsilon^2(\tilde{z}+0.5)(1 - 2\tilde{b}\cos\phi + \tilde{b}^2)[\epsilon^2(1 - 2\tilde{b}\cos\phi + \tilde{b}^2) - 2(\tilde{z}-0.5)^2]}{[\epsilon^2(1 - 2\tilde{b}\cos\phi + \tilde{b}^2) + (\tilde{z}+0.5)^2]^{2.5}[\epsilon^2(1 - 2\tilde{b}\cos\phi + \tilde{b}^2) + (\tilde{z}-0.5)^2]^{2.5}}$$

$$+ \frac{-5\epsilon^2(\tilde{z}+0.5)(1 - 2\tilde{b}\cos\phi + \tilde{b}^2)[\epsilon^2(1 - 2\tilde{b}\cos\phi + \tilde{b}^2) - 2(\tilde{z}-0.5)^2]}{[\epsilon^2(1 - 2\tilde{b}\cos\phi + \tilde{b}^2) + (\tilde{z}+0.5)^2]^{1.5}[\epsilon^2(1 - 2\tilde{b}\cos\phi + \tilde{b}^2) + (\tilde{z}-0.5)^2]^{3.5}}. \tag{5.28}$$

Or more compactly written by excluding the ϕ-integration:

$$\tilde{F}_2(\eta) = \int\limits_{-\infty}^{\infty} dz \frac{(z+0.5)[\eta^2 - 2(z-0.5)^2]}{[\eta^2 + (z+0.5)^2]^{1.5}[\eta^2 + (z-0.5)^2]^{2.5}}$$

$$+ \frac{2\eta^2(z+0.5)}{[\eta^2 + (z+0.5)^2]^{1.5}[\eta^2 + (z-0.5)^2]^{2.5}}$$

$$+ \frac{-3\eta^2(z+0.5)[\eta^2 - 2(z-0.5)^2]}{[\eta^2 + (z+0.5)^2]^{2.5}[\eta^2 + (z-0.5)^2]^{2.5}}$$

$$+ \frac{-5\eta^2(z+0.5)[\eta^2 - 2(z-0.5)^2]}{[\eta^2 + (z+0.5)^2]^{1.5}[\eta^2 + (z-0.5)^2]^{3.5}}. \tag{5.29}$$

The last three terms are two orders higher in η and therefore only the first term of the integrand of equation 5.29 is relevant:

$$g(z,\eta) = \frac{(z+0.5)[\eta^2 - 2(z-0.5)^2]}{[\eta^2 + (z+0.5)^2]^{1.5}[\eta^2 + (z-0.5)^2]^{2.5}} \tag{5.30}$$

If we would set η to zero, we would receive:

$$g_0(z) = \frac{-2(z+0.5)}{|z+0.5|^3|z-0.5|^3} \tag{5.31}$$

Since $g_0(z)$ has poles at $z_1 = -0.5$ and $z_2 = 0.5$ we first have to discuss the integrand around these poles.

5.5.1 Analytical Discussion of the First Pole at $z_1 = -0.5$

For the calculation of the integral over g to close to the pole at $z_1 = -0.5$, we can use the following approximation $g_1(z,\eta)$ with finite η if we shift by -0.5:

$$g_1(z,\eta) = \frac{z[\eta^2 - 2(z-1)^2]}{[\eta^2 + z^2]^{1.5}[\eta^2 + (z-1)^2]^{2.5}} = \frac{z(\eta^2 - 2) + 4z^2 - 2z^3}{[\eta^2 + z^2]^{1.5}[\eta^2 + 1 - 2z + z^2]^{2.5}} \tag{5.32}$$

$$= \frac{z(\eta^2 - 2) + 4z^2 - 2z^3}{[\eta^2 + z^2]^{1.5}[\eta^2 + 1]^{2.5}} \left(1 - \frac{5}{2}\left[\frac{-2+2z}{\eta^2+1}\right]_{z=0} z + \mathcal{O}(z^2)\right) \tag{5.33}$$

$$\approx \frac{z(\eta^2 - 2) - 6z^2 + \mathcal{O}(z^3)}{[\eta^2 + z^2]^{1.5}} \tag{5.34}$$

If we integrate $g_1(z,\eta)$ around $z = 0$ for $0 < \Delta \leq 0.5$, only even order terms of z remain in the nominator, since the denominator is even:

$$\int\limits_{-\Delta}^{\Delta} g_1(z,\eta)dz = \int\limits_{-\Delta}^{\Delta} \frac{z(\eta^2 - 2) - 6z^2 + \mathcal{O}(z^3)}{[\eta^2 + z^2]^{1.5}}dz = \int\limits_{-\Delta}^{\Delta} \frac{-6z^2 + \mathcal{O}(z^4)}{[\eta^2 + z^2]^{1.5}}dz \tag{5.35}$$

$$= \int\limits_{-\Delta}^{\Delta} s(z,\eta)dz + \mathcal{O}(\Delta), \tag{5.36}$$

where

$$s(z, \eta) = \frac{-6z^2}{[\eta^2 + z^2]^{1.5}}. \tag{5.37}$$

We can split up the integrand $s(z, \eta)$ in two parts:

$$s_1(z, \eta) = \frac{\eta^2 + z^2}{[\eta^2 + z^2]^{1.5}} = \frac{1}{[\eta^2 + z^2]^{0.5}} \tag{5.38}$$

$$s_2(z, \eta) = \frac{1}{[\eta^2 + z^2]^{1.5}} \tag{5.39}$$

$$s(z, \eta) = -6s_1(z, \eta) + 6\eta^2 s_2(z, \eta) \tag{5.40}$$

Now we want to extract the scale behaviour of the integral over s_1 for $\eta \ll \Delta$:

$$\int_{-\Delta}^{\Delta} s_1(z, \eta) dz = \int_{-\Delta}^{\Delta} \frac{1}{[\eta^2 + z^2]^{0.5}} dz = 2 \int_{0}^{\Delta} \frac{1}{[\eta^2 + z^2]^{0.5}} dz \tag{5.41}$$

$$\approx 2 \int_{0}^{\Delta} \frac{1}{\eta + z} dz = 2 \ln(\eta + \Delta) - 2 \ln(\eta) \tag{5.42}$$

$$= -2 \ln(\eta) + 2 \ln(\Delta) + \mathcal{O}(\eta/\Delta) = -2 \ln(\eta) + \mathcal{O}(1) \tag{5.43}$$

The leading term does not depend on Δ. For s_2 we can obtain:

$$\int_{-\Delta}^{\Delta} s_2(z, \eta) dz = \int_{-\Delta}^{\Delta} \frac{1}{[\eta^2 + z^2]^{1.5}} dz = 2 \int_{0}^{\Delta} \frac{1}{[\eta^2 + z^2]^{1.5}} dz \tag{5.44}$$

$$= \left[\frac{z}{\eta^2 \sqrt{\eta^2 + z^2}} \right]_{z=0}^{z=\Delta} = \frac{\Delta}{\eta^2 \sqrt{\eta^2 + \Delta^2}} = \mathcal{O}(\eta^{-2}) \tag{5.45}$$

So we obtain for s:

$$\int_{-\Delta}^{\Delta} s(z, \eta) dz = -6 \int_{-\Delta}^{\Delta} s_1(z, \eta) dz + 6\eta^2 \int_{-\Delta}^{\Delta} s_2(z, \eta) dz \tag{5.46}$$

$$\approx 12 \ln(\eta) + \mathcal{O}(1) = C \ln(\eta) + \mathcal{O}(1), \tag{5.47}$$

with $C = 12$. Now we estimate the error of our approximation from equation 5.41 to equation 5.42 for $\eta < 0.5$ and $0 \leq z \leq 0.5$:

$$0 \leq \eta z \leq \eta^2 + z^2 \Leftrightarrow (\eta^2 + z^2) \leq (\eta + z)^2 \leq 3(\eta^2 + z^2) \Leftrightarrow \frac{1}{\sqrt{\eta^2 + z^2}} \geq \frac{1}{\eta + z} \geq \frac{1}{3\sqrt{\eta^2 + z^2}}. \tag{5.48}$$

As result we can say that:

$$C \ln(\eta) + \mathcal{O}(1) \geq \int_{-\Delta}^{\Delta} s(z, \eta) dz \geq \frac{C}{3} \ln(\eta) + \mathcal{O}(1) \tag{5.49}$$

We can conclude that first pole of g shows a logarithmic divergence for small η:

$$\int_{-1}^{0} g(z,\eta)\mathrm{d}z = \tilde{C}\ln(\eta) + \mathcal{O}(1), \tag{5.50}$$

where $\tilde{C} \approx C$, since our approximation by using equation 5.48 is accurate at the pole.

5.5.2 Analytical Discussion of the Second Pole at $z_2 = 0.5$

If we shift $g(z,\eta)$ by $+0.5$, we receive:

$$\tilde{g}(z,\eta) \;=\; \frac{(z+1)(\eta^2 - 2z^2)}{[\eta^2 + (z+1)^2]^{1.5}[\eta^2 + z^2]^{2.5}} = \frac{\eta^2 + \eta^2 z - 2z^2 - 2z^3}{[\eta^2 + 1 + 2z + z^2]^{1.5}[\eta^2 + z^2]^{2.5}} \tag{5.51}$$

In order to integrate $\tilde{g}$ analytically around $z = 0$ we expand the left factor in the denominator around $z = 0$:

$$a(z) \;=\; \frac{1}{[\eta^2 + 1 + 2z + z^2]^{1.5}} = 1 - 3z + 6z^2 - 10z^3 + \frac{955}{24}z^4 + \mathcal{O}(z^5). \tag{5.52}$$

If we insert the expansion of $a(z)$ in equation 5.51, we obtain:

$$\tilde{g}(z,\eta) \;=\; \frac{\eta^2 + \eta^2 z - 2z^2 - 2z^3}{[\eta^2 + z^2]^{2.5}}\left(1 - 3z + 6z^2 - 10z^3 + \frac{955}{24}z^4 + \mathcal{O}(z^5)\right) \tag{5.53}$$

$$\;=\; \frac{\eta^2 + 2\eta^2 z + (-2 + 3\eta^2)z^2 + (-4 + 4\eta^2)z^3 + (-6 + \frac{715}{24}\eta^2)z^4 + \mathcal{O}(z^5)}{[\eta^2 + z^2]^{2.5}} \tag{5.54}$$

Since the denominator is even and we integrate from $-\Delta$ to $+\Delta$, we only have to consider even terms in z in the nominator:

$$g_2(z,\eta) \;=\; \frac{\eta^2 + (-2 + 3\eta^2)z^2 + (-6 + \frac{715}{24}\eta^2)z^4}{[\eta^2 + z^2]^{2.5}} \tag{5.55}$$

We split the integrand in the following terms:

$$u_1(z,\eta) \;=\; \frac{\eta^2}{[\eta^2 + z^2]^{2.5}} \tag{5.56}$$

$$u_2(z,\eta) \;=\; \frac{(-2 + 3\eta^2)z^2}{[\eta^2 + z^2]^{2.5}} \tag{5.57}$$

$$u_3(z,\eta) \;=\; \frac{1}{[\eta^2 + z^2]^{0.5}} = s_1(z,\eta) \tag{5.58}$$

$$u_4(z,\eta) \;=\; \frac{\eta^2 z^2}{[\eta^2 + z^2]^{2.5}} \tag{5.59}$$

$$u_5(z,\eta) \;=\; \frac{\eta^4}{[\eta^2 + z^2]^{2.5}}, \tag{5.60}$$

where

$$g_2(z,\eta) = u_1(z,\eta) + u_2(z,\eta) + \left(-6 + \frac{715}{24}\eta^2\right)[u_3(z,\eta) - 2u_4(z,\eta) - u_5(z,\eta)]. \tag{5.61}$$

Analogously to the discussion of the first pole we will now integrate the functions $u_i(z, \eta)$ from $-\Delta$ to $+\Delta$ up to leading order for $0 < \Delta \leq 0.5$ and assume $\eta \ll \Delta$:

$$\int_{-\Delta}^{\Delta} u_1(z, \eta) \mathrm{d}z = 2 \int_0^{\Delta} \frac{\eta^2}{[\eta^2 + z^2]^{2.5}} \mathrm{d}z = 2 \left[\frac{\eta^2 z + 2z^3/3}{\eta^2 [\eta^2 + z^2]^{1.5}} \right]_{z=0}^{z=\Delta} = \frac{2\Delta}{[\eta^2 + \Delta^2]^{1.5}} + \frac{4\Delta^3/3}{\eta^2 [\eta^2 + \Delta^2]^{1.5}}$$

$$= \frac{4\Delta^3/3}{\eta^2 [\eta^2 + \Delta^2]^{1.5}} + \mathcal{O}(\Delta^{-2}) = \frac{4\Delta^3/3}{\eta^2 [\eta^2 + \Delta^2]^{1.5}} + \mathcal{O}(1) \tag{5.62}$$

$$\int_{-\Delta}^{\Delta} u_2(z, \eta) \mathrm{d}z = 2 \int_0^{\Delta} \frac{(-2 + 3\eta^2)z^2}{[\eta^2 + z^2]^{2.5}} \mathrm{d}z = 2 \left[\frac{\eta^2 z - 2z^3/3}{\eta^2 [\eta^2 + z^2]^{1.5}} \right]_{z=0}^{z=\Delta} = \frac{2\Delta}{[\eta^2 + \Delta^2]^{1.5}} - \frac{4\Delta^3/3}{\eta^2 [\eta^2 + \Delta^2]^{1.5}}$$

$$= -\frac{4\Delta^3/3}{\eta^2 [\eta^2 + \Delta^2]^{1.5}} + \mathcal{O}(\Delta^{-2}) = -\frac{4\Delta^3/3}{\eta^2 [\eta^2 + \Delta^2]^{1.5}} + \mathcal{O}(1) \tag{5.63}$$

The integral over $u_3(z, \eta) = s_1(z, \eta)$ has been calculated during the discussion of the first pole:

$$\int_{-\Delta}^{\Delta} u_3(z, \eta) \mathrm{d}z = \int_{-\Delta}^{\Delta} s_1(z, \eta) \mathrm{d}z = 2 \int_0^{\Delta} \frac{1}{[\eta^2 + z^2]^{0.5}} \mathrm{d}z \tag{5.64}$$

$$\approx 2 \int_0^{\Delta} \frac{1}{\eta + z} \mathrm{d}z = 2 \ln(\eta + \Delta) - 2 \ln(\eta) \tag{5.65}$$

$$= -2 \ln(\eta) + 2 \ln(\Delta) + \mathcal{O}(\eta/\Delta) = -2 \ln(\eta) + \mathcal{O}(1) \tag{5.66}$$

The leading term does not depend on Δ.

$$\int_{-\Delta}^{\Delta} u_4(z, \eta) \mathrm{d}z = 2 \int_0^{\Delta} \frac{\eta^2 z^2}{[\eta^2 + z^2]^{2.5}} \mathrm{d}z = 2 \left[\frac{z^3/3}{\eta^2 [\eta^2 + z^2]^{1.5}} \right]_{z=0}^{z=\Delta}$$

$$= \frac{2\Delta^3/3}{[\eta^2 + \Delta^2]^{1.5}} = \mathcal{O}(1) \tag{5.67}$$

$$\int_{-\Delta}^{\Delta} u_5(z, \eta) \mathrm{d}z = 2 \int_0^{\Delta} \frac{\eta^4}{[\eta^2 + z^2]^{2.5}} \mathrm{d}z = 2 \left[\frac{\eta^2 z + 2z^3/3}{[\eta^2 + z^2]^{1.5}} \right]_{z=0}^{z=\Delta}$$

$$= \frac{\eta^2 \Delta + 2\Delta^3/3}{[\eta^2 + \Delta^2]^{1.5}} = \mathcal{O}(1). \tag{5.68}$$

By inserting into equation 5.61 we obtain:

$$\int_{-\Delta}^{\Delta} g_2(z, \eta) \mathrm{d}z = \frac{4\Delta^3/3}{\eta^2 [\eta^2 \Delta^2]^{1.5}} - \frac{4\Delta^3/3}{\eta^2 [\eta^2 \Delta^2]^{1.5}} - 2 \ln(\eta)(-6 + \frac{715}{24}\eta^2) + \mathcal{O}(1) = C \ln(\eta) + \mathcal{O}(1), \tag{5.69}$$

with $C = 12$. The final result of the z-integration is:

$$\int_{-\infty}^{\infty} g(z,\eta)\mathrm{d}z = \int_{-1}^{1} g(z,\eta)\mathrm{d} + \mathcal{O}(1) = 2\int_{0}^{0.5} g_1(z,\eta)\mathrm{d} + 2\int_{0}^{0.5} g_2(z,\eta)\mathrm{d} + \mathcal{O}(1) \tag{5.70}$$

$$= 2C\ln(\eta) + \mathcal{O}(1) = 24\ln(\eta) + \mathcal{O}(1) \tag{5.71}$$

The ϕ-integration is trivial for the leading term of $F_2(\epsilon)$:

$$F_2(\epsilon) = \int_{0}^{2\pi} \mathrm{d}\phi \int_{-\infty}^{\infty} g(z,\eta)\mathrm{d}z = \int_{0}^{2\pi} \mathrm{d}\phi\,[24\ln(\eta) + \mathcal{O}(1)] \tag{5.72}$$

$$= \int_{0}^{2\pi} \mathrm{d}\phi\,[24\ln(\epsilon) + \mathcal{O}(1)] = 48\pi\ln(\epsilon) + \mathcal{O}(1) \tag{5.73}$$

The final results of the expansion is

$$I_{\mathrm{CNT}} = \frac{\epsilon^2}{\pi R_{\mathrm{eff}}^4} F(\epsilon) \approx \frac{\epsilon^4}{2\pi R_{\mathrm{eff}}^4} F_2(\epsilon) \tag{5.74}$$

$$= 24\frac{\epsilon^4}{R_{\mathrm{eff}}^4}\ln(\epsilon) + \mathcal{O}(\epsilon^4) = -24d^{-4}\ln(d/R) + \mathcal{O}(d^{-4}),$$

as mentioned earlier in equation 5.23. In Figure 5.3 we use for the solid black lines:

$$|I_{\mathrm{CNT}}(d)| = 24d^{-4}\ln(d/R) + C_0 d^{-4}, \tag{5.75}$$

where the second leading order amplitude $C_0 = -44.1$ is obtained from a fit to the numerical data.

5.6 Parameter Dependence

The polarization-dragging theory (equation 5.9), shown as lines in Figure 5.2, is in excellent agreement with simulations and in particular reproduces the frequency and phase-shift dependency of the velocity in Figure 5.2 A and Figure 5.2 C. Our theory predicts that the pumping effect vanishes for static fields $\omega \to 0$ and for standing waves, $\varphi = 0$ or $\varphi = 180°$, since in these limits the water polarization is not coupled to an electric-field gradient and thus no thrust is generated.

In Figure 5.4 A we show simulation data for $m_z(\vec{r},t)$ for different times as a function of z (data points), the relative weak polarization justifies our use of linear response theory. The lines according to equation 5.2 satisfactorily match the simulation data, our theory therefore not only describes the average pumping speed but also spatio-temporal details of the propagating polarization wave within the CNT. This suggests that our setup of oscillating phase-shifted charges indeed actuates water by a polarization-dragging mechanism, and not by a rotation-translation-coupling scenario[167, 170, 173], as confirmed by additional data in Appendix C.3. The maximal possible pumping speed is given by the phase velocity

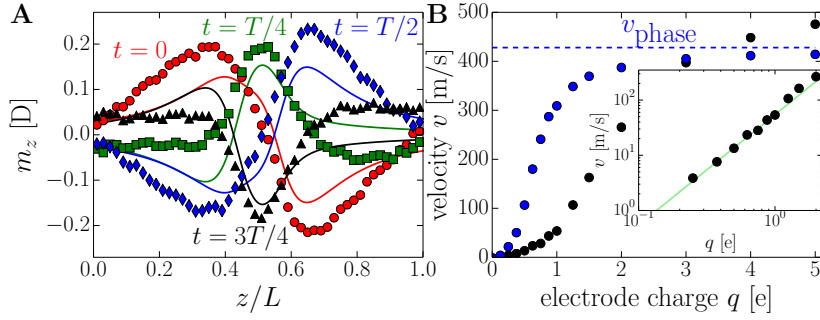$$v_{\mathrm{phase}} = \frac{\omega}{\varphi/d} = \frac{d}{T}\frac{2\pi}{\varphi}, \tag{5.76}$$

FIGURE 5.4: (A) The z-component of the induced water dipole moment m_z for $n = 2$, $T = 10\,\text{ps}$, $q = 1\,e$ and $d = 1.07\,\text{nm}$ as a function of z for various times; full water orientation would correspond to $m_z \approx 2.3\,\text{D}$. Lines denote predictions according to equation 5.2. (B) Velocity v for $T = 10\,\text{ps}$, $d = 1.07\,\text{nm}$ as a function of the electrode charge q: v converges for high q towards the electric phase velocity v_{phase} (equation 5.76, dashed line). Inset: For low q the velocity depends quadratically on q (green line), as predicted by the polarization-dragging theory (equation 5.9).

which indeed is reached for high electrode charge q, as shown in Figure 5.4 B. For small q, v depends quadratically on q, as predicted by our polarization-dragging theory (equation 5.9) and demonstrated in the inset.
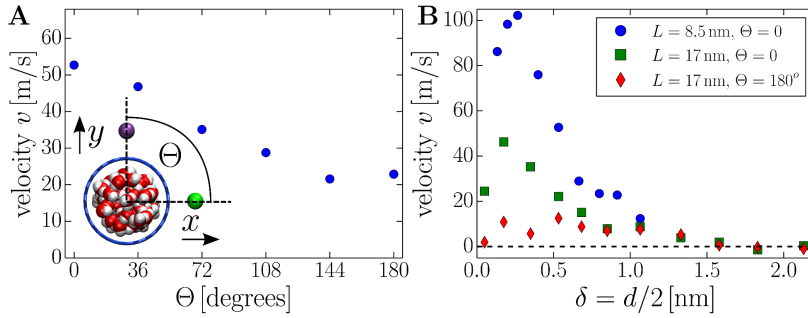

FIGURE 5.5: (A) The velocity as a function of the electrode-tube-electrode angle Θ shows that even when the electrodes are attached to the tube from different sides, i.e. $\Theta = 180^o$, the pump remains operative ($\delta = 0.5\,\text{nm}$, $d = 1.07\,\text{nm}$). (B) The velocity as a function of the distance between the electrode and the tube wall $\delta = d/2$ for $\Theta = 0$: The fastest pumping is found for $\delta \approx 0.3\,\text{nm}$. (All data for $n = 2$, $T = 10\,\text{ps}$, $q = 1\,e$, $\varphi = \pi/2$ and $L = 8.5\,\text{nm}$.)

In an experimental setup, it might be more convenient to locate the two electrodes at a finite electrode-tube-electrode angle Θ, as indicated in the inset of Figure 5.5 A. The influence of Θ on the pumping speed is shown in Figure 5.5 A. We find that the pump remains operative even when the electrodes are attached to different sides of the tube. In Figure 5.5 B we study the dependence of the flow velocity on the distance δ between the electrodes and the CNT. In the simulations, we simultaneously increase the electrode spacing according to $d = 2\delta$. The pumping speed shows a maximum at $\delta \approx 0.3\,\text{nm}$, i.e., when the electrodes are relatively close to the tube wall.

5.7 Efficieny

We now turn to the efficiency $\eta = P_{\text{mech}}/P_{\text{el}}$ of our nanopump, defined as the ratio of extracted mechanical power P_{mech} and consumed electric power P_{el}. P_{el} follows from the electrostatic potentials due to water polarization at the two electrodes, $\phi_{\text{wat,i}}(t)$, multiplied by the electric currents
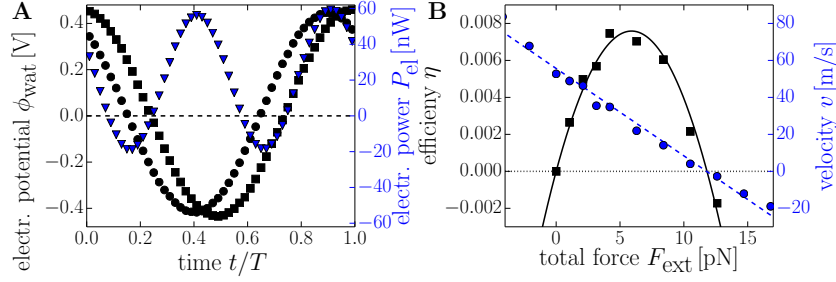
FIGURE 5.6: (A) Electrostatic potentials $\phi_{\text{wat,i}}(t)$ (circles and squares) at the two electrodes due to water dipole orientation and instantaneous consumed electric power (triangles). (B) Velocity v and pumping efficiency $\eta = P_{\text{mech}}/P_{\text{el}}$ as a function of the external force F_{ext}. All data for $n = 2$, $T = 10\,\text{ps}$, $q = 1\,e$ and $d = 1.07\,\text{nm}$.

$\dot{q}_i(t)$,

$$P_{\text{el}} = \frac{1}{T} \int_0^T \phi_{\text{wat,1}}(t)\dot{q}_1(t) + \phi_{\text{wat,2}}(t)\dot{q}_2(t)\, dt. \tag{5.77}$$

The potentials $\phi_{\text{wat,i}}(t)$ (black circles and squares in Figure 5.6 A) reach maximal values of around 0.4 V, the average consumed electric power (average over the blue triangles in Figure 5.6 A is $P_{el} = 19.6\,\text{nW}$). In order to extract mechanical work, we apply an external force F_{ext}, in the form of a gravitational force acting equally on all atoms, opposite to the flux. In Figure 5.6 B we see that v decreases linearly with F_{ext} according to $v = (F_{\text{ext}}^{\text{max}} - F_{\text{ext}})/(\gamma L)$ (dashed line), from which we extract the friction coefficient $\gamma L = 0.21\,\text{pN s/m}$ and the friction coefficient per unit length, $\gamma = 2.5 \cdot 10^{-5}\,\text{N s/m}^2$, used in describing the simulation data in Figure 5.2. This corresponds to a friction per area $\lambda = \gamma/(2\pi R_{\text{eff}}) = 7 \cdot 10^3\,\text{N s/m}^3$, considerably higher than the value $\lambda = 3 \cdot 10^3\,\text{N s/m}^3$ for a bare CNT[21], which means that the oscillating driving charges produce considerable friction on their own (following previous work[21], the effective CNT radius is defined as $R_{\text{eff}} = R - \sigma_{\text{CO}}/2 = 0.62\,\text{nm}$, where $\sigma_{\text{CO}} = 0.326\,\text{nm}$ is the CNT-water Lennard-Jones diameter). The mechanical output power is $P_{\text{mech}} = vF_{\text{ext}} \simeq F_{\text{ext}}(F_{\text{ext}}^{\text{max}} - F_{\text{ext}})/(\gamma L)$, with a stall force of $F_{\text{ext}}^{\text{max}} = 11.8\,\text{pN}$ corresponding to a stall pressure of about 100 bar. Since P_{el} is within numerical accuracy independent of F_{ext} (see Appendix C.8), the efficiency follows to be approximately parabolic with a maximal value of about $\eta = 0.8\,\%$ at $F_{\text{ext}} = 6\,\text{pN}$, see Figure 5.6 B. For electrokinetic power generation in nano channels efficiencies of the same order have been reported experimentally[174].

5.8 Summary & Conclusions

Nanoscopic fluidic devices for filter or sensor applications require suitable flow actuators. We propose a novel mechanism to use CNTs as water pumps based on time-varying and phase-shifted electric fields, in our explicit simulations generated by oscillating point charges. By comparison with an analytic theory, the pumping is shown to be due to a polarization-dragging-mechanism. Fabrication of carbon nanotubes has almost become a routine process[22, 24, 175], and application of AC electric fields in the GHz range at nanometer scales is also possible[176]. Our nanopump design works for a wide range of electrode positions (as shown by the long tube expansion in section 5.5), so the experimental realization seems possible. Even for conducting CNTs, the transverse (static) relative dielectric constant is around 10[177], allowing sufficient passage of electric fields

for our pump to work. Other non-conducting materials such as boron-nitride tubes[178] represent a possible alternative material. Our setup is a simple prototype for a nanofluidic pump without mechanical parts and represents a promising base for future devices such as nanoscale filtration systems.

Chapter 6

Conclusions and Outlook

In this thesis dielectric effects of aqueous solutions are studied by molecular dynamics simulations. The dielectric susceptibility is calculated from equilibrium simulation trajectories of various solutions using different decompositions in the chapters two to four. The simulation spectra of aqueous sodium chloride of four different concentrations and sodium-fluoride, sodium-bromide and soidum-iodide solutions of one molar concentration are successfully compared to robust experimental results from the Buchner group in chapter two. The spectra are blue-shifted and the static dielectric susceptibility decreases with increasing salt concentration and for larger anion size. While the dielectric spectrum of pure water is single Debye like, the response becomes broader in frequency space with increasing salt concentration. From the good agreement between the experimental and simulated dielectric spectra we conclude that the halide force fields that were optimized based on thermodynamic properties[82] reproduce the ion specific dielectric effects quite well, this is in particular noteworthy for the dielectric relaxation time, which comes out naturally in good agreement with experimental data. The two force fields used for iodide, denoted by NaI(4) and NaI(1), were found to be of equal quality in previous ion force-field optimization studies[82]. This degeneracy of the two iodide force fields is lifted by the comparison of the simulated and experimental dielectric constants ϵ_{CC} and relaxation times τ_{CC} in the insets of Figures 2.3 B and D. This shows that dielectric properties can be used succesfully to optimize ionic force fields.

Due to improved simulation statistics and the correct treatment of the ion-water cross-correlation polarization term we show that this term is negative and considerably suppresses the total dielectric response. We also analyze the ion polarization auto-correlation contribution and show that it contributes only about one percent to the static dielectric constant for a one molar NaCl solution. The decomposition of the dominant water polarization contribution into different solvation shells demonstrates that the first solvation shell shows the strongest ionic influence and is predominantly responsible for the blue shift and the dielectric decrement of the total dielectric spectra. By a further decomposition of the first water solvation shell into different ion-pair states we show that the static conductance of contact ion pairs is more than $50\,\%$ lower than for the other ion pairs, this partly explains the reduced conductance of concentrated salt solutions.

Our spectral decomposition suggests that the non-Debye-like character of salt solution spectra is not due to the superposition of different elementary (single Debye) relaxation processes with different relaxation times but rather an inherent spectral signature of the first solvation shell of

water around ions. It would be interesting to investigate whether a different decomposition of the dielectric contribution from the first solvation shell into separate Debye processes is possible.

A decomposition of the dominant water spectra into the self relaxation of single dipoles and the collective relaxation between different water molecules is done in chapter three. The collective signal exceeds the self contribution by a factor of three for pure bulk water and is blueshifted with increasing salt concentration as observed in dielectric relaxation spectroscopy measurements and our simulations. In contrast, the self relaxation of water is retarded in the vicinity of ions, as verified by two-dimensional infrared vibrational echo spectroscopy experiments of aqueous solutions of sodium bromide. Our decomposition resolves this puzzle and confirms both experimental trends.

Although our simulations reproduce the experimental trends of the static dielectric constant and the dynamics well, the absolute values are offset with respect to experiments due to an inaccuracy of the SPC/E water model. If new polarizable or non-polarizable water models with a dielectric spectrum closer to the experimental results become available in the future, it would be worth to redo the present simulations using an improved water model. Unfortunately, for this the ionic force fields would have to be optimized again. The method of the various decompositions applied here for sodium-halide can be transferred to other solutions. For instance, the slow processes appearing in dielectric relaxation spectroscopy measurements of aqueous sulfate solutions[57, 58] would be an interesting target for further simulations. Unfortunately, the currently available sulfate force fields are not very accurate and require further optimization[179].

The dielectric spectra of eight residue alanine solvated in water are presented in chapter four. Via a projection into folded and unfolded peptide configurations we study the spectral impact of the secondary structure. In addition to the bulk water resonance, a second peak appears in the sub-GHz range. Our spectral decomposition shows that this peak is mainly caused by the auto-correlation of the peptide polarization and is much stronger, if the peptide is folded. At nearly the same relaxation time we find a slow process in the collective hydration water response, which is more pronounced for a folded peptide. The self relaxation of the hydration water is only weakly retarded and shows that the peptide is not able to fix the orientation of single water molecules over times much longer than the bulk water relaxation time. The existence of slow collective processes inside the hydration shell might be related to the controversially discussed picture of "slaving water" around proteins, where solvent fluctuations control protein dynamics via activation enthalpy[12, 165]. With improved computational resources in the future, it would be meaningful to redo similar simulations with much larger peptides and therefore a much slower peptide relaxation time in order to find out whether the slow collective processes in the hydration shell water will adapt the slower peptide time-scale. If the adaption is not observed, the slow collective interactions in the hydration shell might be distinguished from the peptide processes and found to be the experimentally observed δ-dispersion at intermediate time-scale[145, 146]. Experimental spectroscopic measurements for eight residue alanine or similar-sized peptides are desirable for comparison to our simulation results.

We show in chapter five that the relatively strong dielectric response of water to an external electric field can be used to pump pure water with AC electric fields. Nano-fluidic systems require driving mechanisms different from the conventional macroscopic methods, which are based on relatively weak pressure gradients and mechanical parts. Our novel mechanism uses time-varying and phase-shifted electric fields in the GHz range. The specific design, which is studied in this

thesis, consists of two oscillating point charges next to a carbon nanotube filled with water. Several setup parameters are varied. The results are in good agreement with the analytic polarization-dragging-mechanism, derived in this thesis. The manufacturing and use of carbon nanotubes is established[22, 24, 175], and implementation of AC electric fields in the GHz range at nanometer scales is also possible[176]. Since our mechanism is applicable over a wide range of electrode positions, future experimental realization seems possible. Our setup is a simple prototype for a nanofluidic pump without mechanical parts and represents a promising base for future devices in nano-fluidic systems.

Appendix A

Fluctuation Dissipation Theorem

This derivation of the fluctuation dissipation is close to Kohler's derivation[106].

We write the Hamiltonian $H = H_0 + H'$ as sum of an equilibrium Hamiltonian H_0 and an interaction Hamiltonian H' due to a perturbing force $F(t)$:

$$H'(t) = -AF(t), \tag{A.1}$$

with a coupling parameter A which can be time, special and momentum dependent.

The expectation value of an observable $B(t)$ is related to the history of the forces up to the time t by an after effect function $\phi_{BA}(\tau)$:

$$\langle B(t) \rangle = \int_{-\infty}^{t} \phi_{BA}(t-t')F(t')\mathrm{d}t' \tag{A.2}$$

Using the variable transformation $\tau = t - t'$ in the first and the convolution theorem in the second step we can rewrite the expression as

$$\langle B(t) \rangle = \int_{0}^{\infty} \phi_{BA}(\tau)F(t-\tau)\mathrm{d}\tau \tag{A.3}$$

$$= \int_{-\infty}^{\infty} \tilde{F}(\omega)e^{i\omega t} \int_{0}^{\infty} \phi_{BA}(\tau)e^{-i\omega\tau}\mathrm{d}\tau\mathrm{d}\omega, \tag{A.4}$$

where $\tilde{F}(\omega) = \frac{1}{2\pi}\int_{-\infty}^{\infty} F(t)e^{-i\omega t}\mathrm{d}t$ is the Fourier transform of F. The Fourier transforms of B and F be related by the generalized susceptibility $\chi_{BA}(\omega)$:

$$\langle \tilde{B}(\omega) \rangle = \tilde{F}(\omega)\chi_{BA}(\omega) \tag{A.5}$$

$$\chi_{BA}(\omega) = \int_{0}^{\infty} \phi_{BA}(\tau)e^{-i\omega\tau}\mathrm{d}\tau. \tag{A.6}$$

The Liouville equation describes the time evolution of the N-particle distribution function $f^{(N)}(\vec{r}^N, \vec{p}^N) = f_0^{(N)}(\vec{r}^N, \vec{p}^N) + f_1^{(N)}(\vec{r}^N, \vec{p}^N)$, where $f_0^{(N)}$ denotes the equilibrium distribution:

$$\frac{\partial f_1^{(N)}}{\partial t} = \frac{\partial f_1^{(N)}}{\partial t} + \frac{\partial f_0^{(N)}}{\partial t} = \frac{\partial f^{(N)}}{\partial t} \tag{A.7}$$

$$= -\sum_{k=1}^{N} \left[\nabla_p H \cdot \nabla_r (f_0^{(N)} + f_1^{(N)}) - \nabla_r H \cdot \nabla_p (f_0^{(N)} + f_1^{(N)}) \right] \tag{A.8}$$

$$= -\sum_{k=1}^{N} \left[\nabla_p (H_0 + H') \cdot \nabla_r (f_0^{(N)} + f_1^{(N)}) - \nabla_r (H_0 + H') \cdot \nabla_p (f_0^{(N)} + f_1^{(N)}) \right] \tag{A.9}$$

By neglecting products of H' and $f_1^{(N)}$ we obtain:

$$\frac{\partial f_1^{(N)}}{\partial t} = -\sum_{k=1}^{N} \left[\nabla_p H_0 \cdot \nabla_r f_1^{(N)} - \nabla_r H_0 \cdot \nabla_p f_1^{(N)} \right] - \frac{f_0^{(N)}}{k_B T} \sum_{k=1}^{N} \left[\nabla_p H_0 \cdot \nabla_r H' - \nabla_r H_0 \cdot \nabla_p H' \right]$$

$$= -\sum_{k=1}^{N} \left[\nabla_p H_0 \cdot \nabla_r f_1^{(N)} - \nabla_r H_0 \cdot \nabla_p f_1^{(N)} \right] - \frac{V f_0^{(N)}}{k_B T} F(t) \dot{A}_0, \tag{A.10}$$

where we have used the fact that H' only depends on r or p via the coupling parameter A. The notation $\dot{A}_0$ indicates that the unperturbed Hamiltonian H_0 is used in the Liouville equation. An integration leads to

$$f_1^{(N)}(t) = \frac{V f_0^{(N)}}{k_B T} \int_{-\infty}^{t} F(t') e^{-i(t'-t)L_0} \dot{A}_0 dt, \tag{A.11}$$

where $L_0 = i \sum_k (\nabla_p H_0 \nabla_r - \nabla_r H_0 \nabla_p)$ is the Liouville operator propagating the system in time.

Knowing the time evolution of the N-particle system allows us to calculate the expectation value of an observable B:

$$\langle B(t) \rangle = \int B(0) f_1^{(N)}(t) dr^{(N)} dp^{(N)} \tag{A.12}$$

$$= \frac{V}{k_B T} \int_{-\infty}^{t} F(t') \int f_0^{(N)} B(0) e^{-i(t'-t)L_0} \dot{A}_0 dr^{(N)} dp^{(N)} dt. \tag{A.13}$$

By comparison with equation A.3 we express the after effect function as

$$\phi(t - t') = \frac{V}{k_B T} \int f_0^{(N)} B(0) e^{-i(t'-t)L_0} \dot{A}_0 dr^{(N)} dp^{(N)} \tag{A.14}$$

$$= \frac{V}{k_B T} \langle B(0) \dot{A}(t' - t) \rangle = \frac{V}{k_B T} \langle B(t - t') \dot{A}(0) \rangle. \tag{A.15}$$

The generalized susceptibility reads now:

$$\langle \tilde{B}(\omega) \rangle = \int_0^{\infty} \langle B(t) \dot{A}(0) \rangle e^{-i\omega t} dt. \tag{A.16}$$

For the coupling parameter and observable being equal to the polarization density $A = B = \vec{P}/V$, we can obtain now the expression for susceptibility in three dimensions, which allows to calculate

dielectric spectra from equilibrium fluctuations of the polarization as

$$\epsilon_0 \chi(f) = -\frac{1}{3V k_B T} \int_0^\infty e^{-2\pi i f t} \langle \vec{P}(0) \dot{\vec{P}}(t) \rangle \mathrm{d}t. \tag{A.17}$$

Appendix B

Appendix to Sodium-Halide Spectra

This part of the Appendix provides additional information to the chapters 2 & 3: The integration procedure of and fits to the correlation functions, the life time of contact ion pairs, further tests of the Madden-Kivelson equation, second Legendre polynomials of the dipole and the hydrogen-hydrogen vector of water in a 1 M NaCl soultions, a discussion of theromstat and barostat effects and a further comparison of experimental and simulation results.

B.1 Integration of the Correlation Functions

The water polarization auto-correlation function $\phi_{\rm W}(t)$, the ion current auto-correlation function $\phi_{\rm I}(t)$ and the cross-correlation function between the ion current and water polarization $\phi_{\rm IW}(t)$ are obtained using fast Fourier-transformation techniques. Since all correlation functions decrease with time they drop below the noise level at finite time, it is therefore useful to use an integration cutoff during calculation of the spectra via Laplace transformation. In the following the choice of the cutoff-time $T_{\rm cut}$ for the different correlation functions is discussed.

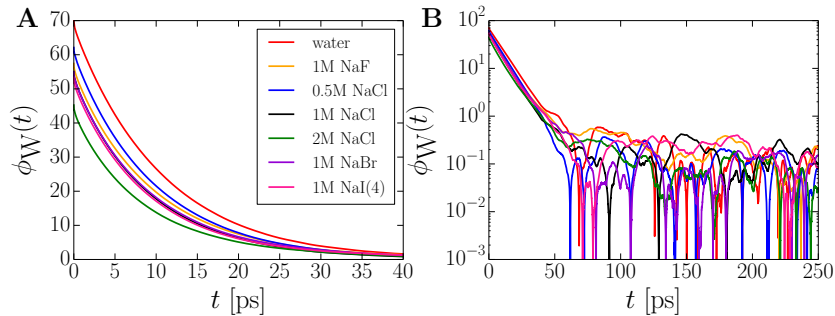### B.1.1 Water Polarization Auto-Correlation

FIGURE B.1: Auto-correlation function $\phi_{\rm W}(t)$ of the water polarization. For all studied salt solutions the data is strictly positive up to about 50 ps.

The water polarization auto-correlation function $\phi_{\rm W}(t)$ is most relevant for the computation of the dielectric spectra. Because of noise, $\phi_{\rm W}(t)$ drops below zero between 50 and 200 ps for all

studied solutions, as demonstrated in Figure B.1. Therefore, we integrate $\phi_W(t)$ only up to the time threshold where it first drops below zero.

B.1.2   Ion-Water Cross-Correlation Function

The ion-water cross-correlation function $\phi_{IW}(t)$ is zero at $t = 0$, reaches a maximum after about 0.2 ps and then drops to zero within about 20 ps. Similar to $\phi_W(t)$ we integrate $\phi_{IW}(t)$ up to the time threshold where it first drops below zero.
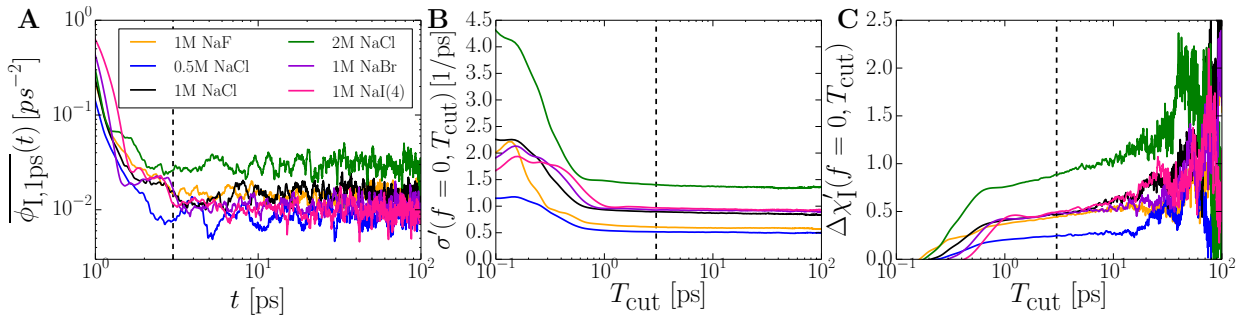
B.1.3   Ion Current Auto-Correlation

FIGURE B.2: (A) The running average over a time window of $T = 1\,\mathrm{ps}$ of the absolute value of the ion polarization autocorrelation function $\phi_I(t)$ levels off at around $t = 3\,\mathrm{ps}$. (B) The static conductivity $\sigma'(f = 0, T_{cut})$ shows only weak dependence on the integration cutoff time T_{cut}. (C) The ion-polarization contribution to the static dielectric constant, $\Delta\chi'_I(f = 0, T_{cut})$ exhibits considerable dependence on the integration cutoff time T_{cut}.

Since the ion current auto-correlation function $\phi_I(t)$ oscillates, we can not use the first drop below zero to determine a cutoff time. We denote the running average of $\phi_I(t)$ over a time window T by

$$\overline{\phi_{I,\,T}}(t) \quad = \quad \int_{t-0.5T}^{t+0.5T} |\phi_I(t')| \frac{\mathrm{d}t'}{T} \tag{B.1}$$

Figure B.2 A shows that the T=1 ps average of $\phi_I(t)$ only decreases until about 3 ps beyond which it levels off because of noise. Therefore, we choose a cutoff of $T_{cut} = 3\,\mathrm{ps}$ to limit the influence of noise on the dielectric spectra. To check the influence of the chosen cutoff we calculate the ionic contribution to the static conductivity $\sigma'_I(f = 0, T_{cut})$ and to the static dielectric constant $\Delta\chi'_I(f = 0, T_{cut})$ as a function of the integration cutoff T_{cut}, the results are shown in Figures B.2 B and C. The cutoff is not critical for the conductivity $\sigma'_I(f = 0)$, because only the short-time behavior of $\phi_I(t)$ is relevant, the results for $\Delta\chi'_I(f = 0)$ more sensitively depend on the cutoff parameter and become noisy for larger cutoff values. To investigate the cutoff effects on $\Delta\chi'_I$ further, we in Figure B.3 show the spectral function for various cutoffs. For the larger cutoff values low-frequency features appear which cannot easily be distinguished from noise. Therefore, we have to acknowledge that low-frequency ionic processes can not be ruled out based on our simulation data, since the auto-correlation function $\phi_I(t)$ is only statistically robust for the first ps. This is no problem for the total dielectric spectra, since the ion polarization autocorrelation only contributes negligibly, but for the complete understanding of low-frequency ionic polarization effects much longer simulations would be necessary.
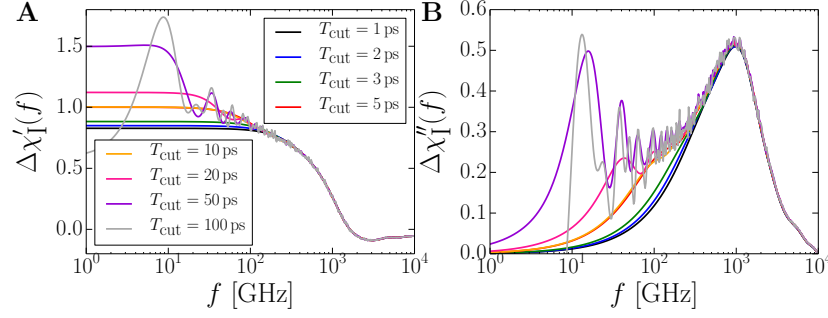
FIGURE B.3: The ion-polarization contribution to the dielectric spectrum $\Delta\chi_{\mathrm{I}}(f)$ for $2\,\mathrm{M}$ NaCl is shown for various integration cutoff times T_{cut}. For larger cutoff times the spectrum exhibits additional features in the low-frequency range.

B.2 Contact Ion Pair Lifetime

In Figure B.4 A we present a typical time evolution of the distance $r_{\mathrm{Na,Cl}}(t)$ between a sodium ion in 1M NaCl solution and the closest chloride ion (black line). According to our definition in section **??** contact ion pairs are pairs with distance r smaller than the threshold $r_{\mathrm{CIP}} = 0.374\,\mathrm{nm}$ (dashed blue line). If t_0 and $t_1 > t_0$ are times with $r(t_0) = r(t_1) = r_{\mathrm{CIP}}$ and $r(t) \leq r_{\mathrm{CIP}}$ for all $t \in [t_0, t_1]$, the CIP lifetime is defined as the difference $t_1 - t_0$. In order to exclude jumps around the threshold we only include strongly bound pairs where at least once in the range $[t_0, t_1]$ the distance is below $r_0 = 0.289\,\mathrm{nm}$ (dashed green line), where r_0 is the position of the maximum of the radial distribution function $g(r_{\mathrm{Na,Cl}})$ (shown in Figure 2.1 C). So the CIP lifetime can be expressed as:

$$t_{\mathrm{CIP}} = (t_1 - t_0 | t_1 > t_0, r(t_0) = r(t_1) = r_{\mathrm{CIP}},$$
$$r(t) \leq r_{\mathrm{CIP}} \forall t \in [t_0, t_1], \min(r(t) | t \in [t_0, t_1]) < r_0)$$

The probability distribution of t_{CIP} is shown in Figure B.4 B and has an average value of $12.3\,\mathrm{ps}$ (red line).
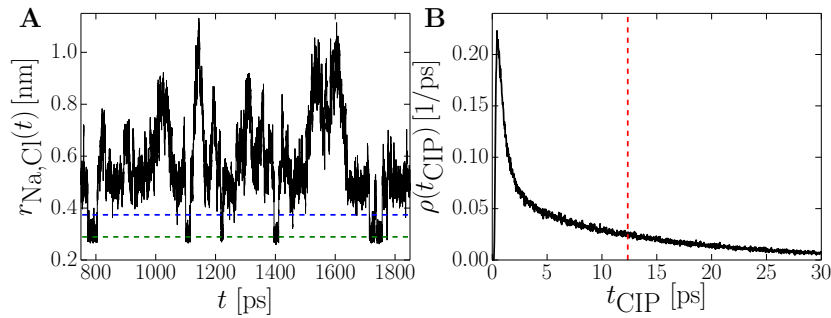

FIGURE B.4: (A) Trajectory of the distance $r_{\mathrm{Na,Cl}}(t)$ between a sodium ion in 1M NaCl solution and the closest chloride ion (black line). The dashed blue line is the threshold between CIP and SIP and the dashed green line shows the position of the maximum of the radial distribution function $g(r_{\mathrm{Na,Cl}})$. (B) Probability distribution of the CIP lifetime t_{CIP}.

Since the mean lifetime of ion pairs is of the order of the relaxation time of water, it is clear that sodium-halide ion pairs are difficult to probe based on dielectric spectroscopy.

B.3 Fits to Correlation Functions

In Figure ?? A-C we show double Debye fits of the form $\phi(t)/\phi(0) = A_1 \exp(-t/\tau_1) + A_2 \exp(-t/\tau_2)$ to the normalized polarization correlation functions of the different water components of 1M NaCl and pure water on the log-lin scale in the range between 0 and 25 ps. In Tables B.1-B.3 we list the fit parameters:

self term	A_1	A_2	τ_1 [ps]	τ_2 [ps]
1 M NaCl: W1+	0.364	0.541	13.400	3.496
1 M NaCl: W1-	0.285	0.619	11.972	3.841
1 M NaCl: W2	0.259	0.643	11.910	3.846
1 M NaCl: W3	0.232	0.670	11.289	3.909
1 M NaCl: W	0.263	0.640	11.963	3.836
pure water	0.738	0.000	6.346	-

TABLE B.1: Double Debye fit parameters to the self correlation function of different water components shown in Figure ?? A-C.

The fits to the self term lead to a fast relaxation of about 4 ps and a slow one of about 12 ps. The large difference between the two relaxation times makes it obvious that a single Debye fit would be insufficient. Only for pure water our two-exponential fit converges to a single Debye fit, since $A_2 = 0$.

collective term	A_1	A_2	τ_1 [ps]	τ_2 [ps]
1 M NaCl: W1-	0.935	0.195	9.584	9.584
1 M NaCl: W2	1.062	0.000	9.468	-
1 M NaCl: W3	1.043	0.000	10.879	-
1 M NaCl: W	1.028	0.000	10.175	-
pure water	1.086	0.000	11.528	-

TABLE B.2: Double Debye fit parameters to the collective correlation function of different water components shown in Figure ?? B. Note that for the water solvation shell next to sodium (W1+) no fit is performed, since this function vanishes quickly.

The fits to the collective correlation in Table B.2 indicate that except for W1- a single Debye fit in the time domain is sufficient.

both terms	A_1	A_2	τ_1 [ps]	τ_2 [ps]
1 M NaCl: W1+	0.853	0.123	7.169	0.268
1 M NaCl: W1-	0.944	0.042	9.018	0.109
1 M NaCl: W2	0.962	0.030	9.000	0.388
1 M NaCl: W3	0.492	0.491	12.541	7.506
1 M NaCl: W	0.921	0.056	9.542	1.643
pure water	0.980	0.020	10.685	0.017

TABLE B.3: Double Debye fit parameters to the total correlation function of different water components shown in in Figure ?? C

Among the fits to the total correlation in Table B.3, water next to sodium (W1+) has the fastest relaxation time τ_1.

B.4 Test of the Madden-Kivelson Equation

In Figure ?? A the static dielectric constant per molecule and the relaxation time of second and third solvation shell water of 1M NaCl as well as of pure water lie on a straight line in a correlation plot. For first solvation shell water, water next to sodium and chloride we also obtain a linear relation between these two observables but with a different prefactor compared to the outer shell water. In Figure B.5 we show an analogous plot for 1M NaF (A), 1M NaBr (B) and 1M NaI (C). The slope of the fitting line for the first solvation shell increases with increasing anion size, according to the Madden-Kivelson equation this indicates that the self relaxation time for first solvation shell water approaches the value of pure water for the larger anions. This is indeed confirmed in Figure ?? A, where the self relaxation time is shown to decrease from fluoride to iodide.
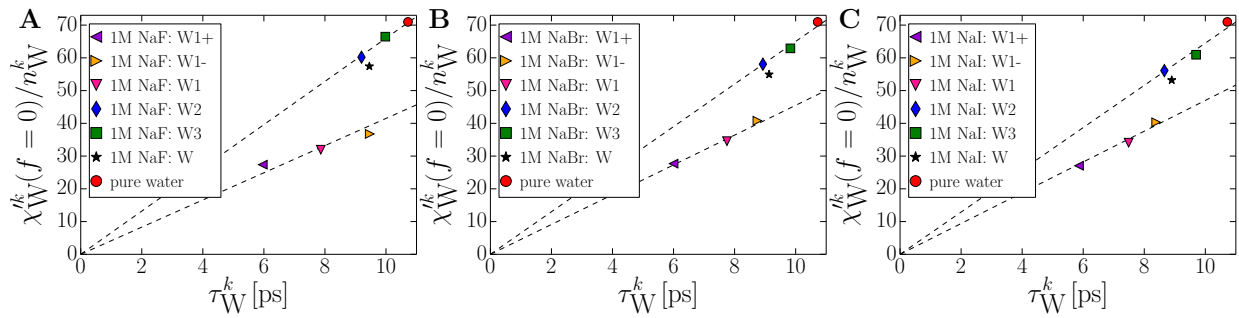

FIGURE B.5: Plot of the static dielectric contribution per water molecule $\chi_W^k(f=0)/n_W^k$ versus the Cole-Cole relaxation time τ_W^k for the different water solvation shells of 1 M NaF (A), NaBr (B) and NaI (C), the result for pure water is indicated by a red circle. The broken lines are fitted separately to pure water, second (W2) and third solvation shell (W3) results and to the first solvation shell results.

In Figure B.6 we plot the various quantities that appear in the Madden-Kivelson equation for the different water solvation shells in a 1 M solution of NaF, NaBr and NaI, while the same plot for NaCl is already shown in chapter 3. The black spheres denote the Kirkwood factor g_K, which in the first solvation shell is considerably smaller than in the second or third solvation shell. The Kirkwood factor of water in the first shell increases with increasing anion size. This shows that the presence of a small anion almost completely destroys the cooperative water structure that leads to the large value of $g_K \simeq 2.5$ in pure bulk water, which we determined in separate simulations. Accordingly, fluoride can be called a very efficient dielectric structure breaker.

B.5 Second Legendre polynomial results for dipole and hydrogen-hydrogen vector correlations

In Figure ?? our results for the second Legendre polynomial $P_2(x) = (3x^2 - 1)/2$ of the OH-bond vector correlation are presented. Although the second Legendre polynomial of the time-correlation of the normalized dipole vector $\vec{u}_D$ and the hydrogen-hydrogen vector $\vec{u}_{HH}$ are accessible from simulations, they are typically not shown since they are not accessible experimentally.

In Figure B.7 A we show P_2 of the correlation of the normalized dipole vector $\vec{u}_D$ for the different water components of 1M NaCl and pure water from our simulations (solid lines) and double Debye
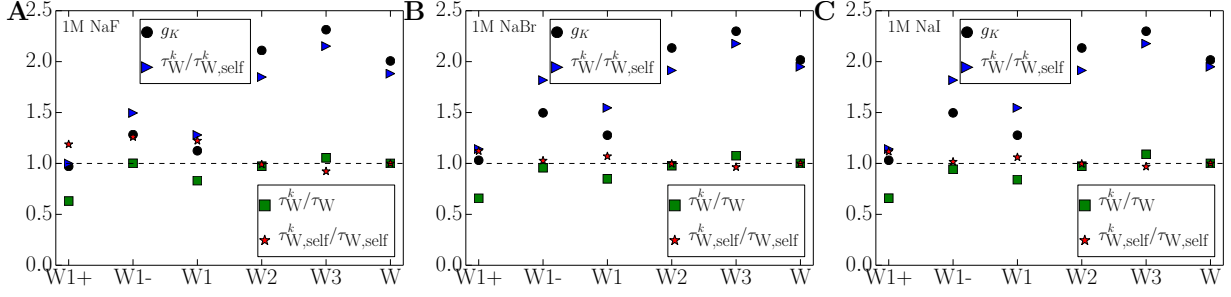
FIGURE B.6: Plot of the Kirkwood factor $g_K = (2\epsilon + 1)\chi_W'^k(f = 0)/(3\epsilon\chi_{W,self}'^k(f = 0))$ (black circles), the ratio of the dielectric water relaxation time and the single water relaxation time $\tau_W^k/\tau_{W,self}^k$ (blue triangles), the rescaled dielectric relaxation time τ_W^k/τ_W (green squares) and the rescaled single-water relaxation time $\tau_{W,self}^k/\tau_{W,self}$ (red stars) for different water solvation shells in 1 M NaF (A), 1 M NaBr (B) and 1 M NaI (C). τ_W^k is normalized with respect to the dielectric relaxation time of the entire water ensemble τ_W and $\tau_{W,self}^k$ is normalized with respect to the single-water relaxation time of the entire water ensemble $\tau_{W,self}$.

fits (dashed lines). While the results for bulk water (red line) decrease in a single exponential way and faster than water in the ionic solutions, P_2 decreases slower going from outer shell water (W3) to water in the vicinity of sodium (W1). Similarly to our findings for the OH-vector, a fast decay by about 20 % is observed within the first 200 fs which is independent of the presence of the ions, this is more clearly demonstrated in Figure B.7 B where pure water results and the data for all water solvation shells in 1 M NaCl are shown to exhibit identical decay at short times (all solid lines superimpose perfectly). Our results in Figure B.7 C demonstrate that the slowing down of the dipole vector relaxation is more pronounced than for the OH-bond, for which the slower relaxation time increases by only about 2 ps (compare Figure **??** C).
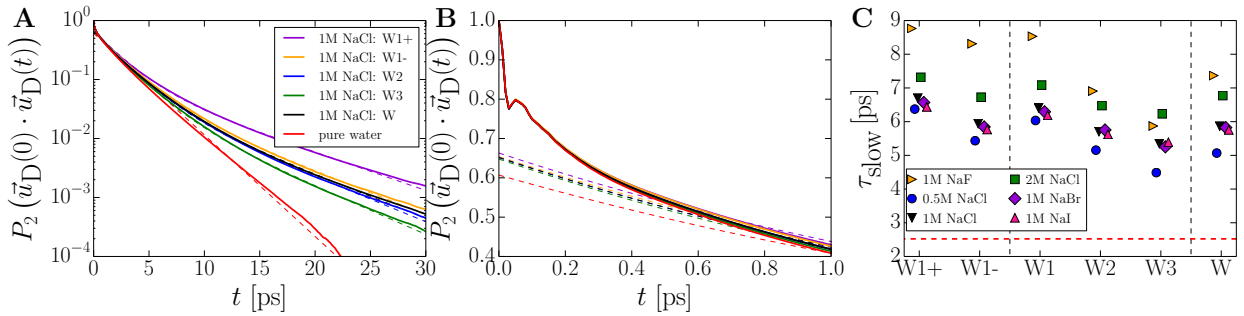

FIGURE B.7: (A) Results for the second Legendre polynomial of the water dipole vector auto-correlation function for different solvation shells in 1 M NaCl, solid lines are simulation data and broken lines are double Debye fits in the range $[0.2, 25\,\text{ps}]$. Results for pure bulk water are denoted by red lines. The short-time behavior is shown in (B). (C) Slower relaxation time τ^{slow} of the double Debye fits in A for all different salt solutions and concentrations, sorted according to the different solvation shells. All relaxation times are slower than the pure water value (denoted by a horizontal red dashed line).

Finally, we present in Figure B.8 the second Legendre polynomial for the time-correlation of the normalized hydrogen-hydrogen vector $\vec{u}_{HH}$. The short time as well as the long time evolution are similar to the findings for the dipole vector. The slower relaxation times in Figure B.8 C are about one ps slower than the corresponding relaxation times for the dipole vector in Figure B.7 C.

Summarizing this section, the ion-specific trends and the effects seen in the inner solvation shell are analogous for the three studied molecular vectors which indicates that the rotation of single water molecules is slowed down by ions almost independent of the axis of rotation.
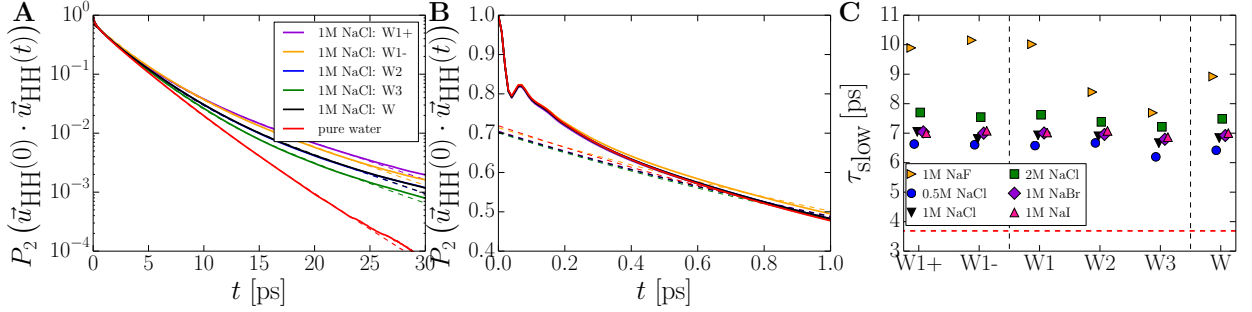

FIGURE B.8: (A) Results for the second Legendre polynomial of the water HH vector auto-correlation function for different solvation shells in $1\,\mathrm{M}$ NaCl, solid lines are simulation data and broken lines are double Debye fits in the range $[0.2, 25\,\mathrm{ps}]$. Results for pure bulk water are denoted by red lines. The short-time behavior is shown in (B). (C) Slower relaxation time τ^{slow} of the double Debye fits in A for all different salt solutions and concentrations, sorted according to the different solvation shells. All relaxation times are slower than the pure water value (denoted by a horizontal red dashed line).

B.6 Discussion of Thermostat and Barostat Parameters

The simulation systems are coupled to a Nose-Hoover thermostat with coupling time $\tau_{\mathrm{T}} = 1\,\mathrm{ps}$ and a Parrinello-Rahman barostat with atmospheric pressure with a coupling time of $\tau_{\mathrm{P}} = 1\,\mathrm{ps}$. In order to check if the water dynamics distinctly depends on the coupling times, we performed a NPT simulation with larger temperature coupling time of $10\,\mathrm{ps}$ and NVT simulations with temperature coupling times of 1 and $10\,\mathrm{ps}$ for $1\,\mathrm{M}$ NaCl. A comparison of the water polarization auto-correlation functions is presented in Figure B.9 A. Only at longer times the results differ slightly due to noise. These difference do only influence the spectra very weakly, as can be seen in Figures B.9 B and C. Therefore, our choice of an NPT ensemble with a temperature coupling time $\tau_{\mathrm{T}} = 1\,\mathrm{ps}$ is robust against possible barostat and thermostat artifacts.
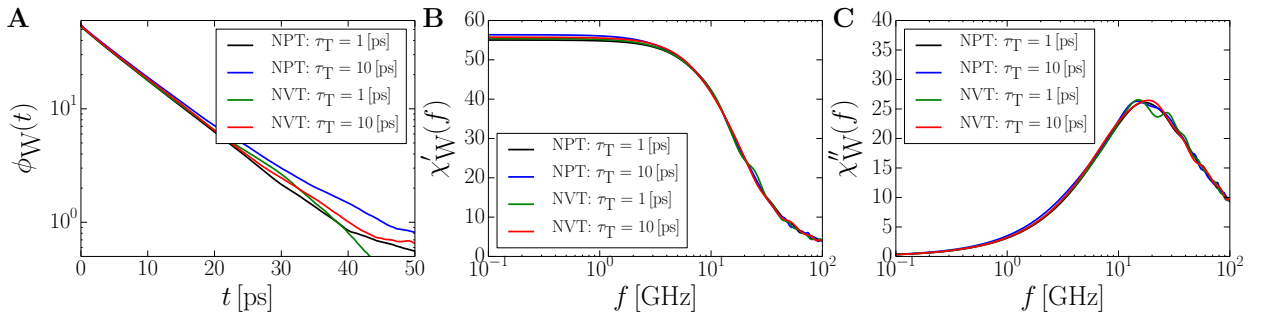

FIGURE B.9: Comparison of the water polarization auto-correlation (A) and the water contribution to the dielectric spectra (B & C) for various coupling parameters: The black and the blue lines denote NPT simulation with temperature coupling times of 1 and $10\,\mathrm{ps}$, while the green and red lines a NVT simulations with temperature coupling times of 1 and $10\,\mathrm{ps}$.

As an additional validation of our ionic force fields, we calculated solution densities in the NPT ensemble. The densities of all studied solutions are in good agreement with experimental densities, as shown in Table B.4.

	ρ_{sim} [kg/l]	ρ_{exp} [kg/l]
water	0.998	0.998
1 M NaF	1.051	1.04
0.5 M NaCl	1.013	1.019
1 M NaCl	1.031	1.038
2 M NaCl	1.066	1.074
1 M NaBr	1.066	1.075
1 M NaI	1.092	1.10

TABLE B.4: Comparison of densities from simulation and experiments for the studied solutions.

B.7   Experimental vs. Simulation Spectra

In Figure B.10 we directly compare dielectric spectra of water and sodium chloride solutions from our simulations (solid lines) with experiments from Buchner's group (symbols). The static dielectric constant is shifted down by 10-15 in simulations compared to experimental data. Since this shift occurs also for pure water, we assign this deviation to the SPC/E water force field. Likewise, the relaxation times in simulations are red-shifted compared to experiments. As a consequence, the comparison of ion-specific and concentration-dependent trends is easier when comparing fit values for the dielectric constants and dielectric relaxation times, as done in chapter 3.
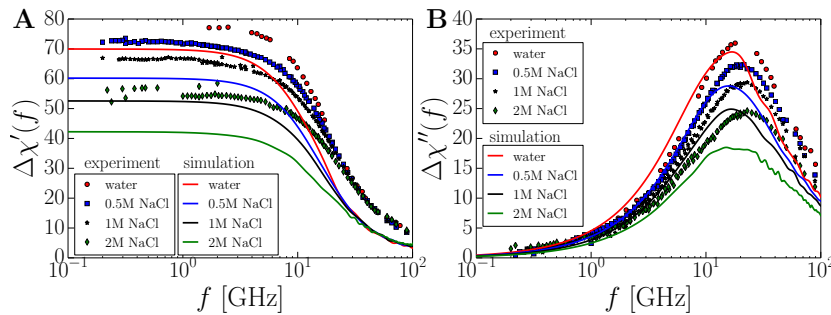

FIGURE B.10: Comparison of the real (A) and imaginary part (B) of the dielectric spectra for water and NaCl solutions between experiments (symbols) and simulations (solid lines).

Appendix C

Appendix to Nanoscale Pumping of water by AC Electric Fields

In this part of the Appendix simulation results for varying electrode geometries are presented. Furthermore, details on the simulation methods and parameters used in simulations to chapter 5 are given.
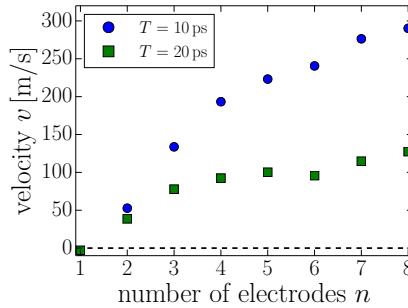
C.1   Varying the Number of Electrodes

FIGURE C.1: Flow speed v as a function of the number of electrodes n. For the spatially periodic ($n = 8$) system the flow speed doubles when the oscillation periodicity is changed from $T = 20\,\mathrm{ps}$ to $T = 10\,\mathrm{ps}$, in line with the maximal possible pumping speed given by the phase velocity. (All data for $q = 1\,e$, $\varphi = \pi/2$, $\delta = 0.5\,\mathrm{nm}$, $d = 1.07\,\mathrm{nm}$ and $L = 8.5\,\mathrm{nm}$.)

Here we systematically vary the number of electrodes n for a given system, leaving all other parameters fixed. As might be expected, we find that the flow increases with increasing n, see Figure C.1. In the limit of strong electric fields we expect the pumping velocity to be proportional to the phase velocity v_{phase} defined in equation 5.76. Indeed, for $n = 8$ we see in Figure C.1 that the pumping speed doubles when the oscillation period is reduced from $20\,\mathrm{ps}$ (green dots) to $10\,\mathrm{ps}$ (blue dots).

C.2 Possible Influence of the Electrode Position Relative to the CNT Lattice

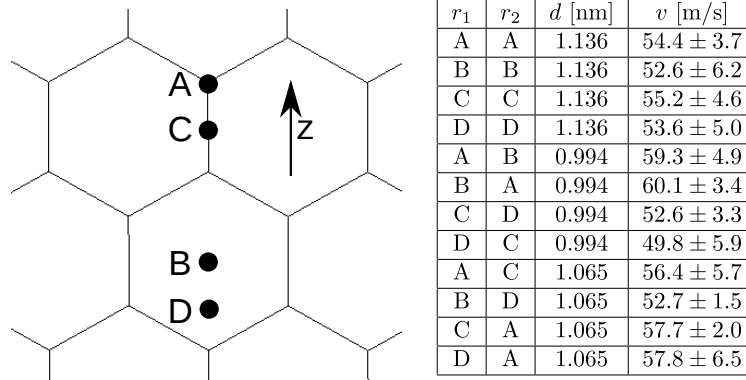| r_1	r_2	d [nm]	v [m/s]
A	A	1.136	54.4 ± 3.7
B	B	1.136	52.6 ± 6.2
C	C	1.136	55.2 ± 4.6
D	D	1.136	53.6 ± 5.0
A	B	0.994	59.3 ± 4.9
B	A	0.994	60.1 ± 3.4
C	D	0.994	52.6 ± 3.3
D	C	0.994	49.8 ± 5.9
A	C	1.065	56.4 ± 5.7
B	D	1.065	52.7 ± 1.5
C	A	1.065	57.7 ± 2.0
D	A	1.065	57.8 ± 6.5

FIGURE C.2: The dependence of the pumping velocity v on the electrode position relative to the honeycomb lattice formed by the CNT atoms is weak. The combination (B,D) is equal to the positioning of two electrodes as studied in chapter 5. (Data for $n = 2$, $T = 10\,\mathrm{ps}$, $q = 1\,e$, $\varphi = \pi/2$, $\delta = 0.5\,\mathrm{nm}$ and $L = 8.5\,\mathrm{nm}$.)

Next, we investigate the influence of the electrode positions relative to the honeycomb lattice of carbon atoms composing the CNT wall, as illustrated in Figure C.2. We simulate the two electrode system, $n = 2$, for various electrode positions relative to the lattice of carbon atoms. The results which are displayed in Figure C.2 only show a weak dependence of the velocity on various combinations of lattice positions. Thus, the effect of the electrode position relative to the CNT lattice can be neglected.

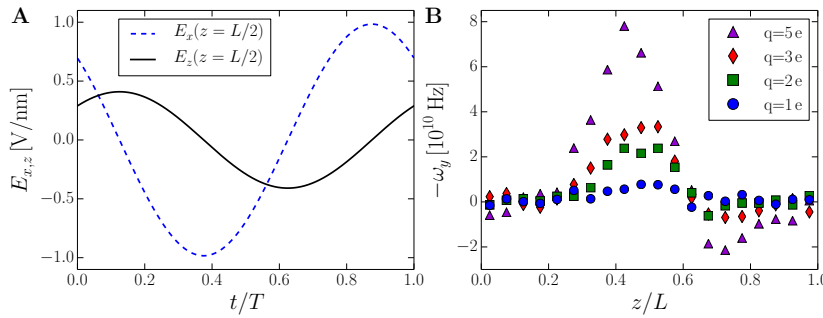## C.3 Rotation-Translation-Coupling Contribution

FIGURE C.3: (A) The x and z-components of the electric field at $z = L/2$ on the tube axis oscillate as function of time with different phase and amplitude. (B) In all regions the average water rotation is much slower than the field rotation of $\omega = 2\pi/T = 2\pi \cdot 10^{11}\,\mathrm{Hz}$. For the standard charge $q = 1\,e$ we measure a rotation $|\omega_y| \simeq 5 \cdot 10^9\,\mathrm{Hz}$ nearby the electrodes. (Data for $n = 2$, $T = 10\,\mathrm{ps}$, $\varphi = \pi/2$, $\delta = 0.5\,\mathrm{nm}$, $d = 1.07\,\mathrm{nm}$ and $L = 8.5\,\mathrm{nm}$.)

Bonthuis et al.[173] have shown that in a planar channel with asymmetric surface conditions (one wall hydrophobic, the other hydrophilic), pure water can be pumped via *rotation-translation-coupling* in presence of a rotating electric field. In our tube, we effectively have similar asymmetric surface conditions due to the asymmetric positioning of the electrode charges in most of our simulations. In Figure C.3 A we demonstrate that the x and z-components of the electric field at

$z = L/2$ on the tube axis oscillate as a function of time with a phase shift of about $90°$. The amplitudes are different, so we have an elliptic rotating electric field in the center of the CNT. Therefore, one could in principle expect that the flow in our system might be caused by rotation-translation-coupling.

In order to test this possibility, we first check whether the water molecules in the CNT are rotating. To that end we measure the average dipole rotation ω_y around the y-axis with the axes as defined in Figure 5.1 A. In order to disentangle thermal from mean rotation, the dipole angle α in the x-z-plane has to be collected every timestep,

$$\alpha = \begin{cases} \arccos(\frac{p_z}{\sqrt{p_x^2 + p_z^2}}), & \text{if } p_x \geq 0 \\ 2\pi - \arccos(\frac{p_z}{\sqrt{p_x^2 + p_z^2}}), & \text{if } p_x < 0 \end{cases} \tag{C.1}$$

$$p_x = (x_{\text{H1}} + x_{\text{H2}} - 2x_{\text{O}})\, q_H \tag{C.2}$$

$$p_z = (z_{\text{H1}} + z_{\text{H2}} - 2z_{\text{O}})\, q_H, \tag{C.3}$$

where q_H is the partial charge of a hydrogen atom, x_{H1} and x_{H2} are the x coordinates of the two hydrogen atoms and x_{O} the x coordinate of the oxygen atom of one water molecule.

By comparing with the orientation at the previous timestep, we obtain the rotation

$$\omega_y(t) = \frac{\alpha(t) - \alpha(t - \delta t)}{\delta t} \in [-\frac{\pi}{\delta t}, \frac{\pi}{\delta t}]. \tag{C.4}$$

For the system with two electrodes and $q = 1\,e$, we obtain a maximal rotation of about $|\omega_y| \simeq 5 \cdot 10^9$ Hz (Figure C.3 B), which is much lower than the field oscillation of $\omega = 2\pi/T = 2\pi 10^{11}$ Hz.

The rotation-translation-coupling mechanism in cylindrical geometry is much more involved than in a planar channel. To obtain a rough estimate for the pumping due to rotation-translation-coupling, we calculate the corresponding pumping speed expected in a planar channel of height $H = 2R_{\text{eff}} = 1.24$ nm along the x-direction that would be associated with a homogeneous water rotation $|\omega_y| \simeq 5 \cdot 10^9$ Hz, which constitutes an upper bound for the pumping speed in a cylinder. Neglecting effects from the channel wall and assuming full rotation-translation coupling (see ref. [173] for further details), we obtain a linear velocity profile $v(x) = 2\omega_y\, x$ and thus the average velocity $\bar{v} = H\omega_y \simeq 6$ m/s. This estimated average velocity is one order of magnitude smaller than the measured speed of 53 m/s, so we conclude that the contribution of rotation-translation-coupling in our pump is weak. This conclusion is independently verified by the velocity that is calculated based on the polarization-dragging theory, which consistently explains the simulation results.

C.4 Alternative Polar Fluids

In our simulation study we focus on water, which is the most important polar fluid. But our polarization-dragging mechanism applies generally to all different polar fluids. In C.1 we list experimentally obtained material constants for other common polar fluids. If the refractive index n or the relative permittivity ϵ_r are known at a certain frequency, the gas phase molecular polarisibility α can be calculated by the Lorentz-Lorenz-equation or the Clausius-Mossotti-equation,

	$\mu[D]$	$V_M[\text{cm}^3]$	$\epsilon_{r,\text{static}}$	α_{static} [10^{-40} C m^2/V]	α_{vis} [10^{-40} C m^2/V]
DMSO	4.0	71.0	47	29.4	8.9
acetone	2.9	74.0	21	28.4	7.0
methanol	1.7	40.5	33	16.3	3.7
ethanol	1.7	58.4	25	22.9	6.0
water	1.9	18.1	80	7.6	1.5

TABLE C.1: Experimental data for the molecular dipole moment μ in the gas phase, the molar volume V_M and the static relative permittivity $\epsilon_{r,\text{static}}$ at room temperature of various polar fluids. The static molecular polarizability in the gas phase α_{static} has been calculated by the Clausius-Mossotti-equation using the listed values for V_M and $\epsilon_{r,\text{static}}$. The gas phase molecular polarisability α_{vis} in the visible has been obtained by the Lorentz-Lorenz-equation using experimental refractive index data at a wave length $\lambda = 589\,\text{nm}$. The polarisability α_{vis} of DMSO is from reference[180], all other data from reference[181].

respectively,

$$\alpha = 3\epsilon_0 \frac{n^2 - 1}{n^2 + 2} \frac{V_M}{N_A} \tag{C.5}$$

$$\alpha = 3\epsilon_0 \frac{\epsilon_r - 1}{\epsilon_r + 2} \frac{V_M}{N_A}, \tag{C.6}$$

where N_A is the Avogadro constant and V_M the molar volume of the fluid. In C.1 we report the static polarisability α_{static} and the polarisability in the visible α_{vis}. In the GHz frequency range the polarisability is expected to have a value somewhat in between these two limits, but note that electronic polarizability effects, that are dominant in the visible range, are not included in our classical MD simulations.

The assumption of an isolated molecule, inherent to the Clausius-Mossotti-equation, likely breaks down for a cylindrical column of liquid in a nanotube. In bulk, i.e. for a molecule embedded in a three-dimensional condensed phase, the Kirkwood-Fröhlich-equation instead is valid[182, 183]

$$\alpha_{\text{KF}} = 3\epsilon_0 \frac{(2\epsilon_r + 1)(\epsilon_r - 1)}{9\epsilon_r} \frac{V_M}{N_A}. \tag{C.7}$$

For water one obtains, $\alpha_{\text{static,KF}} = 1.4 \cdot 10^{-38}$C m^2/V, so the static polarizabilty increases by a factor of 20 compared to the gas phase prediction. Comparing with our fitted values for the polarizabilities, which are $\alpha_1 = 7.7 \cdot 10^{-40}$C m^2/V and $\alpha_2 = 5.7 \cdot 10^{-40}$C m^2/V, giving a total polarizability of $\alpha_{\text{tot}} = \alpha_1 + \alpha_2 = 1.3 \cdot 10^{-39}$C m^2/V, we are led to conclude that the two above discussed effects, decrease of polarizability due to relaxation effects that have to do with the finite frequency, and increase of polarizability due to collective effects, cancel out to some degree, but that collective effects dominate and lead to an overall increase of the water polarizability inside the CNT.

C.5 Equilibration of the Number of Water Molecules in the Tube

Since we run simulations in the NVT ensemble (constant particle number, volume and temperature), we need to make sure that the number of water molecules N inside the tube corresponds to the bulk chemical potential of water. In order to determine N, we add two reservoirs at the
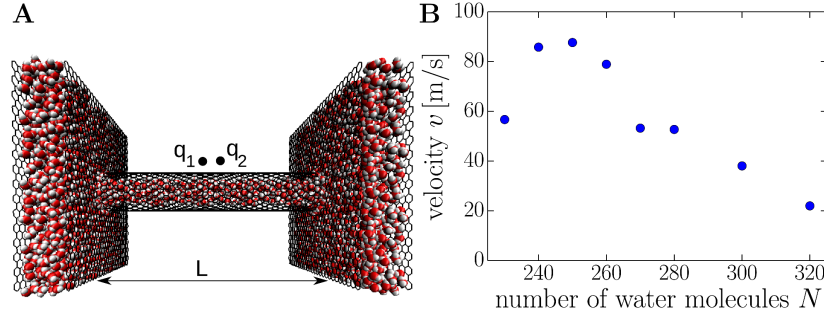
FIGURE C.4: (A) Illustration of our setup to determine the equilibrium number of water molecules inside the tube: Two pistons push water from the reservoirs with a pressure of 1 bar into the tube. (B) The flow velocity decreases when we increase the number of molecules inside the tube due to higher friction. For $N = 230$, on the other hand, the water tube inside the CNT becomes discontinuous, decreasing the pumping velocity. (Data for $n = 2$, $T = 10$ ps, $q = 1 e$, $\varphi = \pi/2$, $\delta = 0.5$ nm, $d = 1.07$ nm and $L = 8.5$ nm.)

two tube ends and two pistons that push water from the reservoirs into the tube (Figure C.4 A). The force on the pistons corresponds to a pressure of 1 bar. During such a simulation with two electrodes ($q = 1 e$, $T = 10$ ps, $\varphi = \pi/2$, $d = 1.07$ nm, $\delta = 0.5$ nm) we measure an average number of $N = 280$ water molecules inside the tube. This number for the tube of length $L = 8.5$ nm was used for all production runs without reservoirs in order to save computation time. We thus neglect variations of the water chemical potential due to a change of the pump parameters. As a check on the accuracy of our method, we in Figure C.4 B demonstrate that the flow speed depends only weakly on the number of water molecules. In fact, the pumping speed decreases with increasing number of water molecules, due to the higher friction. For a very low number of 230 water molecules, on the other hand, the flow also decreases, because in this case the water tube inside the CNT becomes discontinuous and shows partial dewetting.
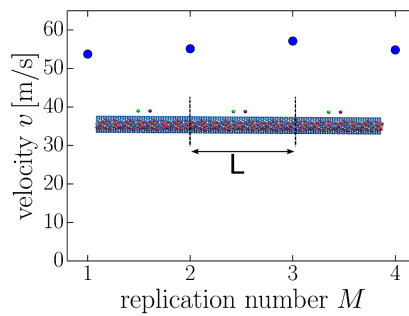
C.6 Effects of Periodic Boundary Conditions

FIGURE C.5: The flow velocity for a simulation box with M replicated pumps depends only weakly on M. A snapshot of the simulation system with three pumps ($M = 3$) is shown in the inset. (Data for $n = 2$, $T = 10$ ps, $q = 1 e$, $\varphi = \pi/2$, $\delta = 0.5$ nm, $d = 1.07$ nm and $L = 8.5$ nm.)

Since we apply periodic boundary conditions in all three dimensions, all atom charges and their periodic images are included in the Ewald summation calculated with *kspace pppm*[72]. The electric field is implemented by an external electric field equivalent to the unscreened electrode charges at positions $\vec{r}_i(t)$. Periodic images of these electrodes are not a priori included in LAMMPS' Ewald

	σ_{CO} [nm]	ϵ_{CO} [kJ/mol]	σ_{OO} [nm]	ϵ_{OO} [kJ/mol]
Our work	0.326	0.427	0.316	0.650
GROMOS96[184]	0.338	0.427	0.316	0.650
Werder et al.[169]	0.319	0.392	0.316	0.650

TABLE C.2: Lennard-Jones parameters for carbon-water and water-water interaction: The first line shows the parameters we use. For comparison we also show two other common force fields.

summation algorithm. For all simulations in chapter 5, we have manually added one image on each side by placing additional electrodes at $\vec{r}_i(t) - L\vec{e}_z$ and $\vec{r}_i(t) + L\vec{e}_z$.

To show that the pumping speed is not modified by finite-size effects, we perform test simulations in which the entire system containing the tube of length L as well as the $n = 2$ electrodes is explicitly replicated M times, as shown in the inset of Figure C.5. The resulting large simulation box of length ML is then simulated as before, manually adding one image of the electrodes on each side. The resultant pumping speed v in Figure C.5 shows that the replication number M has no effect on the pumping speed. We can thus exlude finite-size artifacts as the cause of the observed flow. All data in chapter 5 are obtained for $M = 1$.

C.7 Simulation Methods and Numerical Parameters

The CNT atoms are fixed in space and time, water interaction parameters are given by the SPC/E force field. Our Lennard-Jones parameters are listed in the first row of table C.2. For comparison, we also show a few other literature force fields for CNT-water interactions. The SHAKE algorithm of LAMMPS is used to keep the O-H distance and the H-O-H angle fixed.
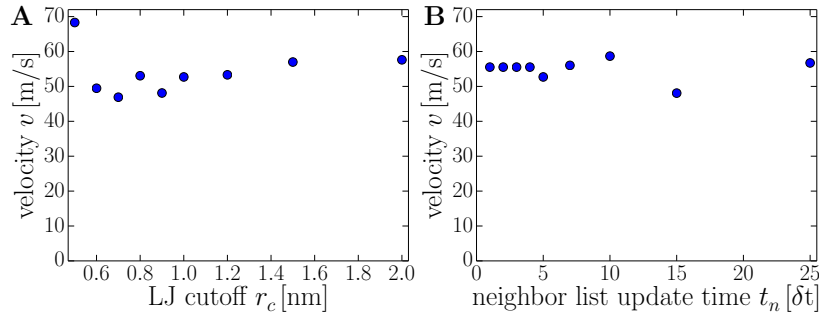

FIGURE C.6: (A) The flow speed for various LJ-cutoff lengths r_c: Except for a very small cutoff of $r_c = 0.5$ nm, the velocities show only weak dependence on r_c.
(B) The velocities for short neighbor list update times of $t_n < 5\,\delta t$ agree with our results for $t_n = 5\,\delta t$. (All data for $n = 2$, $T = 10$ ps, $q = 1\,e$, $\varphi = \pi/2$, $\delta = 0.5$ nm, $d = 1.07$ nm and $L = 8.5$ nm.)

In our simulations the Lennard-Jones-interaction is truncated above $r_c = 1$ nm and the neighbor list is updated every 5 timesteps. In Figure C.6 A the velocity measurements for longer cutoff lengths agree with the flow for the standard cutoff $r_c = 1$ nm. Only the very short cutoff 0.5 nm leads to a higher flow. Next, we test if our neighbor list update period has been chosen short enough. In Figure C.6 B we see that the velocities for short neighbor list update times of $t_n < 5\,\delta t$ agree with our value for $t_n = 5\,\delta t$. Only for longer periods the results vary.

In order to have a smooth field in time, we decrease the standard time step of $2\,\text{fs}$ for short oscillation periods T to $\delta t = T/50$. Hence for the shortest period $T = 10\,\text{fs}$ we employ a time step of $0.2\,\text{fs}$. Only velocity components perpendicular to the flow direction are used by the Nose/Hoover thermostat.
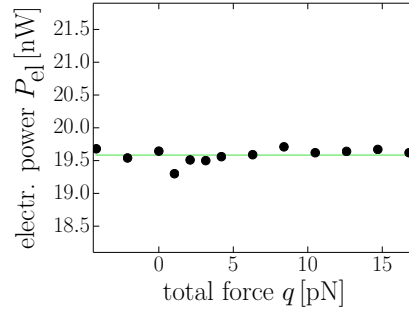
C.8   Consumed Electrostatic Power

FIGURE C.7: The consumed electrostatic power is roughly independent of the external force F_{ext}. (Data for $n = 2$, $T = 10\,\text{ps}$, $q = 1\,e$, $\varphi = \pi/2$, $\delta = 0.5\,\text{nm}$, $d = 1.07\,\text{nm}$ and $L = 8.5\,\text{nm}$.)

The consumed electrostatic power, defined in equation 5.77, is independent of the external force F_{ext} (Figure C.7). Consequently the efficiency is proportional to the performed mechanical work.

List of Publications

This thesis is based on the following papers, which have been published in or are under review for publication in peer-reviewed journals:

[i] **Klaus F. Rinne**, Julius C. F. Schulz, and Roland R. Netz. Impact of Secondary Structure and Hydration Water on the Dielectric Spectrum of Poly-Alanine and Possible Relation to the Debate on Slaved versus Slaving Water. *under review for J. Chem. Phys.*

[ii] **Klaus F. Rinne**, Stephan Gekle, and Roland R Netz. Ion-Specific Solvation Water Dynamics: Single Water versus Collective Water Effects. *J. Phys. Chem. A*, **118**, 11667-11677 (2014).
DOI: 10.1021/jp5066874

[iii] **Klaus F. Rinne**, Stephan Gekle, and Roland R Netz. Dissecting Ion-Specific Dielectric Spectra of Sodium-Halide Solutions into Solvation Water and Ionic Contributions. *J. Chem. Phys.*, **141**, 214502 (2014).
DOI: 10.1063/1.4901927

[iv] **Klaus F. Rinne**, Stephan Gekle, Douwe J. Bonthuis, and Ronald R. Netz. Nanoscale Pumping of Water by AC Electric Fields. *ACS Nano Lett.*, **12**, 1780-1783 (2012).
DOI: 10.1021/nl203614t

The following publication is not discussed in the present thesis:

[v] Douwe J. Bonthuis, **Klaus F. Rinne**, Kerstin Falk, C. Nadir Kaplan, Dominik Horinek, A. Nihat Berker, Lyderic Bocquet, and Roland R Netz. Theory and Simulations of Water Flow through Carbon Nanotubes: Prospects and Pitfalls. *J. Phys. Condens. Matter*, **23**, 184110 (2011).
DOI: 10.1088/0953-8984/23/18/184110

Bibliography

[1] Petersen, J., Sack, D. & Gabler, R. *Fundamentals of Physical Geography* (Cengage Learning, 2010).

[2] Stillinger, F. H. Water Revisited. *Science* **209**, 451–457 (1980).

[3] Errington, J. R. & Debenedetti, P. G. Relationship between Structural Order and the Anomalies of Liquid Water. *Nature* **409**, 318–321 (2001).

[4] Stokely, K., Mazza, M. G., Stanley, H. E. & Franzese, G. Effect of Hydrogen Bond Cooperativity on the Behavior of Water. *PNAS* **107**, 1301–1306 (2010).

[5] Widom, B., Bhimalapuram, P. & Koga, K. The Hydrophobic Effect. *PCCP* **5**, 3085–3093 (2003).

[6] Teeter, M. M. Water-Protein Interactions: Theory and Experiment. *Annu. Rev. Biophys. Bio.* **20**, 577–600 (1991).

[7] Wertz, D. H. & Scheraga, H. A. Influence of Water on Protein Structure. An Analysis of the Preferences of Amino Acid Residues for the Inside or Outside and for Specific Conformations in a Protein Molecule. *Macromolecules* **11**, 9–15 (1978).

[8] Haberler, M., Schöder, C. & Steinhauser, O. Hydrated Ionic Liquids with and without Solute: The Influence of Water Content and Protein Solutes. *J. Chem. Theory Comput.* **8**, 3911–3928 (2012).

[9] Selkoe, D. J. Folding Proteins in Fatal Ways. *Nature* **426**, 900–904 (2003).

[10] Orr, H. T. & Zoghbi, H. Y. Trinucleotide Repeat Disorders. *Annu. Rev. Neurosci.* **30**, 575–621 (2007).

[11] Kauzmann, W. Some Factors in the Interpretation of Protein Denaturation. *Adv. Protein Chem.* **14**, 1–63 (1959).

[12] Frauenfelder, H. *et al.* A Unified Model of Protein Dynamics. *PNAS* **106**, 5129–5134 (2009).

[13] Khodadadi, S. *et al.* Dynamics of Biological Macromolecules: Not a Simple Slaving by Hydration Water. *Biophys. J.* **98**, 1321–1326 (2010).

[14] Hribar, B., Southall, N. T., Vlachy, V. & Dill, K. A. How Ions Affect the Structure of Water. *JACS* **124**, 12302–12311 (2002).

[15] Kropman, M. & Bakker, H. Dynamics of Water Molecules in Aqueous Solvation Shells. *Science* **291**, 2118–2120 (2001).

[16] Nandi, N., Bhattacharyya, K. & Bagchi, B. Dielectric Relaxation and Solvation Dynamics of Water in Complex Chemical and Biological Systems. *Chem. Rev.* **100**, 2013–2046 (2000).

[17] Barthlott, W., Cerman, Z. & Stosch, A. K. Der Lotus-Effekt: Selbstreinigende Oberflächen und ihre Übertragung in die Technik. *Biol. uns. Zeit* **34**, 290–296 (2004).

[18] Marmur, A. The Lotus Effect: Superhydrophobicity and Metastability. *Langmuir* **20**, 3517–3519 (2004).

[19] Otten, A. & Herminghaus, S. How Plants Keep Dry: A Physicist's Point of View. *Langmuir* **20**, 2405–2408 (2004).

[20] Berezhkovskii, A. & Hummer, G. Single-File Transport of Water Molecules through a Carbon Nanotube. *Phys. Rev. Lett.* **89**, 064503 (2002).

[21] Falk, K., Sedlmeier, F., Joly, L., Netz, R. R. & Bocquet, L. Molecular Origin of Fast Water Transport in Carbon Nanotube Membranes: Superlubricity versus Curvature Dependent Friction. *ACS Nano Lett.* **10**, 4067–4073 (2010).

[22] Holt, J. K. *et al.* Fast Mass Transport Through Sub-2-Nanometer Carbon Nanotubes. *Science* **312**, 1034–1037 (2006).

[23] Majumder, M., Chopra, N., Andrews, R. & Hinds, B. J. Nanoscale Hydrodynamics: Enhanced Flow in Carbon Nanotubes. *Nature* **438**, 44 (2005).

[24] Whitby, M. & Quirke, N. Fluid Flow in Carbon Nanotubes and Nanopipes. *Nature Nano.* **2**, 87–94 (2007).

[25] Longhurst, M. J. & Quirke, N. Temperature-Driven Pumping of Fluid through Single-Walled Carbon Nanotubes. *ACS Nano Lett.* **7**, 3324–3328 (2007).

[26] Wang, B. & Král, P. Coulombic Dragging of Molecules on Surfaces Induced by Separately Flowing Liquids . *JACS* **128**, 15984–15985 (2006).

[27] Insepov, Z., Wolf, D. & Hassanein, A. Nanopumping using Carbon Nanotubes. *ACS Nano Lett.* **6**, 1893–1895 (2006).

[28] Gekle, S. & Netz, R. R. Nanometer-Resolved Radio-Frequency Absorption and Heating in Biomembrane Hydration Layers. *J. Phys. Chem. B* (2014).

[29] van Deventer, E., van Rongen, E. & Saunders, R. WHO Research Agenda for Radiofrequency Fields. *Bioelectromagnetics* **32**, 417–421 (2011).

[30] Bonthuis, D. J., Gekle, S. & Netz, R. R. Dielectric Profile of Interfacial Water and its Effect on Double-Layer Capacitance. *Phys. Rev. Lett.* **107**, 166102 (2011).

[31] Fu, D.-W. *et al.* Dielectric Anisotropy of a Homochiral Trinuclear Nickel (II) Complex. *JACS* **129**, 5346–5347 (2007).

[32] Ratna, B. & Shashidhar, R. Dielectric Studies on Liquid Crystals of Strong Positive Dielectric Anisotropy. *Mol. Cryst. Liq. Cryst.* **42**, 113–125 (1977).

[33] Schubert, M., Tiwald, T. & Herzinger, C. Infrared Dielectric Anisotropy and Phonon Modes of Sapphire. *Phys. Rev. B* **61**, 8187 (2000).

[34] Gekle, S. & Netz, R. R. Anisotropy in the Dielectric Spectrum of Hydration Water and its Relation to Water Dynamics. *J. Chem. Phys.* **137**, 104704 (2012).

[35] Zhang, C., Gygi, F. & Galli, G. Strongly Anisotropic Dielectric Relaxation of Water at the Nanoscale. *J. Phys. Chem. Lett.* **4**, 2477–2481 (2013).

[36] Bonthuis, D. J., Gekle, S. & Netz, R. R. Profile of the Static Permittivity Tensor of Water at Interfaces: Consequences for Capacitance, Hydration Interaction and Ion Adsorption. *Langmuir* **28**, 7679–7694 (2012).

[37] Hunter, R. J. *Foundations of Colloid Science* (2001).

[38] Lyklema, J. *Fundamentals of Interface and Colloid Science: Soft Colloids*, vol. 5 (Academic press, 2005).

[39] Bonthuis, D. J. & Netz, R. R. Unraveling the Combined Effects of Dielectric and Viscosity Profiles on Surface Capacitance, Electro-Osmotic Mobility, and Electric Surface Conductivity. *Langmuir* **28**, 16049–16059 (2012).

[40] Bonthuis, D. J. & Netz, R. R. Beyond the Continuum: How Molecular Solvent Structure Affects Electrostatics and Hydrodynamics at Solid–Electrolyte Interfaces. *J. Phys. Chem. B* **117**, 11397–11413 (2013).

[41] Bagchi, B. Water Dynamics in the Hydration Layer around Proteins and Micelles. *Chem. Rev.* **105**, 3197–3219 (2005).

[42] Born, B., Weingärtner, H., Bründermann, E. & Havenith, M. Solvation Dynamics of Model Peptides Probed by Terahertz Spectroscopy. Observation of the Onset of Collective Network Motions. *JACS* **131**, 3752–3755 (2009).

[43] Auty, R. P. & Cole, R. H. Dielectric Properties of Ice and Solid D_2O. *J. Chem. Phys.* **20**, 1309–1314 (1952).

[44] Reagor, D., Ahrens, E., Cheong, S., Migliori, A. & Fisk, Z. Large Dielectric Constants and Massive Carriers in La_2CuO_4. *Phys. Rev. Lett.* **62**, 2048 (1989).

[45] Barthel, J. *et al.* Dielectric Relaxation Spectroscopy of Electrolyte Solutions. Recent Developments and Prospects. *J. Mol. Liq.* **78**, 83–109 (1998).

[46] Buchner, R. & Barthel, J. Dielectric Relaxation in Solutions. *Ann Rep. S. C* **91**, 71–106 (1994).

[47] Kremer, F. & Schönhals, A. *Broadband Dielectric Spectroscopy* (Springer, 2003).

[48] Funkner, S. *et al.* Watching the Low-Frequency Motions in Aqueous Salt Solutions: The Terahertz Vibrational Signatures of Hydrated Ions. *JACS* **134**, 1030–1035 (2012).

[49] Han, P. *et al.* A Direct Comparison between Terahertz Time-Domain Spectroscopy and Far-Infrared Fourier Transform Spectroscopy. *J. Appl. Phys.* **89**, 2357–2359 (2001).

[50] Van Exter, M., Fattinger, C. & Grischkowsky, D. Terahertz Time-Domain Spectroscopy of Water Vapor. *Opt. Lett.* **14**, 1128–1130 (1989).

[51] Huang, F. *et al.* Terahertz Study of 1, 3, 5-Trinitro-S-Triazine by Time-Domain and Fourier Transform Infrared Spectroscopy. *Appl. Phys. Lett.* **85**, 5535–5537 (2004).

[52] Buchner, R., Barthel, J. & Stauber, J. The Dielectric Relaxation of Water between 0°C and 35°C. *Chem. Phys. Lett.* **306**, 57–63 (1999).

[53] Buchner, R., Hefter, G. T. & May, P. M. Dielectric Relaxation of Aqueous NaCl Solutions. *J. Phys. Chem. A* **103**, 1–9 (1999).

[54] Buchner, R., Hefter, G. T. & Barthel, J. Dielectric Relaxation of Aqueous NaF and KF Solutions. *J. Chem. Soc., Faraday Trans.* **90**, 2475–2479 (1994).

[55] Wachter, W., Kunz, W., Buchner, R. & Hefter, G. Is there an Anionic Hofmeister Effect on Water Dynamics? Dielectric Spectroscopy of Aqueous Solutions of NaBr, NaI, NaNO$_3$, NaClO$_4$, and NaSCN. *J. Phys. Chem. A* **109**, 8675–8683 (2005).

[56] Tromans, A., May, P. M., Hefter, G., Sato, T. & Buchner, R. Ion Pairing and Solvent Relaxation Processes in Aqueous Solutions of Sodium Malonate and Sodium Succinate. *J. Phys. Chem. B* **108**, 13789–13795 (2004).

[57] Buchner, R., Capewell, S. G., Hefter, G. & May, P. M. Ion-Pair and Solvent Relaxation Processes in Aqueous Na$_2$SO$_4$ Solutions. *J. Phys. Chem. B* **103**, 1185–1192 (1999).

[58] Buchner, R., Chen, T. & Hefter, G. Complexity in Simple Electrolyte Solutions: Ion Pairing in MgSO$_4$ (aq). *J. Phys. Chem. B* **108**, 2365–2375 (2004).

[59] Kaatze, U. & Giese, K. Dielectric Spectroscopy on some Aqueous Solutions of 3: 2 Valent Electrolytes. A Combined Frequency and Time Domain Study. *J. Mol. Liq.* **36**, 15–35 (1987).

[60] Schrödle, S., Wachter, W., Buchner, R. & Hefter, G. Scandium Sulfate Complexation in Aqueous Solution by Dielectric Relaxation Spectroscopy. *Inorg. Chem.* **47**, 8619–8628 (2008).

[61] Knocks, A. & Weingärtner, H. The Dielectric Spectrum of Ubiquitin in Aqueous Solution. *J. Phys. Chem. B* **105**, 3635–3638 (2001).

[62] Oleinikova, A., Sasisanker, P. & Weingärtner, H. What Can Really be Learned from Dielectric Spectroscopy of Protein Solutions? A Case Study of Ribonuclease A. *J. Phys. Chem. B* **108**, 8467–8474 (2004).

[63] Engel, G. & Hertz, H. On the Negative Hydration. A Nuclear Magnetic Relaxation Study. *Ber. Bunsen Ges.* **72**, 808–834 (1968).

[64] Marcus, Y. Effect of Ions on the Structure of Water: Structure Making and Breaking. *Chem. Rev.* **109**, 1346–1370 (2009).

[65] Bakulin, A. A., Pshenichnikov, M. S., Bakker, H. J. & Petersen, C. Hydrophobic Molecules Slow Down the Hydrogen-Bond Dynamics of Water. *J. Phys. Chem. A* **115**, 1821–1829 (2011).

[66] Moilanen, D. E., Wong, D., Rosenfeld, D. E., Fenn, E. E. & Fayer, M. Ion–Water Hydrogen-Bond Switching Observed with 2D IR Vibrational Echo Chemical Exchange Spectroscopy. *PNAS* **106**, 375–380 (2009).

[67] Rezus, Y. & Bakker, H. Observation of Immobilized Water Molecules around Hydrophobic Groups. *Phys. Rev. Lett.* **99**, 148301 (2007).

[68] Heisler, I. A., Mazur, K. & Meech, S. R. Low-Frequency Modes of Aqueous Alkali Halide Solutions: an Ultrafast Optical Kerr Effect Study. *J. Phys. Chem. B* **115**, 1863–1873 (2011).

[69] Park, S. & Fayer, M. D. Hydrogen Bond Dynamics in Aqueous NaBr Solutions. *PNAS* **104**, 16731–16738 (2007).

[70] Caillol, J. M., Levesque, D. & Weis, J. J. Theoretical Calculation of Ionic Solution Properties. *J. Chem. Phys.* **85**, 6645–6657 (1986).

[71] Hess, B., Kutzner, C., van der Spoel, D. & Lindahl, E. GROMACS 4: Algorithms for Highly Efficient, Load-Balanced, and Scalable Molecular Simulation. *J. Chem. Theory Comput.* **4**, 435–447 (2008).

[72] Plimpton, S. Fast Parallel Algorithms for Short-Range Molecular Dynamics. *J. Comp. Phys.* **117**, 1–17 (1995).

[73] Forester, T. R. & Smith, W. SHAKE, Rattle, and Roll: Efficient Constraint Algorithms for Linked Rigid Bodies. *J. Comput. Chem.* **19**, 102–111 (1998).

[74] Plimpton, S. LAMMPS User Manual 483–484 (1992).

[75] Jorgensen, W. L. Quantum and Statistical Mechanical Studies of Liquids. 10. Transferable Intermolecular Potential Functions for Water, Alcohols, and Ethers. Application to Liquid Water. *JACS* **103**, 335–340 (1981).

[76] Berendsen, H. J., Postma, J., Van Gunsteren, W. & Hermans, J. Interaction Models for Water in Relation to Protein Hydration. In *Intermolecular Forces*, 331–342 (Springer, 1981).

[77] Jorgensen, W. L., Chandrasekhar, J., Madura, J. D., Impey, R. W. & Klein, M. L. Comparison of Simple Potential Functions for Simulating Liquid Water. *J. Chem. Phys.* **79**, 926–935 (1983).

[78] Berendsen, H., Grigera, J. & Straatsma, T. The Missing Term in Effective Pair Potentials. *J. Phys. Chem.* **91**, 6269–6271 (1987).

[79] Mahoney, M. W. & Jorgensen, W. L. A Five-Site Model for Liquid Water and the Reproduction of the Density Anomaly by Rigid, Nonpolarizable Potential Functions. *J. Chem. Phys.* **112**, 8910–8922 (2000).

[80] Höchtl, P., Boresch, S., Bitomsky, W. & Steinhauser, O. Rationalization of the Dielectric Properties of Common Three-Site Water Models in Terms of their Force Field Parameters. *J. Chem. Phys.* **109**, 4927–4937 (1998).

[81] Rami Reddy, M. & Berkowitz, M. The Dielectric Constant of SPC/E Water. *Chem. Phys. Lett.* **155**, 173–176 (1989).

[82] Fyta, M. & Netz, R. R. Ionic Force Field Optimization Based on Single-Ion and Ion-Pair Solvation Properties: Going beyond Standard Mixing Rules. *J. Chem. Phys.* **136**, 124103 (2012).

[83] Duan, Y. *et al.* A Point-Charge Force Field for Molecular Mechanics Simulations of Proteins Based on Condensed-Phase Quantum Mechanical Calculations. *J. Comput. Chem.* **24**, 1999–2012 (2003).

[84] Berendsen, H. J., Postma, J. P. M., van Gunsteren, W. F., DiNola, A. & Haak, J. Molecular Dynamics with Coupling to an External Bath. *J. Chem. Phys.* **81**, 3684–3690 (1984).

[85] Hoover, W. G. Canonical Dynamics: Equilibrium Phase-Space Distributions. *Phys. Rev. A* **31**, 1695 (1985).

[86] Nosé, S. A Molecular Dynamics Method for Simulations in the Canonical Ensemble. *Mol. Phys.* **52**, 255–268 (1984).

[87] Ewald, P. P. Die Berechnung Optischer und Elektrostatischer Gitterpotentiale. *Ann. Phys.* **369**, 253–287 (1921).

[88] Darden, T., York, D. & Pedersen, L. Particle Mesh Ewald: An N log (N) Method for Ewald Sums in Large Systems. *J. Chem. Phys.* **98**, 10089–10092 (1993).

[89] Hockney, R. W. & Eastwood, J. W. *Computer Simulation Using Particles* (McGrwa-Hill, 1981).

[90] van der Spoel, D. *et al.* Gromacs User Manual version 4.0 53–55 (2008).

[91] Bonthuis, D. J., Horinek, D., Bocquet, L. & Netz, R. R. Electrokinetics at Aqueous Interfaces without Mobile Charges. *Langmuir* **26**, 12614–12625 (2010).

[92] Madden, P. & Kivelson, D. A Consistent Molecular Treatment of Dielectric Phenomena. *Adv. Chem. Phys.* 467–566 (1984).

[93] Buchner, R. & Hefter, G. Interactions and Dynamics in Electrolyte Solutions by Dielectric Spectroscopy. *PCCP* **11**, 8984–8999 (2009).

[94] Chandra, A. Static Dielectric Constant of Aqueous Electrolyte Solutions: Is there any Dynamic Contribution? *J. Chem. Phys.* **113**, 903–905 (2000).

[95] Chowdhuri, S. & Chandra, A. Molecular Dynamics Simulations of Aqueous NaCl and KCl Solutions: Effects of Ion Concentration on the Single-Particle, Pair, and Collective Dynamical Properties of Ions and Water Molecules. *J. Chem. Phys.* **115**, 3732 (2001).

[96] Zasetsky, A. Y. & Svishchev, I. M. Dielectric Response of Concentrated NaCl Aqueous Solutions: Molecular Dynamics Simulations. *J. Chem. Phys.* **115**, 1448 (2001).

[97] Schröder, C., Rudas, T. & Steinhauser, O. Simulation Studies of Ionic Liquids: Orientational Correlations and Static Dielectric Properties. *J. Chem. Phys.* **125**, 244506 (2006).

[98] Schröder, C., Wakai, C., Weingärtner, H. & Steinhauser, O. Collective Rotational Dynamics in Ionic Liquids: A Computational and Experimental Study of 1-Butyl-3-Methyl-Imidazolium Tetrafluoroborate. *J. Chem. Phys.* **126**, 084511 (2007).

[99] Sala, J., Guardia, E. & Marti, J. Effects of Concentration on Structure, Dielectric, and Dynamic Properties of Aqueous NaCl Solutions using a Polarizable Model. *J. Chem. Phys.* **132**, 214505 (2010).

[100] Schröder, C. & Steinhauser, O. Using Fit Functions in Computational Dielectric Spectroscopy. *J. Chem. Phys.* **132**, 244109–244109 (2010).

[101] Sega, M., Kantorovich, S., Holm, C. & Arnold, A. Kinetic and Pairing Contributions in the Dielectric Spectra of Electrolyte Solutions. *J. Chem. Phys.* **140**, 211101 (2014).

[102] Weingärtner, H., Knocks, A., Boresch, S., Höchtl, P. & Steinhauser, O. Dielectric Spectroscopy in Aqueous Solutions of Oligosaccharides: Experiment Meets Simulation. *J. Chem. Phys.* **115**, 1463–1472 (2001).

[103] Tielrooij, K. J., Garcia-Araez, N., Bonn, M. & Bakker, H. J. Cooperativity in Ion Hydration. *Science* **328**, 1006–1009 (2010).

[104] Holzmann, J., Ludwig, R., Geiger, A. & Paschek, D. Pressure and Salt Effects in Simulated Water: Two Sides of the Same Coin? *Angew. Chem. Int. Ed.* **46**, 8907–8911 (2007).

[105] O'Brien, J. T., Prell, J. S., Bush, M. F. & Williams, E. R. Sulfate Ion Patterns Water at Long Distance. *JACS* **132**, 8248–8249 (2010).

[106] Kohler, F., Findenegg, G., Fischer, J. & Posch, H. *The Liquid State* (Verlag Chemie Weinheim, 1972).

[107] De Groot, S. & Mazur, P. *Non-Equilibrium Thermodynamics* (Dover, New York, 1984).

[108] Kalcher, I. & Dzubiella, J. Structure-Thermodynamics Relation of Electrolyte Solutions. *J. Chem. Phys.* **130**, 134507 (2009).

[109] Fennell, C. J., Bizjak, A., Vlachy, V. & Dill, K. A. Ion Pairing in Molecular Simulations of Aqueous Alkali Halide Solutions. *J. Phys. Chem. B* **113**, 6782–6791 (2009).

[110] Kaatze, U. Dielectric Effects in Aqueous Solutions of 1:1, 2:1, and 3:1 Valent Electrolytes: Kinetic Depolarization, Saturation, and Solvent Relaxation. *Z. Phys. Chem.* **135**, 51–75 (1983).

[111] Marcus, Y. Ionic Radii in Aqueous Solutions. *Chem. Rev.* **88**, 1475–1498 (1988).

[112] Alper, H. E. & Levy, R. M. Field Strength Dependence of Dielectric Saturation in Liquid Water. *J. Phys. Chem.* **94**, 8401–8403 (1990).

[113] Lenart, P. J., Jusufi, A. & Panagiotopoulos, A. Z. Effective Potentials for 1: 1 Electrolyte Solutions Incorporating Dielectric Saturation and Repulsive Hydration. *J. Chem. Phys.* **126**, 044509 (2007).

[114] Martí, J., Guàrdia, E. & Padró, J. Dielectric Properties and Infrared Spectra of Liquid Water: Influence of the Dynamic Cross-Correlations. *J. Chem. Phys.* **101**, 10883–10891 (1994).

[115] Sedlmeier, F. & Netz, R. R. Solvation Thermodynamics and Heat Capacity of Polar and Charged Solutes in Water. *J. Chem. Phys.* **138**, 115101 (2013).

[116] Kirkwood, J. G. The Dielectric Polarization of Polar Liquids. *J. Chem. Phys.* **7**, 911–919 (1939).

[117] Smith, P. E. & van Gunsteren, W. F. Consistent Dielectric Properties of the Simple Point Charge and Extended Simple Point Charge Water Models at 277 and 300 K. *J. Chem. Phys.* **100**, 3169–3174 (1994).

[118] Sega, M., Kantorovich, S. & Arnold, A. Kinetic Dielectric Decrement Revisited: Phenomenology of Finite Ion Concentrations. *Physical Chemistry Chemical Physics* **17**, 130–133 (2015).

[119] Chambers, J. F., Stokes, J. M. & Stokes, R. H. Conductances of Concentrated Aqueous Sodium and Potassium Chloride Solutions at 25°. *J. Phys. Chem.* **60**, 985–986 (1956).

[120] Onsager, L. Zur Theorie der Elektrolyte. I. *Phys. Z.* **27**, 388–392 (1926).

[121] Harder, E., Eaves, J. D., Tokmakoff, A. & Berne, B. Polarizable Molecules in the Vibrational Spectroscopy of Water. *PNAS* **102**, 11611–11616 (2005).

[122] Laage, D. & Hynes, J. T. Reorientional Dynamics of Water Molecules in Anionic Hydration Shells. *PNAS* **104**, 11167–11172 (2007).

[123] Stirnemann, G., Hynes, J. T. & Laage, D. Water Hydrogen Bond Dynamics in Aqueous Solutions of Amphiphiles. *J. Phys. Chem. B* **114**, 3052–3059 (2010).

[124] Boisson, J., Stirnemann, G., Laage, D. & Hynes, J. T. Water Reorientation Dynamics in the First Hydration Shells of F- and I-. *PCCP* **13**, 19895–19901 (2011).

[125] Stirnemann, G., Wernersson, E., Jungwirth, P. & Laage, D. Mechanisms of Acceleration and Retardation of Water Dynamics by Ions. *JACS* **135**, 11824–11831 (2013).

[126] Tielrooij, K., Van Der Post, S., Hunger, J., Bonn, M. & Bakker, H. Anisotropic Water Reorientation around Ions. *J. Phys. Chem. B* **115**, 12638–12647 (2011).

[127] van der Post, S. T., Scheidelaar, S. & Bakker, H. J. Femtosecond Study of the Effects of Ions on the Reorientation Dynamics of Water. *J. Mol. Liq.* **176**, 22–28 (2012).

[128] Boresch, S., Ringhofer, S., Höchtl, P. & Steinhauser, O. Towards a Better Description and Understanding of Biomolecular Solvation. *Biophys. Chem.* **78**, 43–68 (1999).

[129] Murarka, R. K. & Head-Gordon, T. Dielectric Relaxation of Aqueous Solutions of Hydrophilic versus Amphiphilic Peptides. *J. Phys. Chem. B* **112**, 179–186 (2008).

[130] Bertolini, D., Tani, A. & Vallauri, R. Collective Motion and Interparticle Correlations in Liquid Water: A Molecular Dynamics Simulation. *Mol. Phys.* **73**, 69–78 (1991).

[131] Bertolini, D. & Tani, A. The Frequency and Wavelength Dependent Dielectric Permittivity of Water. *Mol. Phys.* **75**, 1065–1088 (1992).

[132] Lee, S. H. & Rasaiah, J. C. Molecular Dynamics Simulation of Ion Mobility. 2. Alkali Metal and Halide Ions Using the SPC/E Model for Water at 25°C. *J. Phys. Chem.* **100**, 1420–1425 (1996).

[133] Koneshan, S., Rasaiah, J. C., Lynden-Bell, R. & Lee, S. Solvent Structure, Dynamics, and Ion Mobility in Aqueous Solutions at 25°C. *J. Phys. Chem. B* **102**, 4193–4204 (1998).

[134] Guàrdia, E., Laria, D. & Martí, J. Hydrogen Bond Structure and Dynamics in Aqueous Electrolytes at Ambient and Supercritical Conditions. *J. Phys. Chem. B* **110**, 6332–6338 (2006).

[135] Hubbard, J., Onsager, L., Van Beek, W. & Mandel, M. Kinetic Polarization Deficiency in Electrolyte Solutions. *PNAS* **74**, 401–404 (1977).

[136] Weingärtner, H., Nadolny, H., Oleinikova, A. & Ludwig, R. Collective Contributions to the Dielectric Relaxation of Hydrogen-Bonded Liquids. *J. Chem. Phys.* **120**, 11692–11697 (2004).

[137] Rezus, Y. & Bakker, H. On the Orientational Relaxation of HDO in Liquid Water. *J. Chem. Phys.* **123**, 114502–114502 (2005).

[138] Chowdhuri, S. & Chandra, A. Dynamics of Halide Ion-Water Hydrogen Bonds in Aqueous Solutions: Dependence on Ion Size and Temperature. *J. Phys. Chem. B* **110**, 9674–9680 (2006).

[139] Lin, Y.-S., Auer, B. & Skinner, J. Water Structure, Dynamics, and Vibrational Spectroscopy in Sodium Bromide Solutions. *J. Chem. Phys.* **131**, 144511 (2009).

[140] Giammanco, C. H., Wong, D. B. & Fayer, M. D. Water Dynamics in Divalent and Monovalent Concentrated Salt Solutions. *J. Phys. Chem. B* **116**, 13781–13792 (2012).

[141] Kropman, M., Nienhuys, H.-K. & Bakker, H. Real-Time Measurement of the Orientational Dynamics of Aqueous Solvation Shells in Bulk Liquid Water. *Phys. Rev. Lett.* **88**, 077601 (2002).

[142] Sajadi, M. *et al.* Observing the Hydration Layer of Trehalose with a Linked Molecular Terahertz Probe. *J. Phys. Chem. Lett.* **5**, 1845–1849 (2014).

[143] Grosse, C. & Delgado, A. Dielectric Dispersion in Aqueous Colloidal Systems. *Curr. Opin. Colloid In.* **15**, 145–159 (2010).

[144] Wolf, M., Gulich, R., Lunkenheimer, P. & Loidl, A. Broadband Dielectric Spectroscopy on Human Blood. *Biochim. Biophys. Acta* **1810**, 727–740 (2011).

[145] Miura, N., Hayashi, Y., Shinyashiki, N. & Mashimo, S. Observation of Unfreezable Water in Aqueous Solution of Globule Protein by Microwave Dielectric Measurement. *Biopolymers* **36**, 9–16 (1995).

[146] Cametti, C., Marchetti, S., Gambi, C. & Onori, G. Dielectric Relaxation Spectroscopy of Lysozyme Aqueous Solutions: Analysis of the δ-Dispersion and the Contribution of the Hydration Water. *J. Phys. Chem. B* **115**, 7144–7153 (2011).

[147] Schwan, H. Electrical Properties of Blood and its Constitutents: Alternating Current Spectroscopy. *Blut* **46**, 185–197 (1983).

[148] Rodríguez-Arteche, I., Cerveny, S., Alegría, Á. & Colmenero, J. Dielectric Spectroscopy in the GHz Region on Fully Hydrated Zwitterionic Amino Acids. *PCCP* **14**, 11352–11362 (2012).

[149] Sasisanker, P. & Weingärtner, H. Hydration Dynamics of Water near an Amphiphilic Model Peptide at Low Hydration Levels: A Dielectric Relaxation Study. *Chem. Phys. Chem.* **9**, 2802–2808 (2008).

[150] Bone, S. Dielectric Studies of Native, Unfolded and Intermediate Forms of Beta-Lactamase. *Phys. Med. Biol.* **39**, 1801 (1994).

[151] Hayashi, Y., Katsumoto, Y., Omori, S., Kishii, N. & Yasuda, A. Liquid Structure of the Urea-Water System Studied by Dielectric Spectroscopy. *J. Phys. Chem. B* **111**, 1076–1080 (2007).

[152] Idrissi, A. *et al.* The Effect of Urea on the Structure of Water: A Molecular Dynamics Simulation. *J. Phys. Chem. B* **114**, 4731–4738 (2010).

[153] Heyden, M. & Havenith, M. Combining THz Spectroscopy and MD Simulations to Study Protein-Hydration Coupling . *Methods* **52**, 74 – 83 (2010).

[154] Wolf, M., Gulich, R., Lunkenheimer, P. & Loidl, A. Relaxation Dynamics of a Protein Solution Investigated by Dielectric Spectroscopy . *Biochim. Biophys. Acta* **1824**, 723 – 730 (2012).

[155] Kaatze, U. Complex Permittivity of Water as a Function of Frequency and Temperature. *J. Chem. Eng. Data* **34**, 371–374 (1989).

[156] Boresch, S., Willensdorfer, M. & Steinhauser, O. A Molecular Dynamics Study of the Dielectric Properties of Aqueous Solutions of Alanine and Alanine Dipeptide. *J. Chem. Phys.* **120**, 3333–3347 (2004).

[157] Hamm, P., Helbing, J. & Bredenbeck, J. Two-Dimensional Infrared Spectroscopy of Photoswitchable Peptides. *Annu. Rev. Phys. Chem.* **59**, 291–317 (2008).

[158] Serrano, A. L., Tucker, M. J. & Gai, F. Direct Assessment of the α-Helix Nucleation Time. *J. Phys. Chem. B* **115**, 7472–7478 (2011).

[159] Ebbinghaus, S. *et al.* An Extended Dynamical Hydration Shell around Proteins. *PNAS* **104**, 20749–20752 (2007).

[160] Born, B., Kim, S. J., Ebbinghaus, S., Gruebele, M. & Havenith, M. The Terahertz Dance of Water with the Proteins: The Effect of Protein Flexibility on the Dynamical Hydration Shell of Ubiquitin. *Faraday Discuss.* **141**, 161–173 (2009).

[161] Bussi, G., Donadio, D. & Parrinello, M. Canonical Sampling through Velocity Rescaling. *J. Chem. Phys.* **126**, 014101 (2007).

[162] Parrinello, M. & Rahman, A. Polymorphic Transitions in Single Crystals: A New Molecular Dynamics Method. *J. Appl. Phys.* **52**, 7182–7190 (1981).

[163] Boresch, S., Höchtl, P. & Steinhauser, O. Studying the Dielectric Properties of a Protein Solution by Computer Simulation. *J. Phys. Chem. B* **104**, 8743–8752 (2000).

[164] Broersma, S. Rotational Diffusion Constant of a Cylindrical Particle. *J. Chem. Phys.* **32**, 1626–1631 (1960).

[165] Fenimore, P. W., Frauenfelder, H., McMahon, B. H. & Parak, F. G. Slaving: Solvent Fluctuations Dominate Protein Dynamics and Functions. *PNAS* **99**, 16047–16051 (2002).

[166] Gong, X. *et al.* A Charge-Driven Molecular Water Pump. *Nature Nano.* **2**, 709–712 (2007).

[167] Joseph, S. & Aluru, N. R. Pumping of Confined Water in Carbon Nanotubes by Rotation-Translation Coupling. *Phys. Rev. Lett.* **101**, 064502 (2008).

[168] Wong-ekkabut, J., Miettinen, M. S., Dias, C. & Karttunen, M. Static Charges cannot Drive a Continuous Flow of Water Molecules through a Carbon Nanotube . *Nature Nano.* **5**, 555 (2010).

[169] Zuo, G., Shen, R., Ma, S. & Guo, W. Transport Properties of Single-File Water Molecules inside a Carbon Nanotube Biomimicking Water Channel. *ACS Nano Lett.* **4**, 205–210 (2010).

[170] Bonthuis, D. J. *et al.* Comment on "Pumping of Confined Water in Carbon Nanotubes by Rotation-Translation Coupling". *Phys. Rev. Lett.* **105**, 209401 (2010).

[171] Hasted, J. B. *Aqueous Dielectrica* (Chapman and Hall, 1973).

[172] Thomas, J. A. & McGaughey, A. J. H. Water Flow in Carbon Nanotubes: Transition to Subcontinuum Transport. *Phys. Rev. Lett.* **102**, 184502 (2009).

[173] Bonthuis, D. J., Horinek, D., Bocquet, L. & Netz, R. R. Electrohydraulic Power Conversion in Planar Nanochannels. *Phys. Rev. Lett.* **103**, 144503 (2009).

[174] van der Heyden, F. H., Bonthuis, D. J., Stein, D., Meyer, C. & Dekker, C. Power Generation by Pressure-Driven Transport of Ions in Nanofluidic Channels. *ACS Nano Lett.* **7**, 1022–1025 (2007).

[175] Whitby, M., Cagnon, L., Thanou, M. & Quirke, N. Enhanced Fluid Flow through Nanoscale Carbon Pipes. *ACS Nano Lett.* **8**, 2632–2637 (2008).

[176] Oosterkamp, T. H. *et al.* Microwave Spectroscopy of a Quantum-Dot Molecule . *Nature* **395**, 783–787 (1998).

[177] Lu, W., Wang, D. & Chen, L. Near-Static Dielectric Polarization of Individual Carbon Nanotubes. *ACS Nano Lett.* **7**, 2729–2733 (2007).

[178] Chopra, N. G. *et al.* Boron Nitride Nanotubes. *Science* **269**, 966–967 (1995).

[179] Wernersson, E. & Jungwirth, P. Effect of Water Polarizability on the Properties of Solutions of Polyvalent Ions: Simulations of Aqueous Sodium Sulfate with Different Force Fields. *J. Chem. Theory Comput.* **6**, 3233–3240 (2010).

[180] Pacak, P. Polarizability and Molecular Radius of Dimethyl-Sulfoxide and Dimethylformamide from Refractive Index Data. *J. Sol. Chem.* **16**, 71–77 (1987).

[181] Lide, D. R. *Handbook of Chemistry and Physics* (CRC Press, 2003).

[182] Böttcher, C. J. F. *Theory of Electric Polarization* (Elsevier, 1973).

[183] Neumann, M. Dipole Moment Fluctuation Formulas in Computer Simulations of Polar Systems. *Mol. Phys.* **50**, 841–858 (1983).

[184] Scott, W. R. *et al.* The GROMOS Biomolecular Simulation Program Package. *J. Phys. Chem. A* **103**, 3596–3607 (1999).

Abstract

The electrostatic interaction is one of the fundamental forces and is extremely important for the dynamics of highly polar water molecules and the network of hydrogen bonds. Experimental dielectric relaxation spectroscopy measurements established that the addition of substances such as salts to water changes the strength of the dielectric absorption and the position of the absorption maximum in the frequency domain. But an unambiguous assignment of spectral resonances to interactions between various components of the solution without the support from atomistic simulations is impossible.

The dielectric spectrum of aqueous sodium-halide solutions is calculated from molecular dynamics simulations in this thesis and is in good agreement with the experimental measurements. By splitting the dielectric signal into cross-correlations between different contributions of water and ions, we show that the dominant contribution is due to the auto-correlation of the water polarization. The cross-term between water and ion polarization weakens the absorption. By a decomposition of the water signal into terms due to different solvation shells, we show that water in the first shell loses about half of its dielectric response and the signal is blueshifted. These effects in the first shell are the main cause for the observed reduction of the static dielectric constant and the faster dynamics seen in the overall spectrum. By a further division of the water contribution in self relaxation and collective relaxations, we show that only the dominant collective contributions are accelerated. In agreement with two-dimensional infrared vibrational echo spectroscopy experiments the self relaxation of single water molecules is slowed down by the presence of ions.

Via projection into folded and unfolded states we calculate the dielectric spectra for native and non-native structures from equilibrium simulations of an eight monomer alanine chain solvated in water for native and non-native states. In addition to the pure water resonance at about $20\,\text{GHz}$, a peak occurs in the range of several hundred megahertz. It is mainly caused by the high polarization of the alanine peptide and is significantly stronger when the peptide is folded. However, we can also find a slow process in the collective interactions between different water molecules in the first hydration shell in this low frequency range via a decomposition. This collective water relaxation in the hydration shell is about two orders of magnitude slower than in pure bulk water. Interestingly, the self-rotation of water dipoles is only slightly retarded even in the first hydration shell.

As a technological application of dielectric effects, we present a novel mechanism for pumping water on the nano scale. Our simulations show that water inside a carbon nanotube can be pumped using two electrodes which are positioned adjacent to the nanochannel. Prerequisite is that the electrode charges oscillate phase shifted to each other in the GHz-range. We derive an analytic polarization-dragging theory, which describes the observed parameter dependence well. The proposed setup is a potential prototype for the generation and control of flow in nanofluidic systems.

Kurzfassung

Die elektrostatische Wechselwirkung gehört zu den fundamentalen Kräften und ist äußerst wichtig für die Dynamik der hoch polaren Wassermoleküle und das Netzwerk aus Wasserstoffbrückenbindungen. Aus experimentellen dielektrischen Relaxationsspektroskopiemessungen ist gesichert, dass durch Zugabe von Stoffen zum Wasser, wie zum Beispiel Salzen, die Stärke der dielektrischen Absorption und die Position des Absorptionsmaximums im Frequenzraum verändert wird. Eine eindeutige Zuordnung einzelner spektraler Signale zu Wechselwirkungen zwischen verschiedenen Komponenten der Lösung ist jedoch ohne Unterstützung durch atomistische Simulationen unmöglich.

Das dielektrische Spektrum von wässerigen Natriumhalogenidlösungen ist in dieser Dissertation aus Moleklardynamiksimulationen berechnet und stimmt gut mit den experimentellen Messungen überein. Durch eine Aufspaltung des dielektrischen Signals in Kreuzkorrelationen zwischen verschieden Polarisationsbeiträgen von Wasser und Ionen zeigen wir, dass der dominante Beitrag von der Autokorrelation der Wasserpolarisation kommt. Der Kreuzterm zwischen Wasser- und Ionenpolarisation schwächt die Absorption. Durch eine Unterteilung des Wassersignals in die verschiedenen Solvationsschalen um Ionen zeigen wir, dass Wasser in der ersten Schale etwa die Hälfte der Amplitude seiner dielektrischen Antwort einbüßt und das Signal ins bläuliche verschoben ist. Diese Effekte in der ersten Wasserschale sind die Hauptursache für den im Gesamtspektrum beobachteten Rückgang der statischen dielektrischen Konstante und die schnellere Dynamik. Durch eine weitere Aufteilung des Wasserbeitrages in Selbstrelaxation und kollektive Relaxationen zeigen wir, dass nur die dominanten, kollektiven Beiträge beschleunigt werden. Jedoch ist im Einklang mit 2D-IR Vibratiosechospektroskopie die Selbstrelaxation der Wassermoleküle durch Ionen verlangsamt.

Durch Projektion in gefaltete und ungefaltete Zustände berechnen wir die dielektrischen Spektra für die verschiedenen Sekundärtrukturen einer Kette aus acht Alaninresiduen in wässeriger Lösung aus Gleichgewichtssimulationen. Zusätzlich zur reinen Wasserresonanz bei etwa 20 GHz tritt ein Peak im Bereich von einigen hundert Megahertz auf. Dieser ist zum großen Teil durch die hohe Polarisation des Alaninpeptides verursacht und deutlich stärker, wenn das Peptid gefaltet ist. Jedoch können wir in diesem niedrigen Frequenzbereich durch eine Aufspaltung auch einen langsamen Prozess in den kollektiven Wechselwirkungen zwischen Wassermolekülen innerhalb der ersten Hydrationsschale finden. Diese kollektiven Prozesse innerhalb der Hydrationsschale sind somit etwa zwei Größenordnungen langsamer als in reinem Wasser. Interesanterweise ist die Rotation von einzelnen Wasserdipolen selbst in der ersten Hydrationsschale nur wenig verlangsamt.

Eine Anwendung von dielektrischen Effekten präsentieren wir mit einem neuartigen Pumpmechanismus für Wasser auf der Nanoskala. Unsere Simulationen zeigen, dass Wasser in einer Kohlenstoffnanoröhre mittels zwei Elektroden, welche neben dem Nanokanal positioniert sind, bewegt werden kann. Voraussetzung dazu ist, dass die Elektrodenladungen zueinander phasenverschobenen im Gigahertzbereich oszillieren. Wir leiten eine analytische Theorie des Ziehens durch Polarisation her, welche die beobachtete Parameterabhängigkeit gut beschreibt. Das vorgestellte Setup ist ein potentieller Prototyp zur Erzeugung und Kontrolle von Flüssen in der Nanofluidik.

Erklärung

Hiermit erkläre ich, dass ich die vorliegende Dissertationsschrift mit dem Titel

Aqueous Dielectric Effects

selbständig angefertigt und hier für keine anderen als die angegebenen Hilfsmittel verwendet habe. Die Arbeit ist weder in einem früheren Promotionsverfahren angenommen noch als ungenügend beurteilt worden.

_____

Berlin, 13. Januar 2015

Danksagung

An dieser Stelle möchte ich mich bei all denjenigen bedanken, die mich während meiner Promotion unterstützt haben. Mein größter Dank gilt meinem Doktorvater, Herrn Prof. Dr. Roland Netz, von dem ich viel lernen durfte, der mir große Freiheit bei meiner Forschung ließ und mich auf die interessanten Themen dieser Dissertation ausmerksam machte.

Für die erfolgreiche Zusammenarbeit bei den Teilprojekten dieser Arbeit danke ich den Mitautoren meiner Veröffentlichungen Jun.-Prof. Dr. Stephan Gekle, Dr. Douwe Jan Bonthius und Julius C. F. Schulz außerordentlich. Herrn Prof. Dr. Richard Buchner aus Regenburg danke ich für die Bereitstellung zusätzlicher unveröffentlicher experimenteller Spektren als wichtige Vergleichsgrundlage für meine Simulationsstudien. Ich danke dem HPC Cluster der ZEDAT an der Freie Universität Berlin für die Bereitstellung von Rechenkapazität und Speicherplatz, ohne die meine Untersuchungen in der Tiefe nicht möglich gewesen wären.

Allen aktuellen und ehemaligen Mitgliedern der Arbeitsgruppe Netz danke ich für die tolle Atmosphäre in der wissenschaftlichen Arbeit und auch abseits der Fachthemen. Besonders hervorheben möchte ich an dieser Stelle meinen Bürokollegen Julius Schulz und danke für das angenehme Büroklima und die Hilfe bei der Lösung viele kleiner programmiertechnischer Herausforderungen in den letzten Jahren.

Meiner Ehefrau, meinem Sohn und meinen Eltern danke ich von Herzen für die Unterstützung und das Verständnis für meine wissenschaftliche Begeisterung.